Efficiency Improvement through Reduction in Friction and Wear in Powertrain Systems

Final Report

DOE Award Number: DE-FC26-04NT42263

Reporting Period: October 2004 – December 2009
Principal Investigator: Michael L. Killian
(248) 226-1766
MikeLKillian@eaton.com

Recipient: Eaton Corporation
Innovation Center
4201 N. 27th Street
Milwaukee, WI 53216

Subcontractors: Caterpillar, Inc.

Northwestern University

Argonne National Laboratory

DISCLAIMER

DOCUMENT AVAILABILITY, ACKNOWLEDGEMENT, DISCLAIMER and PROPRIETARY DATA NOTICE

Document Availability:
Reports are available free via the U.S. Department of Energy (DOE) Information Bridge:
http://www.osti.gov/bridge

Reports are available to DOE employees, DOE contractors, Energy Technology Data Exchange (ETDE) representatives, and Information Nuclear Information System (INIS) representatives from the following source:

Office of Scientific and Technical Information
P.O. Box 62
Oak Ridge, TN 37831
Tel: (865) 576-8401
Fax: (865) 576-5728
E-mail: reports@osti.gov
Web Site: http://www.osti.gov/contact.html

Acknowledgement:
This report is based upon work supported by the U.S. Department of Energy under Award No. DE-FC26-04NT42263.

Disclaimer:
Any findings, opinions, and conclusions or recommendations expressed in this report are those of the author(s) and do not necessarily reflect the views of the Department of Energy.

Table of Contents

List of Figures

	the sub-surface region. Polished surface require a very low load, potentially improving durability.
Figure 6.2.1-2	Typical types of rough surfaces
Figure 6.2.1-3	Comparison of 3D pressure distributions
Figure 6.2.1-4	Irregular pressure distribution results from rough surface contact.
Figure 6.2.1-5	Irregular contact loads cause subsurface residual stresses.
Figure 6.2.1-6	Prediction of crack propagation and coalescence for two semi-circular cracks.
Figure 6.2.2-1	Effect of fill level on the churning torque as well as the lubricant temperatures
Figure 6.2.2-2	Low fill level reduce operating temperatures.
Figure 6.2.3-1	Pin-on-ring Falex test shows effectiveness of coatings.
Figure 6.2.4-1	Results from the wear model show developing wear tracks as a function of time.
Figure 6.2.4-2	Lubricants and surface finishes for use on gears.
Figure 6.2.5-1	ANL-developed relationship between average friction and overall wear for steel on-steel sliding lubricant temperatures of room temperature and 100 degrees C.
Figure 6.2.5-2	ANL look-up table for friction coefficient after friction drop (if any) for 1 cm/sec sliding.
Figure 6.2.6-1	Graph of measured input torque at 100 percent loading and various speeds. Friction torque at low speed with Oil #1 was 47 percent lower than the baseline Oil #18.
Figure 6.2.6-2	Measured input torque at 50 percent loading and various speeds. Friction torque with Oil #1 is 45 percent lower than the baseline Oil #18.
Figure 6.2.6-3	Measured input torque at no load across various speeds. Under no load conditions churning losses correlate with calculated viscosity of the oils.
Figure 6.2.6-4	Caterpillar's new device for accurately measuring bearing endplay
Figure 6.2.7-1	Eaton spur gear, contact fatigue rollers and Falex ring that have been coated with Diamond-Like Carbon by physical vapor deposition.

Figure 6.2.7-2	Torque curves for various PVD Diamond-Like Carbon (DLC) coatings compared to bare, SAE 8620 carburized gear steel Falex tested in Eaton Roadranger SAE 50 Rev 7 lubricant. The DLC coatings effectively reduce torque and friction.
Figure 6.2.7-3	Wear scars on 3 SAE 52100 steel balls run against a bare SAE 8620 carburized gear steel ring (top row) are shown at 12x. Wear scars on balls run against a DLC2 coated ring (middle and bottom rows) exhibit 80 percent less wear.
Figure 6.3.1-1	Because of improper machining, the PVD coating on these rollers was stripped off in 48 hours
Figure 6.3.3-1	Integrated design methodology flowchart.
Figure 6.3.4-1	Falex four-ball test results for commercial and experimental oils.
Figure 6.3.4-2	Falex four ball test data. Note the reduced friction coefficient and reduced wear of RFY4 oil compared to the already low values of Eaton Roadranger Revision 7 lubricant.
Figure 6.3.4-3	Roadranger Revision 7 lubricant compared to hybrid Revision 7 oil containing the new RJK5 additive. The blended additive reduces torque by 30 percent.
Figure 6.3.4-4	Varied-oil, Falex four ball tests results comparing Revision 7 oil and the new hybrid Revision 7 oil with the RJK5 additive. For the upper, dark blue curve, the central 2-hours of the test ran with RJK5 additive blended into the Revision 7 oil before testing. For the lower, light blue curve, RJK5 additive was dosed into Revision 7 after slightly more than 2-hours test time.
Figure 6.3.5-1	Eaton dynamometer test run with a conventional transmission and a similar transmission with a reduced fill, dry sump. The dry sump significantly reduced parasitic torque.
Figure 6.3.5-2	Parasitic torque for four Caterpillar oils tested at 30 degrees C (86 degrees F), a temperature selected to simulate start-up or cold weather operation.
Figure 6.3.5-3	Parasitic loss for four Caterpillar oils tested at 60 degrees C (140 degrees F), cooler than the typical operating condition. Dry sump data clearly separates from the full sump (centerline fill) data.
Figure 6.3.5-4	Parasitic loss for four Caterpillar oils tested at 90 degrees C (194 degrees F), a typical operating condition. Dry sump data clearly separates from the full sump (centerline fill) data. Dry sump provides 47 percent reduction in parasitic loss.

Figure 6.3.5-5	Baseline Oil #18 was tested at four fill levels. As the fill level decreases from a centerline fill (full fill) to the dry sump level (low fill), the parasitic torque decreases by 49 percent.
Figure 6.4.1-1	Strategy for designing high efficiency and high fatigue resistant gear systems.
Figure 6.4.1-2	Illustration of the combined effects of surface topography (composite roughness decreasing from left to right) and lubricant selection (mineral oil, low-shear lubricant, and low-shear lubricant with additive) on friction reduction in mixed lubrication. The current and target conditions are identified.
Figure 6.4.1-3	Pitting Life Prediction Results in Comparison with Gear Test Data
Figure 6.4.1-4	Pitting Life Prediction Results Showing Good Correlation with Test Data
Figure 6.4.1-5	Subsurface stress and strain fields after one rolling cycle.
Figure 6.4.1-6	Traction of equivalent stress at point A and B for the first 4 cycles
Figure 6.4.1-7	Normalized contact fatigue lives for different models
Figure 6.4.2-1	Evolution of the disk wear track (left) and ball wear scar (right) over time. Ball image length scale is larger than that of the disk to facilitate visual analysis. Snapshots of the surfaces are shown without wear and at 1000, 2000, and 3000 cycles after the wear process begins
Figure 6.4.2-2	Evolution of the two ground surfaces moving at 3.75 m/s (left images) and 6.25 m/s (right image). Snapshots of the surfaces are shown without wear, and at 1000 and 2000 cycles after the onset of wear.
Figure 6.4.2-3	Film thickness (top) and pressure (bottom) distributions for the sinusoidal surface contact case simulated with (right) and without (left) wear.
Figure 6.4.2-4	Film thickness (top) and pressure (bottom) distributions for the ground surface contact case simulated with (right) and without (left) wear.
Figure 6.4.2-5	Illustration of the shape change of the contact zone due to an established wear track.
Figure 6.4.2-6	Centerline subsurface stress distribution with (right) and without (left) wear for the ground surface contact case. Dimensionless centerline pressure and film thickness shown above the stress distribution for clarity.
Figure 6.4.2-7	Film thickness (top) and pressure (bottom) distributions for the ball-on-disk

	contact case simulated with (right) and without (left) wear.
Figure 6.4.2-8	Centerline subsurface stress distribution with (right) and without (left) wear for the ball-on-disk case. Dimensionless centerline pressure and film thickness shown above the stress distribution for clarity.
Figure 6.4.2-9	Wear volume as a function of time for the three contact simulation cases analyzed. Inset shows a close-up of trends observed at the onset of wear.
Figure 6.4.2-10	Friction coefficients as a function of time after the introduction of wear (plots start at 500 cycles) for each simulated contact case.
Figure 6.4.2-11	Friction coefficient (solid line) and contact load ratio (hollow squares) as functions of time for the ball-on-disk case illustrating the relationship between friction and contact area during the wear process.
Figure 6.4.2-12	Mura's model for crack initiation within the grain
Figure 6.4.2-13	Applied shear stress pattern
Figure 6.4.2-14 & 6.4.2-15	Inclined slip plane emanating from the free surface with □= 450 and Benchmark of the normalized dislocation density for $\theta = 45^0$
Figure 6.4.2-16	Comparison of stored energy for various inclination angles
Figure 6.4.2-17	Comparison of stored energy for various inclination angles
Figure 6.4.2-18	The dislocation dipoles are aligned along the radial direction
Figure 6.4.2-19	Numerical results for □=1.4, □=0
Figure 6.4.2-20	Numerical results for circular hole
Figure 6.4.2-21	Model validations through comparison with the experimental results in [Etsion et al., 2005], (a) the static friction coefficient versus dimensionless normal load for copper on sapphire, and (b) maximum tangential force (static friction force) versus dimensionless normal load for copper on sapphire and copper on steel.
Figure 6.4.2-22	Comparison of static friction coefficient variations as a function of the dimensionless normal load for the contacts of the copper ball on the rough half-space of different materials.
Figure 6.4.2-23	Effects of surface RMS roughness, Rq, on static friction coefficient for the copper ball on the sapphire half-space.

Figure 6.4.3-1ab	Course pitch gear (left), processed in Batch 1063 with PVD CrWC coating, is compared to finer pitch gear processed in Batch 1137 with AlMgB14-TiB2-C coating.
Figure 6.4.3-2	Micrographs of PVD CrWC coated gear tooth: (a) Batch 1063, tooth tip, 3.05 microns, 1000x; (b) Batch 1063, tooth flank, -1.6 microns, 1000x; (c) Batch 1063 root, 1.62 microns, disband, 1500x.
Figure 6.4.3-3	Micrographs of PVD Aluminum Magnesium Boride-Titanium DiBoride-Carbon (AlMgB14-TiB2-C) coated gear tooth: (a) Batch 1137, *tooth tip*, 3.72 microns, 1000x; (b) Batch 1137, *gear flank near tooth tip*, 2.72 microns, 1000x; (c) Batch 1137, *gear flank at half-tooth height*, 1.78 microns; (d) Batch 1137, at root of gear tooth, 1.46 microns, 1500x. Coating has delaminated from steel substrate of fine pitch.
Figure 6.4.3-4	Micrographs of PVD Chromium/ Tungsten Carbide-Carbon (Cr/WC-C) coated gear tooth: (a) Batch 1062, *tooth tip*, 2.92 microns, 1500x; (b) Batch 1062, at *root* of gear tooth, 2.62 microns, 1500x. Coating has good adhesion at root of coarse pitch gear.
Figure 6.4.4-1	Roller contact fatigue test of bare steel in Roadranger Revision 7 oil. Steel wore and polished during testing, reducing the torque.
Figure 6.4.4-2	Roller contact fatigue test of super finished bare steel in low friction TDN3 oil. Wear was minimal with the torque remaining at 111 inch-pounds over the 96 hour test.
Figure 6.4.4-3	Roller contact fatigue test of super finished, PVD coated AlMgB-TiB-sl steel in Roadranger Revision 7 oil. Wear was minimal with the torque reducing from 140 to 120 inch-pounds over the 96 hour test
Figure 6.4.4-4	Roller contact fatigue test of super finished, PVD coated AlMgB-TiB-C steel in Roadranger Revision 7 oil. Wear was minimal with the torque remaining at 82 inch-pounds over the 96 hour test.
Figure 6.4.4-5	Roller contact fatigue test of super finished PVD DLC coated steel in low friction TDN3 oil. Wear was minimal with the torque remaining at 82 inch-pounds over the 96 hour test.
Figure 6.4.4-6	Summary of roller contact fatigue test of comparing bare steel, super finished steel and PVD coated steels. Best result was a 51 percent decrease in torque, and minimal wear, due to PVD DLC coating and TDN3 low friction oil.
Figure 6.4.5-1	Results from a 180 horsepower dynamometer tests shows the dry sump alone improved efficiency by 0.5 percent compared to the standard transmission. This 2008 improvement relates to decreased churning losses.
Figure 6.4.5-2	This graph compares efficiency for a standard baseline transmission and the dry sump transmission. The 240 horsepower dynamometer tests run in June 2008 showed a 0.32 percent improvement in efficiency with the 2008 dry sump transmission.
Figure: 6.4.6-1	A 2009 efficiency improvement of 0.65 percent resulted with the Best Tech 1 transmission compared to the standard transmission for 180 horsepower

	dynamometer tests.
Figure 6.4.6-2	At 240 horsepower the 2009 Best Tech 1 transmission gave efficiencies greater than 99 percent for all three gear ratios tested. For the under drive gear ratio the efficiency improvement of the Best Tech 1 transmission over the standard transmission was 1.04 percent.
Figure 6.4.6-3	A standard Eaton transmission is mounted on the transmission efficiency dynamometer test stand at Southwest Research Institute.
Figure 6.4.6-4	Effects of various oils on the efficiency of a standard transmission are shown. Experimental low friction oil TDN3 actually lowered efficiency while the new low viscosity oil TGM5 raised efficiency slightly.
Figure 6.4.6-5	Effects of various oils on the efficiency of a standard transmission are shown. Experimental low friction oil TDN3 actually lowered efficiency while the new low viscosity oil TGM5 raised efficiency slightly.
Figure 6.4.6-6	Effects of the dry sump with PVD DLC coated gears and low friction TDN3 oil on efficiency are compared to the efficiency of a standard transmission with SAE 50 Revision 7 oil. The advanced transmission with dry sump showed an efficiency gain of 0.65 percent in overdrive and 0.62 percent for underdrive.
Figure 6.4.6-7	Effects of the dry sump with PVD DLC coated gears and low friction TDN3 oil on efficiency are compared to the efficiency of a standard transmission with SAE 50 Revision 7 oil. At 1500 rpm and 1187 N-m input torque the advanced transmission with dry sump showed an efficiency gain of 0.70 percent in overdrive and 0.67 percent for underdrive.
Figure 6.4.6-8	The Final Drive Four-Square testing Rig.
Figure 6.4.6-9	Final Drive Four-Square Efficiency Testing Data.
Figure 6.4.6-10	Final drive energy gain rolled up to the flywheel.

List of Tables

1.0 EXECUTIVE SUMMARY

The objective of this project is to improve the efficiency of truck drivelines through reduction of friction and parasitic losses in transmission and drive axles. Known efficiencies for these products exceeded 97 percent, so the task was not trivial. The project relied on a working relationship between modeling and hardware testing. Modeling was to shorten the development cycle by guiding the selection of materials, processes and strategies. Bench top and fixture tests were to validate the models. Modeling was performed at a world class, high academic level, but in the end, modeling did not impact the hardware development as much as intended. Insights leading to the most significant accomplishments came from bench top and fixture tests and full scale dynamometer tests.

A key development in the project was the formulation of the implementation strategy. Five technical elements with potential to minimize friction and parasitic losses were identified. These elements included churning, lubrication, surface roughness, coatings and textures. An interesting fact is that both Caterpillar and Eaton independently converged on the same set of technical elements in formulating their implementation strategies.

Exploiting technical elements of the implementation strategy had a positive impact on transmission and drive axle efficiencies. During one dynamometer test of an Eaton Best Tech 1 transmission, all three gear ranges tested: Under drive, direct drive and over drive, showed efficiencies greater than 99 percent. Technology boosts to efficiency for transmissions reached 1 percent, while efficiency improvements to drive axle pushed 2 percent. These advancements seem small, but the accomplishment is large considering that these products normally run at greater than 97 percent efficiency.

Barriers and risks to implementing these technology elements are clear. Schemes using a low fill sump and spray tubes endanger the gears and bearings by lubricant starvation. Gear coatings have exhibited durability issues, stripping away under conditions less demanding than 750,000 miles in service on the road. Failed coatings compound the problem by contaminating the lubricant with hard particles. Under the most severe conditions, super finished surfaces may polish further, reaching a surface roughness unable to support the critical oil film thickness. Low viscosity and low friction lubricants may not protect the gears and bearings adequately leading to excessive pitting, wear and noise. Additives in low friction oils may not stay in solution or suspended thus settling to the bottom and unavailable when they are needed most.

Technical barriers and risks can be overcome through engineering, but two barriers remain formidable: (1) cost of the technology and (2) convincing fleet owners that the technology provides a tangible benefit. Dry sumps lower lubricant operating temperatures so the removal of heat exchangers and hoses and reduced demand on engine cooling systems justify their use. The benefits of surface texturing are varied and remain unproven. Lubricant costs seem manageable, but the cost of super finishing and gear coating are high. These are issues of scale and processing technology. Going across the board with gear super finishing and coating will reduce costs. Pushing the envelope to applications with higher torque and higher power density should drive the adoption of these technologies.

Fleet owners are an educated and seasoned lot. Only technology measureable in dollars returned is used on truck fleets. To convince fleet owners of the benefit of these technologies, new precision in measuring fuel efficiency must be introduced. Legislation for a minimum standard in truck miles per gallon would also enable the use of these technologies.

Improving the efficiency of truck transmissions and axle will make a noticeable impact on the fuel consumption by heavy vehicles in the United States. However, the greatest benefit will come when all the individual efficiency technologies like hybrid power, aerodynamic fairings, auxiliary power units, super single aluminum wheels, single wide tires and reduced cross section radiators are combined synergistically in a single vehicle, the high efficiency truck.

2.0 INTRODUCTON

Reducing friction and parasitic energy loss by 30 to 50 percent in the transmissions and axles used in Class 3 to 8 trucks, without compromising performance or durability, was the objective of this project. Increased efficiency will improve fuel economy by 2 to 4 percent, producing a savings of 390 to 780 gallons per vehicle annually.

This program had a duration of five years. In Years 1 to 3 the approach was (1) to develop computer simulation tools for various contact geometries to predict friction, wear and oil churning losses, (2) to validate friction reduction strategies with coupon bench top and fixture testing and (3) to identify commercialization strategies for improving efficiency in truck transmissions and axles. In Years 4 and 5 the approach was to conduct dynamometer efficiency tests on components and on full scale drive axles and transmissions

Formulation of the implementation strategy to reduce friction and parasitic losses was a key deliverable in the program. The strategy identified specific technical factors that can be exploited to reduce the US consumption of petroleum by trucks. Among the technical factors were the following:

1. Churning
2. Lubrication
3. Surface Roughness
4. Coatings
5. Textures

These technical factors were pursued using a variety of tools and methods including

- Screening with bench top and fixture tests
- Dynamometer tests
- Low fill sump and spray tubes
- Low friction oil with solid lubricants
- Super finishing of gears
- Diamond Like Carbon (DLC) and Aluminum-Magnesium-Boride (AlMgB) coatings applied on gears by PVD/CVD

Reducing churning proved to be the most effective technical element for minimizing parasitic loss. Churning is the viscous drag from contact between rotating components and the lubricant. This was accomplished mainly by the use of low fill level sumps often referred to a "dry sumps". To prevent damage to gears and bearings from insufficient lubrication, spray tubes were used direct oil to the key components. In one particularly effective trial, Eaton 5R transmission solenoid valves were used to modulate the oil sprays, sending lubricant only to the contact interfaces actually transmitting torque.

Lubricant selection was the most important factor in minimizing friction. While many commercial transmission and axle lubricants are very good at minimizing wear and enhancing durability, they are not functionally directed at improving efficiency. Commercial truck lubricants from large oil companies also seem hampered by reliance on chemical strategies specifically tailored for automotive applications. Powerful friction-limiting additives like ZDDP have been eliminated due to their effect on engine emission catalysts. Primary methods for reducing friction with lubricants included the addition of solid lubricants, the addition of known friction modifiers and addition of compounds that form solid lubricants at the contact interface under the right combination of temperature and pressure.

Low surface roughness also is powerful in minimizing friction and wear. Super finishing with the REM process proved to be very effective in producing mirror-like surfaces. Super finishing of gear teeth surfaces was a prerequisite for depositing physical vapor deposition coatings on gears.

Physical Vapor Deposition (PVD) coatings are not exploited for reducing friction at gear contact interfaces because there are many challenges with this technology. Among the challenges are the gear geometry, limited processing temperature, surface finish and cost. These challenges influence the thickness, bond strength and durability of the PVD coatings. A technical advancement in coatings was the incorporation of solid lubricants within the coating. Opportunities exist to tailor the lubricant to interact beneficially with the coating. At present most lubricants are active with a bare steel surface. This area is worthy of further development.

Surface texturing, creating shallow, straight or curving grooves, bowl-shaped dimple patterns, waves or other patterns, is considered to be means for reducing friction and for entrapping oil for use during conditions of lubricant starvation. Designing a texture for a specific application and proving that the texture is effective in reducing friction is extremely difficult. Textures are another technology area for further development, especially in terms of texturing super finished surfaces or coating.

3.0 BACKGROUND

From inception this project based its friction reduction methodology on the well established Stribeck curve, **Figure 3.0-1**. The Stribeck curve presents the relationship between friction coefficient and the lubricant film thickness. This curve also can be used to compare friction to other tribological parameter like pressure, velocity, viscosity and temperature that are factors in determining the oil film thickness. The Stribeck curve separates tribological behavior into three regimes: Boundary lubrication, mixed lubrication and full film lubrication (elastohydrodynamic

or hydrodynamic). Boundary lubrication occurs under conditions of high loads and low speeds. Oil film is thin, comparable to the height of asperities on a rough surface. The asperities on the rough surfaces often contact directly causing high friction. Continually running under boundary lubrication conditions results in high wear and can cause premature component failure.

Reduced pressure and increased velocity shift the operating point to the right. The oil film thickens. Less asperity contact occurs and friction lowers. These conditions characterized mixed lubrication. Many highly loaded products like truck transmissions and drive axles operate in the mixed lubrication regime. Good engineering practices regarding the selection of materials, heat treatments, surface roughness and lubricants enable prolonged operation under mixed lubrication. For example, truck transmissions have 750,000 mile warrantees, and many operate satisfactorily beyond the 1M mile mark.

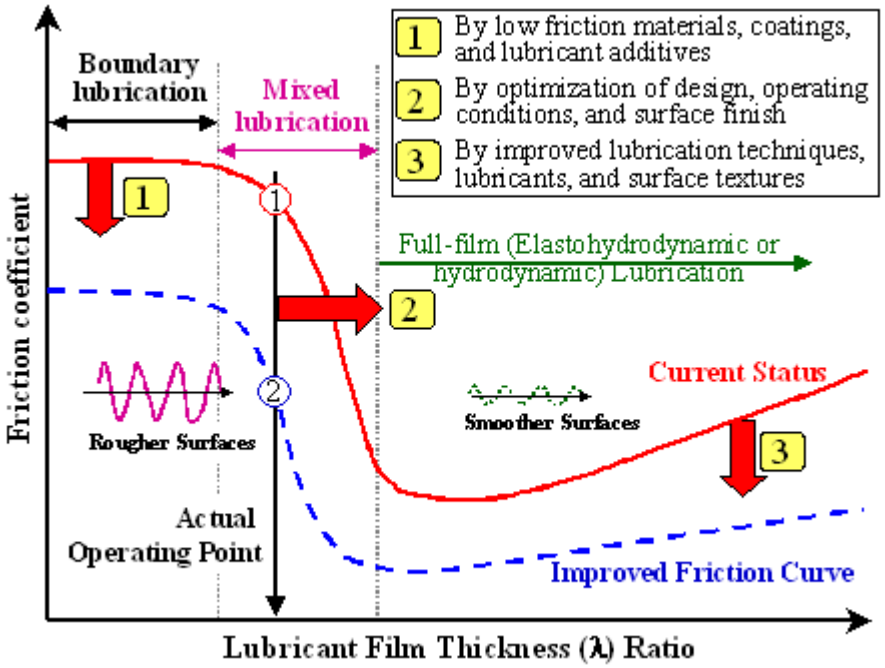

Figure 3.0-1: Stribeck curve shows the relationship between friction and the oil film thickness and provides a guide for the friction reduction strategy.

Reduced loads and increased speeds push the operating point farther right into the regime of full film lubrication. The oil film thickness exceeds the height of the asperities of the surface roughness. There is no asperity contact. Friction is very low. Additional speed increases and load reductions actually increase friction due to increasing fluid drag from the thick oil film.

This project addressed friction in all three lubrication regimes of the Stribeck curve. Friction during boundary lubrication and mixed lubrication was reduced through the use of low friction coatings, low surface roughness, additives to the lubricants and special lubrication techniques. Provisions for control of friction in full film lubrication involved the use of solid lubricants and surface textures, although full film lubrication was not significant in this project.

4.0 OBJECTIVE

To conduct research and development to reduce friction and parasitic energy loss by 30 to 50 percent, in truck transmissions and axles used in Class 3 to 8 trucks, is the objective of this project. The result of that work will be an implementation strategy to minimize friction and oil churning losses, without a compromise in performance and durability.

5.0 DELIVERABLES BY BUDGET PERIOD

Budget Period 1

Project Deliverables-Year 1

1. Boundary film characterization and relationships with materials, oil additives, and coatings
2. Potential benefits study due to friction reduction in gears

Project Deliverables-Year 2

3. Roughness and texture effects on friction
4. Selection of best lubricants for driveline components friction reduction
5. Modeling of boundary lubrication and potential methods to reduce boundary friction
6. Mixed lubrication models for uncoated, textured, and coated surfaces

Budget Period 2

Project Deliverables-Year 3

7. Component surface design model and benefits evaluation
8. A- Optimized sump and reduced churning loss for axles & transmissions
9. Feasibility study for low friction materials and coatings for driveline components
10. Advanced wear model with surface evolution
11. The effect of lubricant rheology, boundary film properties, sump starvation, and severe conditions on friction
12. Models for improved gear design, bearing and seal design/selection
13. Friction, wear and pitting bench test results
14. Preliminary technology implementation strategy for axles and transmissions.
15. Improved design guidelines for lubricant selection

Budget Period 3

Project Deliverables-Year 4

16. Commercialization potential of low friction materials and coatings
17. Failure criteria for driveline component design
18. Integrated design procedure to reduce friction in gears, seals and bearings
19. Friction, wear, and pitting bench test results

(8) B- Optimized sump and reduced churning loss for axles

Budget Period 4

Project Deliverables-Year 5

20. Integrated design model for low friction gears, bearings and seals
21. Integrated efficiency and durability predictive tools
22. Process techniques to overcome difficulties with gear geometry effects and temperature effects.
23. Test data to support use of coated gears in transmission dynamometer tests.
24. Dynamometer and durability test results for low friction driveline components
25. Dynamometer test results using a low friction axle and transmission prototypes

6.0 ACCOMPLISHMENTS

6.1 Budget Period 1

Deliverables

1. Boundary film characterization and relationships with materials, oil additives, and coatings
2. Potential benefits study due to friction reduction in gears
3. Roughness and texture effects on friction
4. Selection of best lubricants for driveline components friction reduction
5. Modeling of boundary lubrication and potential methods to reduce boundary friction
6. Mixed lubrication models for uncoated, textured, and coated surfaces

6.1.1 Boundary Film prediction and Behavior (Argonne)

Argonne developed a test method and approach to generate a boundary friction look-up table for different oils at elevated temperatures. This measurement used the ball-on-disc tester shown in **Figure 6.1.1-1**. Radiative heating is used to heat the lubricant cup containing the test specimens and lubricant. Temperature was measured by a thermocouple immersed in the oil, and controlled by a feedback system. The friction coefficient was continuously monitored during each test. The contact condition was always under the boundary lubrication regime.

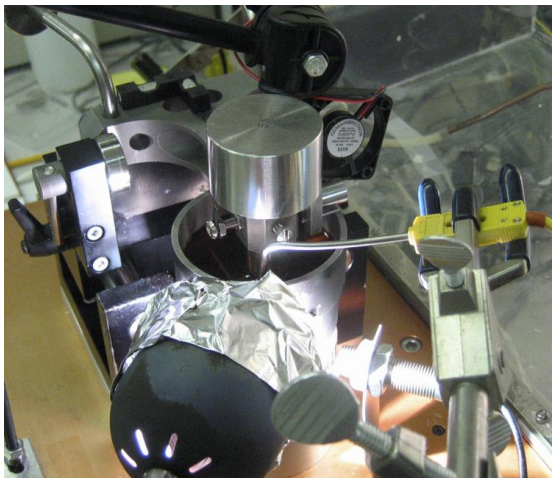

Figure 6.1.1-1: **Argonne used a ball-on-disc friction test rig for elevated temperature tests.**

Friction measurement tests were conducted for the Optimol gear oil at 50° C, 70° C, 100° C and 125° C using the same procedure. **Figure 6.1.1-2** shows the frictional behavior during 100°C test. There was a decrease in the boundary friction from the initial average value of 0.13 to an average value of about 0.05 after the 5 hour run-in.

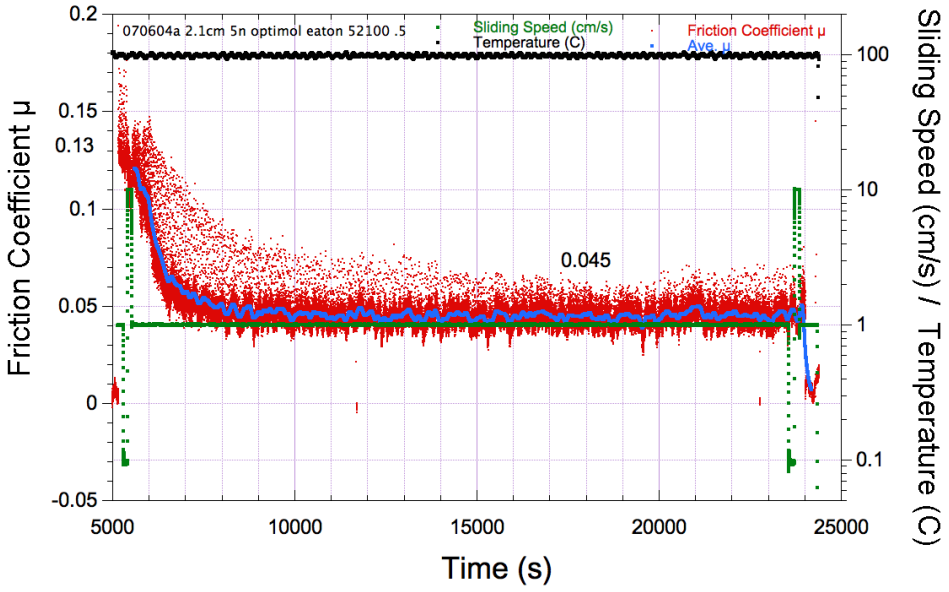

Figure 6.1.1-2: Variation of friction during boundary friction measurement with Optimol gear oil at 100°C.

Similar frictional behavior trend was observed in the test at other temperatures. The rate of friction decrease was higher as the test temperature increases. Analysis by simple curve fitting indicated that the variation of boundary friction with test temperatures for this oil showed an exponential decay with time. The friction results were used to prepare a series of look-up tables. Tests were conducted for the following oils supplied by Caterpillar and Eaton: Roadranger SAE 50 Revision 7, CAT#20, CAT FDAO SYN and CAT FDAO 50.

6.1.2 Potential Benefits Study due to Friction reduction in Gears

Surface Topography Optimization for Friction Reduction in Gears

A computer model for surface evolution due to sliding wear in mixed lubrication was developed. Results showed that the model can simulate surface finish/texture change caused by wear under severe operating conditions. It also predicted the friction and lubrication characteristics with changing surface topography. **Figures 6.1.2-1, 6.1.2-2, and 6.1.2-3** show results of two preliminary trial cases with simulated surface evolution in mixed EHL contacts. **Figures 6.1.2-1 and 6.1.2-2** show the result of a smooth surface (top) sliding over a stationary textured surface (bottom) with the contact is circular. Condition of the surface is shown after selected steps of 10, 150, 350, and 1000 are shown. **Figure 6.1.2-2** is similar to **Figure 6.1.2-1**, but it shows two moving ground surfaces, at different speeds, also with circular contact. The development of the wear track on both surfaces is shown as a function of similar steps. **Figure 6.1.2-3** shows three balls on ring sliding configuration, with the balls not rolling. This is a simple configuration, which can be used to correlate modeling and experimental test results such as wear scar development and friction as a function of load (contact stress0, surface topography, lubricant, and sliding speed.

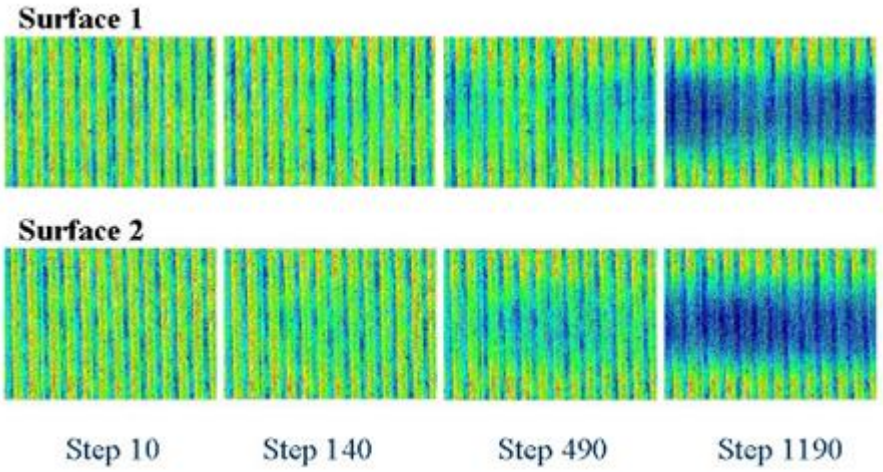

Figure 6.1.2-1: Evolution of surfaces due to sliding wear: a moving smooth Surface 1 (top) against a sinusoidal stationary Surface 2 (bottom), circular EHL contact.

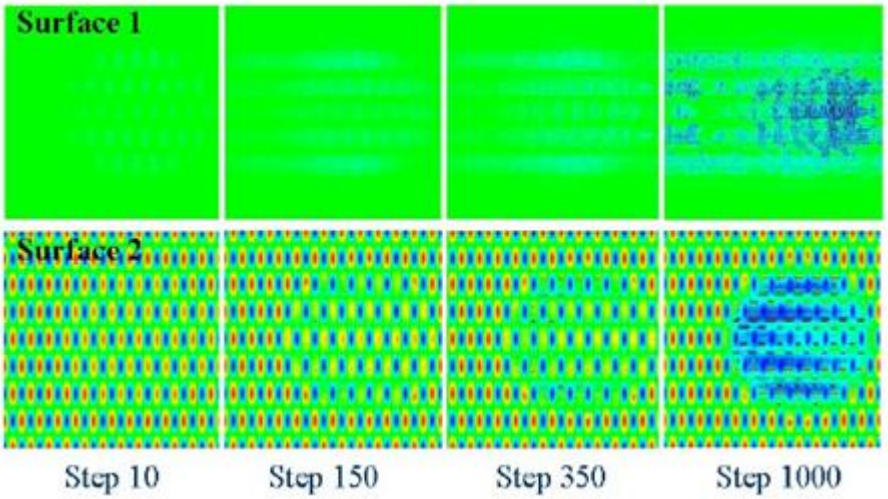

Figure 6.1.2-2: Evolution of surfaces due to sliding wear: a moving ground Surface 1 (top) against a faster moving ground Surface 2 (bottom), circular EHL contact.

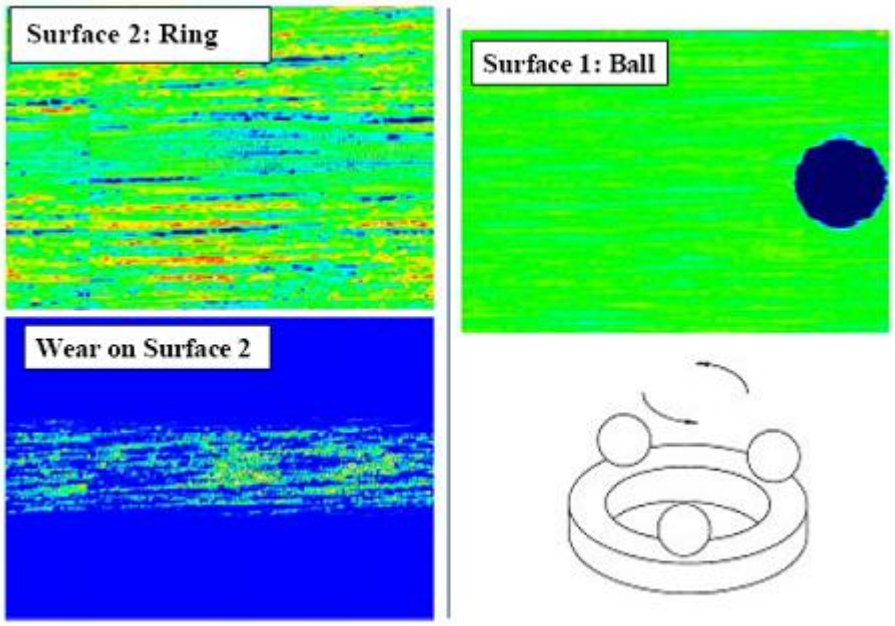

Figure 6.1.2-3: Evolution of surfaces due to sliding wear: simulation of wear in Three-Ball-On-Ring test. Balls are sliding over the ring, but do not roll. Surface 1 is represented by the ball contact (circular) and Surface 2 is the contact track on the ring.

Friction Reduction in Gears

Using the mixed lubrication model refined under this project, a systematic study on the mixed lubrication friction has been conducted and some preliminary results obtained. These results show that, when the film thickness ratio, λ, is large and there is little contact, then the limiting shear stress dominates the total friction and boundary additives do not have significant influence on friction. However, if the surface is rough and there is significant asperity contact, the

boundary additives may have a great influence on the total friction and the rheology of lubricant may not play an important role. There are three major technologies that can help reduce mixed lubrication friction. They are:

1) Optimized surface finish/textures
2) Good lubricant rheological properties (e.g. low limiting shear stress)
3) Boundary additives

Figure 6.1.2-4 summarizes the results that shows that, if all three are used, the total friction can be reduced from a baseline of 0.079 or so (shaved or ground surfaces, base mineral oil with no additive) down to about 0.021(#2 polished surfaces, low shear synthetic oil with low friction boundary additives).

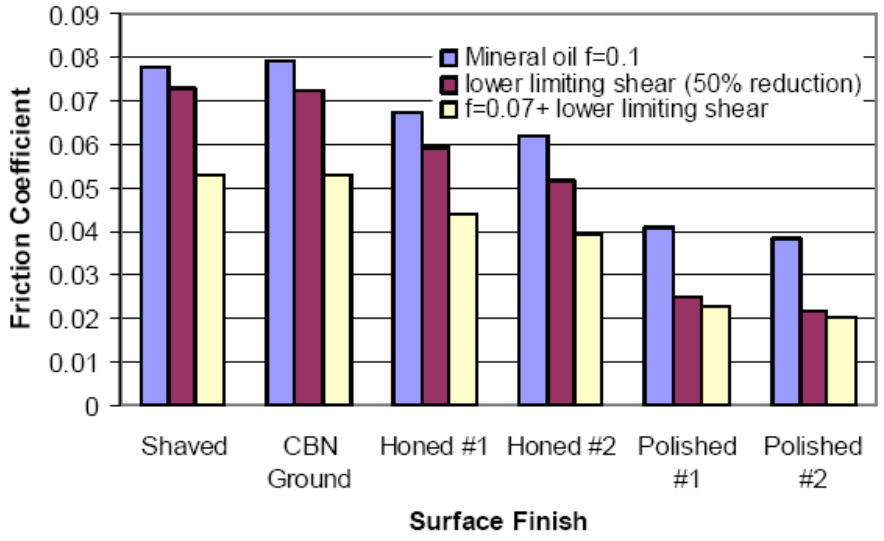

Figure 6.1.2-4: **Mixed lubrication friction influenced by surface roughness/textures, lubricant rheology and boundary additives.**

Figure 6.1.2-4 shows the baseline friction coefficient for gears environment is about 0.079 for ground or shaved surfaces lubricated by base mineral oil with no additive. Lowest friction of about 0.021 under the same operating conditions based on #2 polished surfaces lubricated with low shear synthetic oil with low friction additives.

Excellent opportunities exist for friction reduction in gears. Final selection of a specific approach (combination of the three technologies above) would be influenced by ability to generate a specific texture, lubricant characteristics and boundary additives for specific materials/coatings used.

Gear Tooth Roughness

Two approaches of generating smoother surface roughness on transmission gear teeth were evaluated:

- Isotropic finishing process for enhancing surface smoothness of transmission gears was investigated and REM was identified as having the most promising process technique. It has been found that this process is relatively faster, and the surface roughness is around 7 micro-inches. This process is very promising for friction reduction in gears.

- Modern honing processes for transmission gears also were investigated. It has been claimed that the new honing method could reduce surface roughness from hobbed gears (60-120 micro-in) down to 3-5 micro-in with one process step in minutes. The production cost can be lower than isotropic polishing. For those specific samples the surface finish is about 12 micro-in.

Table 6.1.2-1 below and the associated **Figure 6.1.2-5** show the surface roughness and appearance of honed and isotropic finished samples.

Table 6.1.2-1: **Data for honed and REM super finished surfaces.**

Honed vs Isotropic Gear Tooth Surface Roughness

	Ra (nm)	Rq (Nm)	Rt (nm)
Honed Gear Surface (Ra = 11.3 µin)	287.26	365.77	2970.45
Honed Gear Surface (Ra = 14.0 µin)	356.26	463.02	4943.45
REM Polished Gear Surface (Ra = 14.0 µin)	178.41	225.82	3166.26
REM Polished Gear Surface (Ra = 14.0 µin)	187.54	234.88	2711.56

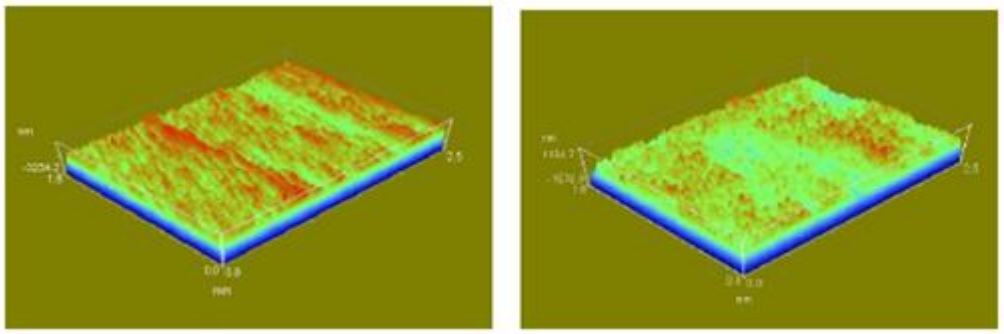

Figure 6.1.2-5: Honed (left) and REM isotropic polished gear tooth surface (right).

6.1.3 Roughness and Surface Texture

Surface Texture

Surface topography and texture design is an important part of surface engineering. Creating surfaces with controlled micro geometry may be an effective approach leading to improved performance of tribological interfaces. Surface finishing processes, such as turning, shaving, grounding, honing, polishing, and dimpling, generate surfaces with textures of specific topography. Specially controlled textures may be found on the surfaces of many mechanical components. One may anticipate that the design of surface textures should be related to the type of contact, materials of the interface, and most importantly, operating conditions. Evaluation of a surface texture design requires extensive analyses of its performance in an expected working environment. Experimental evaluations of surface textures require sample manufacturing and intensive testing, which can be expensive and time consuming even for the simplest surface patterns. Most importantly, a complete evaluation is sometimes nearly impossible because of the limitation of sample fabrication and experimental condition control. Considering the fact that engineered surface topography may be reasonably simulated, a model-based numerical system with contact and mixed lubrication analysis capability has been developed for such evaluations.

Surface roughness has a significant influence on friction. If it is too coarse, the surface roughness changes with test time (use time) and friction is reduced. This phenomenon has been evaluated at Eaton using a *rolling contact fatigue* (RCF) test rig modified for measuring friction, **Figure 6.1.3-1.**

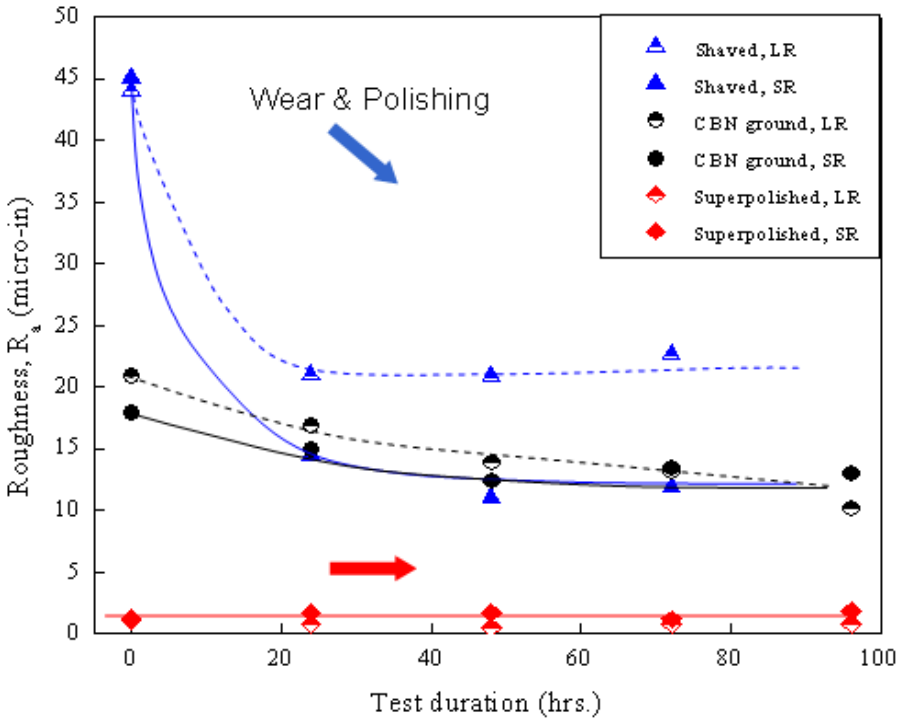

Figure 6.1.3-1: Initial rough surface wear and polish during roller contact fatigue testing. This generates debris and increases noise. Smooth surfaces remain largely unchanged.

Design of Surface Textures

In mixed lubrication, enhancement of film helps reduce friction. An optimal dimple texture design for effective lubrication in such contacts should avoid overlapping individual dimple influence areas. The optimal texture density is among 3 to 11 percent for counterformal contacts. Non-isotropic shapes are preferred with the shorter size along the motion direction. Textures should have shallow depth no larger than 5 micrometers. A triangular pattern with narrow grooves in the motion direction seems to be the best choice. A sinusoidal wave propagates along the motion direction may also be a good selection. All results indicate that the texture direction, either face-to-face or face-to-edge, only has negligibly small influence on the lubrication of textured surfaces under the conditions tested in this study. The texture orientation angle strongly affects the film thickness produced by textured surfaces. Smaller orientation angles are preferred for thicker films. Texture aspect ratio in terms of width/length is inversely related to film thickness. Smaller aspect ratios are preferred for thicker films.

Elliptic dimples may be defined as AxBxSxd with its principal radii, A and B, center span, S, and depth, d. Dimples of the same elliptical shape were numerically generated, with the ratio of elliptic radii of A/B =1/4, to evaluate the importance of these basic factors. The pressure peaks can be correlated to the dimple-free area with or without contact, depending on the severity of interaction influenced by the dimple design. Because of the relative motion of the surfaces, film thickness is a function of time even though the operating conditions are not time dependent. The change of the composite roughness, measured as the root-mean square of the surfaces deviated from its deformed centerline, follows the pattern of the film thickness variation. Contact may occur along the banks of dimples. However, the total contact area does not vary with time because the number of dimples passing through the contact region in a unit time is quite constant if the dimples are not too large. Each dimple has a certain influence area, related to operating conditions and the dimple geometry.

Effect of Size

The relationship between the dimple size and the central film thickness is numerically investigated at a constant dimple density (11.22 percent) and a fixed dimple depth (3 micrometers). The result indicates that the correlation is not linear for both condition groups. At very small sizes, film thickness reduces with the increase of dimple size. The trend turns when the dimple size is further increased. Together with the film pattern, one can easily see the lubrication transition from a highly hydrodynamic state of the case with several large size dimples to a mixed state for the case with many small size dimples.

Effect of Depth

The effect of dimple depth is numerically investigated at a constant dimple density (11.22 percent) and a fixed dimple size (60x240x240). Results reveal a minimum film thickness in all speed-size combinations. In this part of the study, the number of interruption is kept the same while the intensity of single-dimple interruption is significantly varied through the depth change. Increase in dimple depth may enlarge the dimple-influence area. The rise of film thickness values at a larger depth is likely due to the mathematic average of gaps, to which the depth contribution is larger if the dimple is deeper. Similar central film thickness values may correspond to completely different film patterns.

Effect of Density

The effect of dimple density is numerically investigated for surfaces of the same dimple shape under different size-speed combinations and with a fixed dimple depth (3 micrometer, or 1000(d/a) = 5.04). Changing the density while keeping the size the same varies the number of interruptions. The density effect is also related to the dimple size with respect to the Hertzian area. However, for the high-speed low load case with dimples of AxB = 60x240 μm^2, there seems to be a range of optimal density of about 3 to 12 percent, where 5 percent dimple density looks to be the best choice, as indicated by the circle in **Figure 6.1.3-2**. Note that the high film thickness at higher density is due to the average in the entire central area including both textured and non-texture regions.

The numerical results were qualitatively compared with experimental results from ANL by Kovalchenko et al. [2004] for a group of experimental studies on the friction behavior of disk surfaces with circular dimples made with a few different depths, density and diameters. This comparison suggests that shallower dimples are preferred, texture density should not be large, 3 to 11 percent should be the range, and the size along the motion direction should not be long.

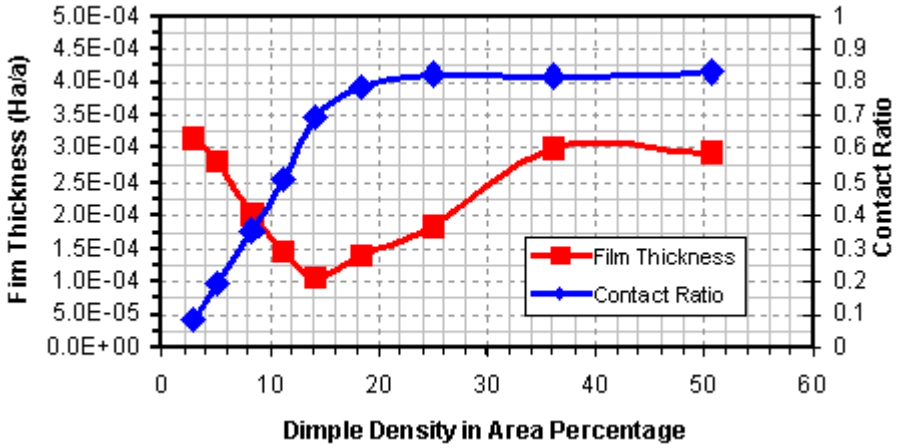

Figure 6.1.3-2: **A dimple density of 3 to 12 percent is a good choice to maintain a reasonable oil film thickness.**

The dimple influence area, which indicates the intensity of interruption and is a function of dimple geometry and operating conditions, and the number of interruption, which is related to dimple density, are two key factors for designing dimpled surfaces for counterformal contact lubrication. The results suggest that an optimal dimple texture design for effective lubrication in such contacts should avoid overlapping individual dimple influence areas.

In mixed lubrication, enhancement of film helps reduce friction. Grove and dimple textures of different distribution patterns have been analyzed. **Figure 6.1.3-3** shows a triangular and sinusoidal distribution. A triangular pattern with narrow grooves in the motion direction seems to be the best choice. A sinusoidal wave propagates along the motion direction may also be a good selection. All results indicate that the texture direction, either face-to-face or face-to-edge, only has negligibly small influence on the lubrication of textured surfaces under the conditions tested in this study. The texture orientation angle strongly affects the film thickness produced by

textured surfaces. Smaller orientation angles are preferred for thicker films. Texture aspect ratio in terms of width/length is inversely related to film thickness. Smaller aspect ratios are preferred for thicker films. **Figure 6.1.3-4** shows vibra-groove samples that were tested in this project.

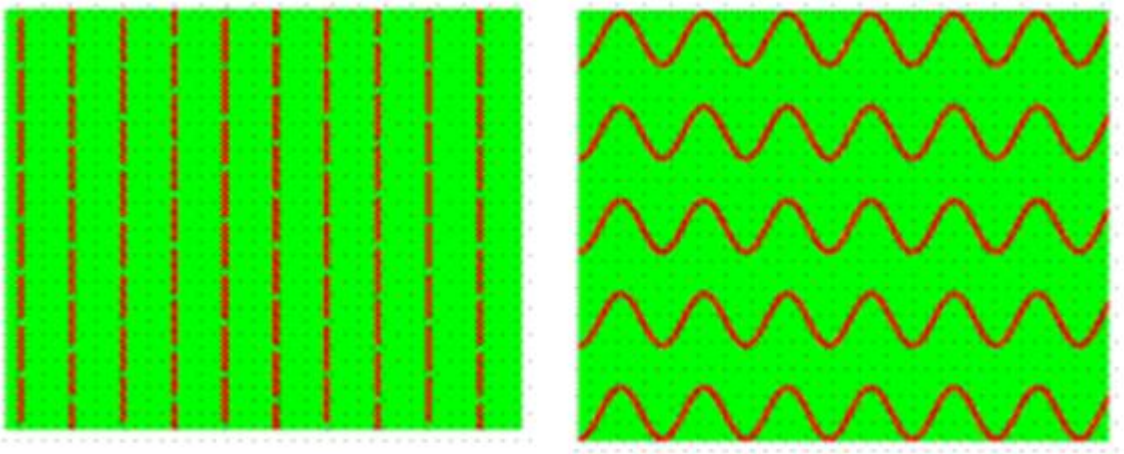

Figure 6.1.3-3: A triangular (left) and sinusoidal (right) texture distribution.

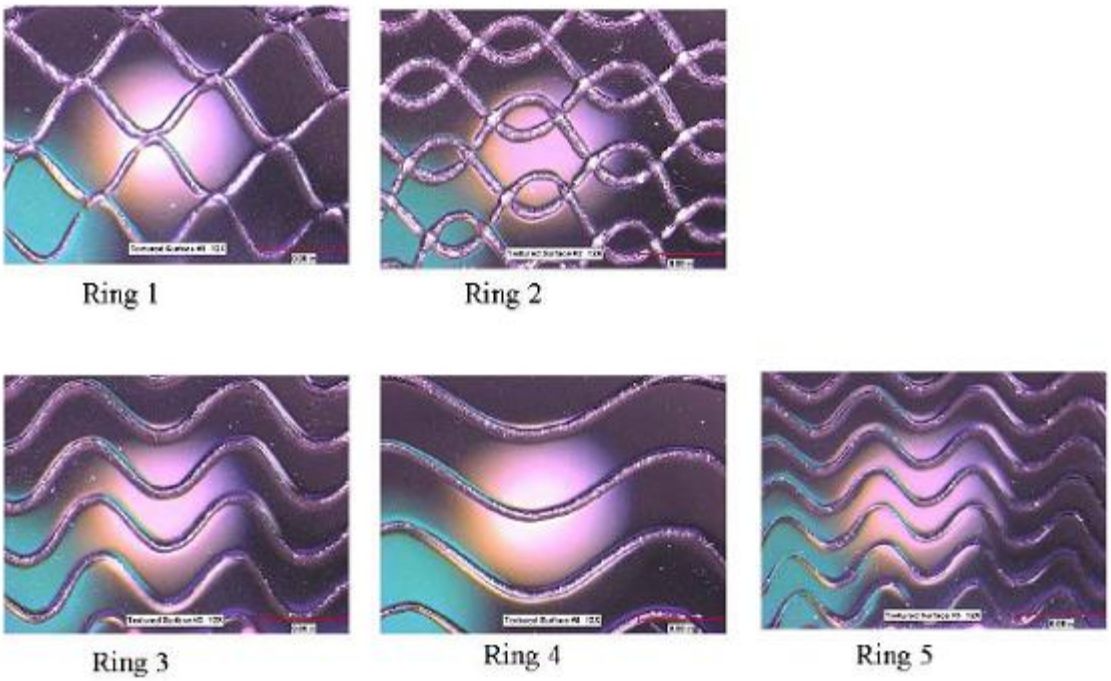

Figure 6.1.3-4: Surface texture, vibra-grooved samples. Rings 2 and 4 exhibited lowest coefficient of friction in Falex mailbox pin test. Contact stress: ~13,000 psi.

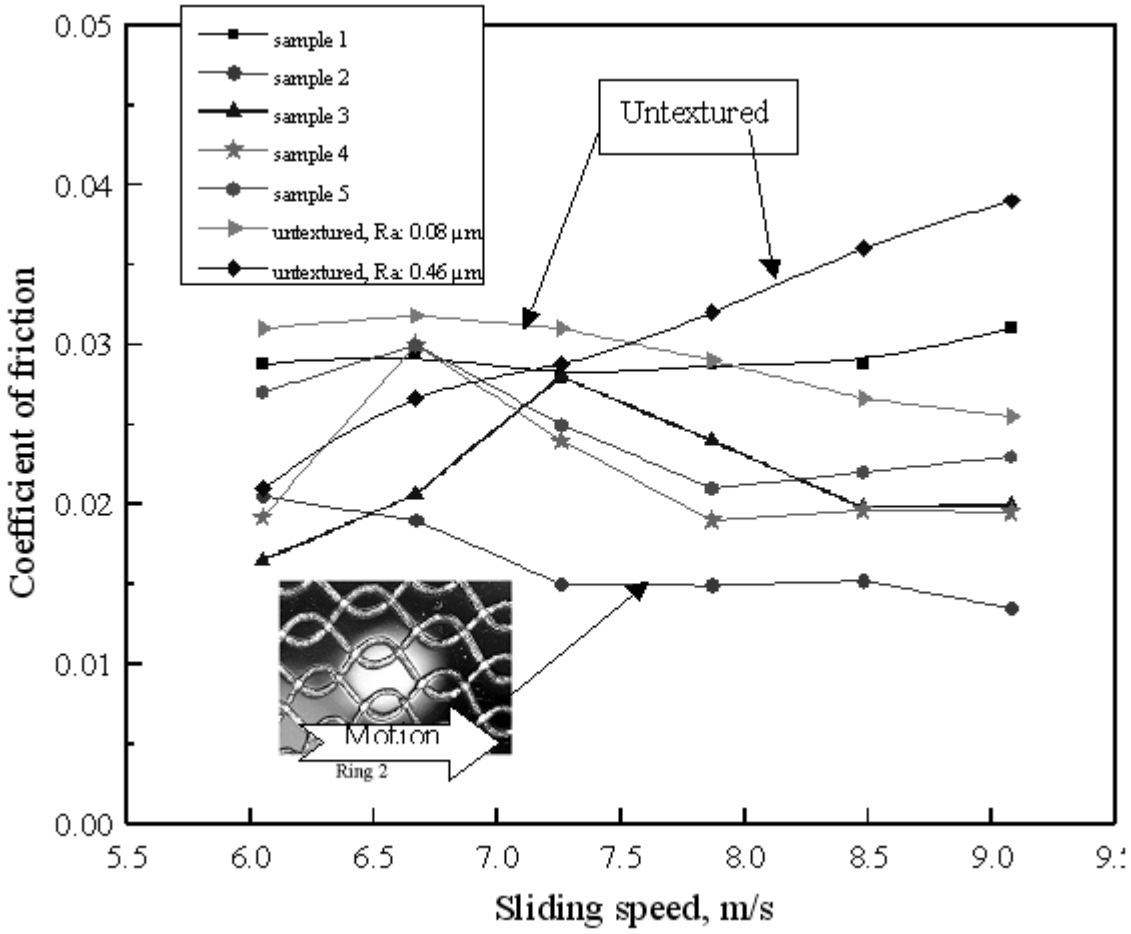

Figure 6.1.3-5: Untextured surfaces exhibited higher friction coefficients than many of the textured surfaces.

Use of textures to reduce friction requires much greater knowledge regarding selection, orientation, texture frequency, and specific texture geometry as it is related to the direction of motion. The best approach to develop and manipulate texture orientation is by computer simulation using virtual textures. The existing EHL model described under the Model Development Status section above was used at Eaton to assess some of textures and their effect on friction. A more focused effort was initiated at Northwestern for the modification of the model to accommodate surface texturing.

Textured Surfaces, Nanoscratching Friction.

The effect of surface textures on the friction of Poly(dimethylsiloxane) (PDMS) elastomer was investigated at both macro and micro scales using a nanoindenter. Friction tests were conducted by means of a stainless-steel bearing ball with a diameter of 1.6mm (macro scale tests) and a Rockwell diamond tip with a radius of curvature of 25µm (micro scale tests), under normal loads of 5, 10, and 25 Nm and with a sliding speed of 1µm/sec. The coefficient of friction (COF) obtained using the textured surface is found to be much lower than that using the flat surface of the same material, and it was reduced by about 59 percent in the macro scale tests and 38 percent in the micro scale tests. COFs in different sliding directions on the groove-textured surfaces were compared, and the friction behaviors were analyzed. **Figure 6.1.3-6** below shows the grooved

surfaces and friction coefficient comparison, **Figure 6.1.3-7**, for these surfaces. Perpendicular grooves yield a lower friction.

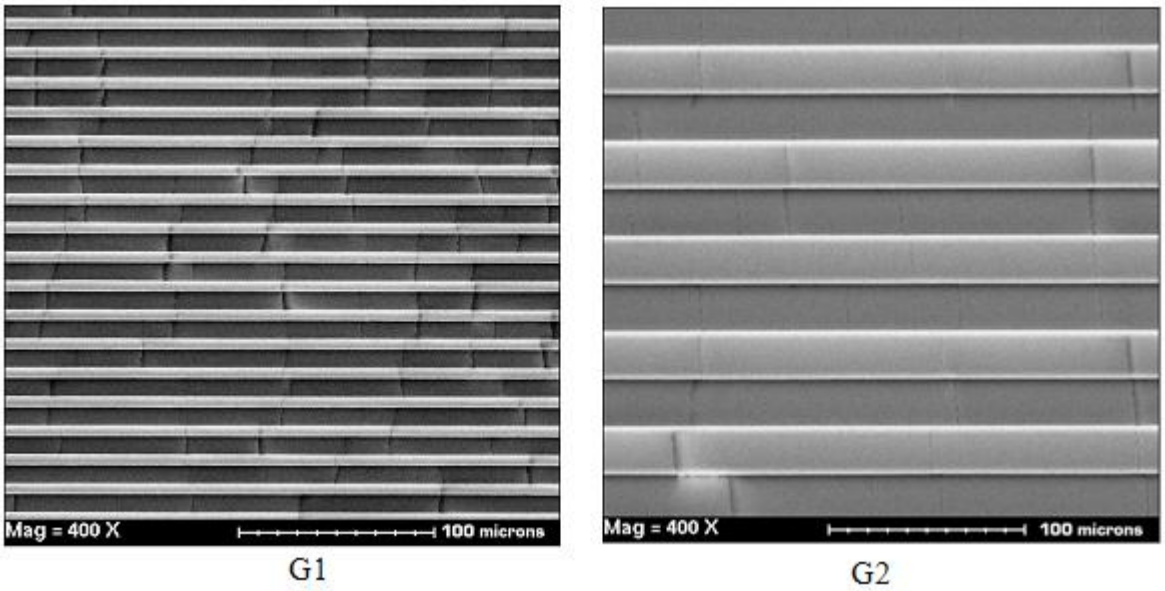

Figure 6.1.3-6: Narrow and wide grooves create surface textures to minimize friction. Perpendicular grooves lower friction.

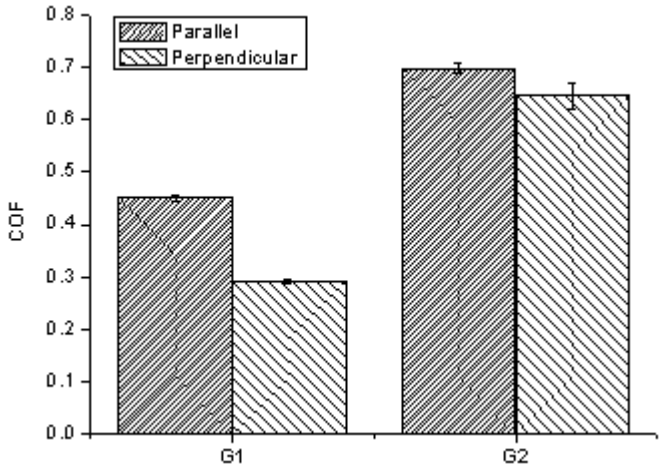

Figure 6.1.3-7:Friction coefficients are shown for the two grooved surfaces in Figure 6.1.3-6

6.1.4 Selection of Lubricants

In 2006 during this project Eaton introduced the new, commercial transmission lubricant Roadranger SAE 50 Rev 7, replacing the former lubricant Roadranger Rev 6 E500 CD50. Falex 4-ball tests at Eaton showed that the new Rev 7 fluid reduced friction by more than 10 percent compared to its predecessor, see **Figure 6.1.4-1.**

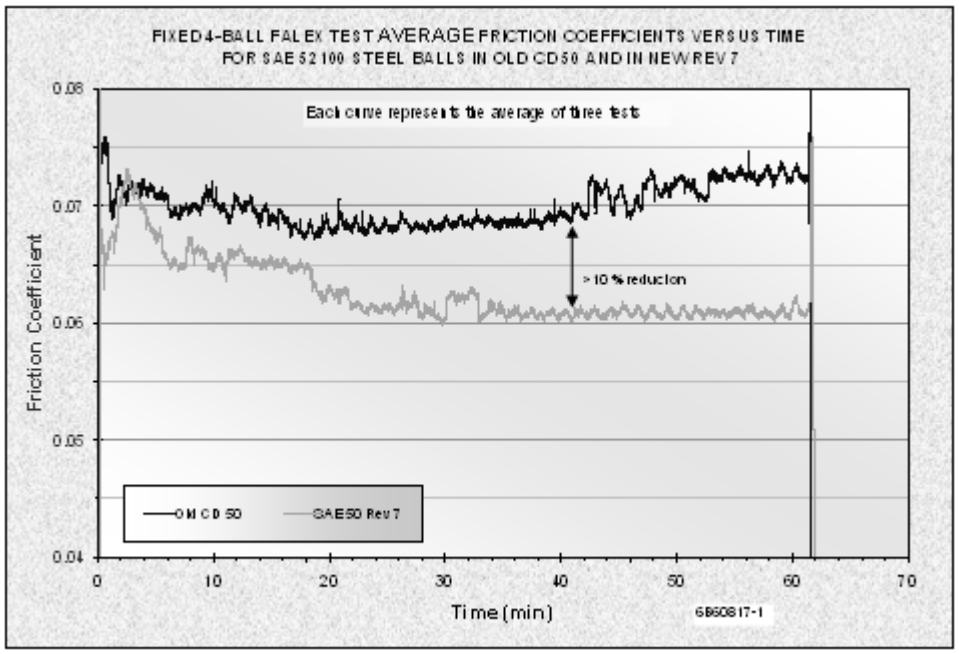

Figure 6.1.4-1: Roadranger SAE 50 Revision 7 oil reduces the friction by 10 percent compared to the older transmission fluid CD50.

Lubricant and Surface Roughness Effects on Friction

Throughout this project numerous lubricants and additives were evaluated by means of bench tests and fixture tests to document the improvements in friction coefficient. Various formulations of a Polyalphaolefin (PAO) base stock with a number of additive packages were tested using the Falex 4-ball test. Test conditions included a force of 40 kilograms and a lubricant temperature of 116 to 121 degrees C. Results of these 4-ball tests are shown in **Table 6.1.4-1** below. For a high contact stress test, the baseline Rev 7 fluid exhibits a friction coefficient of 0.066 and an average wear scar diameter of 0.44 mm. Under the same conditions an older, commercial transmission fluid, Mobil SHC 50, produced a larger friction coefficient of 0.123 coupled with a larger wear scar diameter of 0.64 mm. When a number of PAO-based formulations were 4-ball tested against the Rev 7 fluid, the results were surprising. Adding a friction modifier and various anti-wear additives to the PAO base stock produced fluids that displayed significantly reduced friction and reduced wear compared to the Rev 7 baseline. The

reduction in friction coefficient to a value of 0.038 represents a 42 percent improvement. The reduction in wear to a scar diameter of only 0.33 mm represents a corresponding improvement of 25 percent

Table 6.1.4-1: Alternative, experimental oil formulations show significantly reduced friction coefficients and wear scars compared to the commercial oils Roadranger SAE 50 Revision 7 and Mobil SHC 50.

LUBRICANT COMPOSITION	FRICTION COEFFICIENT	WEAR SCAR DIAMETER (mm)
Roadranger SAE 50 Rev 7 Baseline	**0.066**	0.44
Mobil SHC 50 tested 5/25/07	**0.123**	0.64
PAO + CK3D + RFF2 + RFY2 + H121	**0.038**	0.33
PAO + CK3D + RFF2 + RFY3 + H121	**0.039**	0.33
96-PAO + 1-CK3D + 2-RFF2 + 1-RFN3	**0.039**	0.34
96-PAO + 1-CK3D + 2-RFF2 +1-RFV2	**0.040**	0.34
PAO + CK3D + RFF2 + RFV2 + JDF4 + H1.221.3	**0.040**	0.34
96-PAO + 1-CK3D + 2-RFF2 + 1 RFN2	**0.040**	0.35
94-PAO + 2-RFF2 + 2 RFH3 + 2-CK3D	**0.040**	0.40

The synergistic benefit of lubricant and surface roughness control was advanced in this project. With Wedevan tests, Caterpillar identified two of eighteen lubricants as the best low friction choice. Synthetic base-stocks (Oil #1) provided high efficiency at high speed hydrodynamic lubrication while certain lubricants (Oil #11) with mineral oil base-stock provided high efficiency at low speed where boundary or mixed lubrication was prevalent. In order to develop better low friction lubricant for truck drive axles, new lubricants with potential to achieve further friction reduction in both high and low speed were identified and tested using the same testing protocol.

Comparing with the best low friction lubricants (Oil #1 and #11), one of the new lubricants, Oil #20, achieved lower traction coefficient at both high and low speeds. Additional traction reduction, more than 30 percent compared with the baseline Oil #18 was achieved by applying Oil #20 with coated surfaces against IF (isotropic finished) surfaces, **Figure 6.1.4-2.**

FZG gear efficiency testing also was completed in Year 3 with the new candidate lubricant designated as Oil #20. As illustrated below Oil #20 provides significantly better gear mesh efficiency than either of the best candidates from Year 2 and even greater benefit over the baseline Oil #18, **Figure 6.1.4-3.**

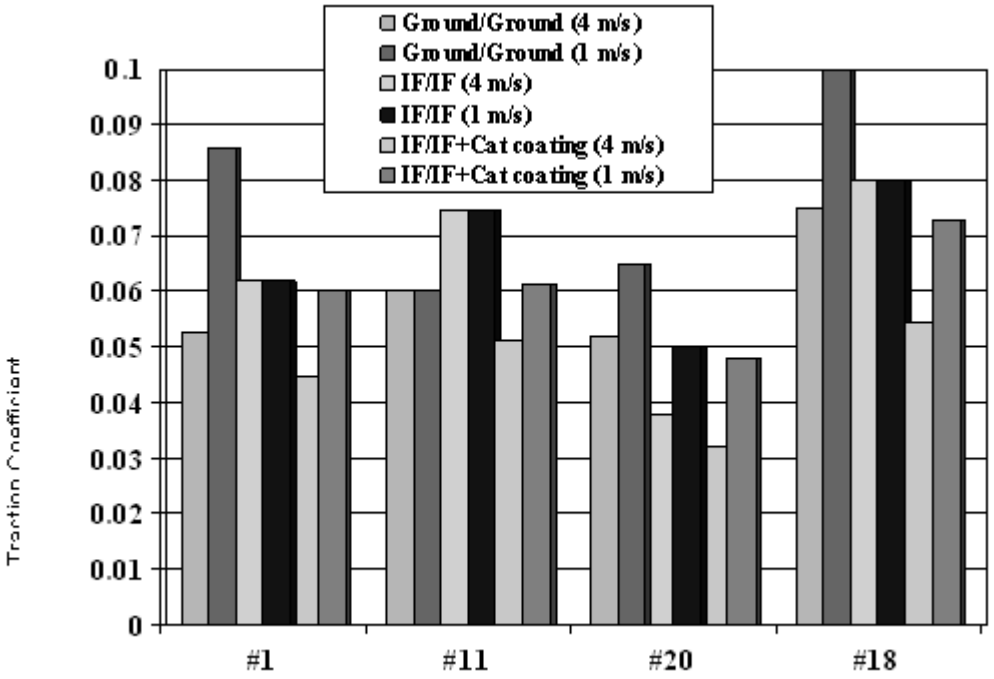

Figure 6.1.4-2: Caterpillar found that the new Oil #20 produced lower friction than either the standard petroleum-based Oil #11 or the synthetic Oil #1.

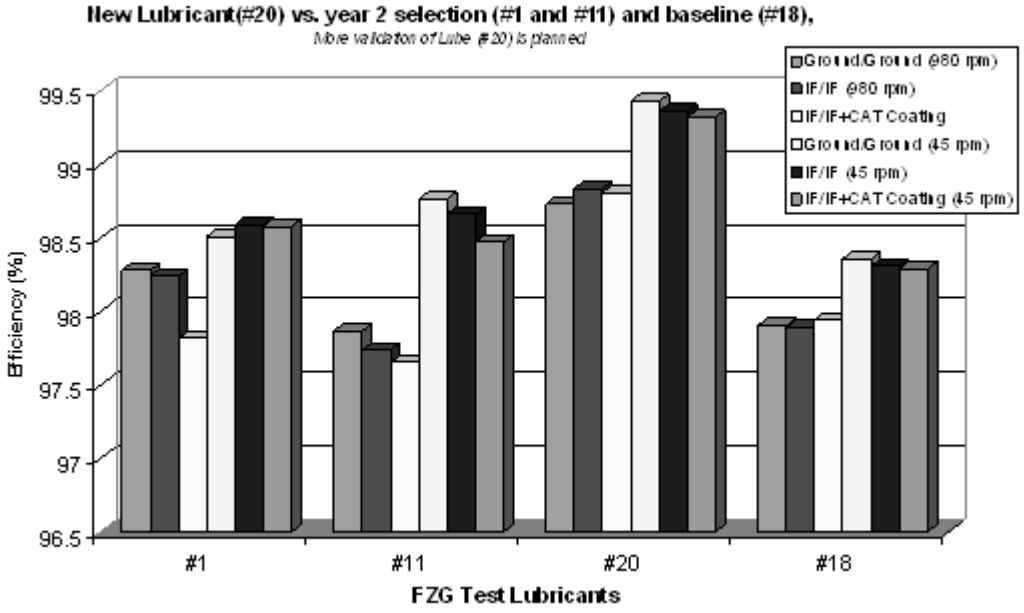

Figure 6.1.4-3: FZG testing showed that Oil #20 produced the highest gear mesh efficiency.

Comparing power loss of the baseline oil #18 to that of candidate #20 at a speed of 45 rpm, a power loss reduction of over 50 percent is seen. A similar reduction is seen at the higher speed of 980 rpm.

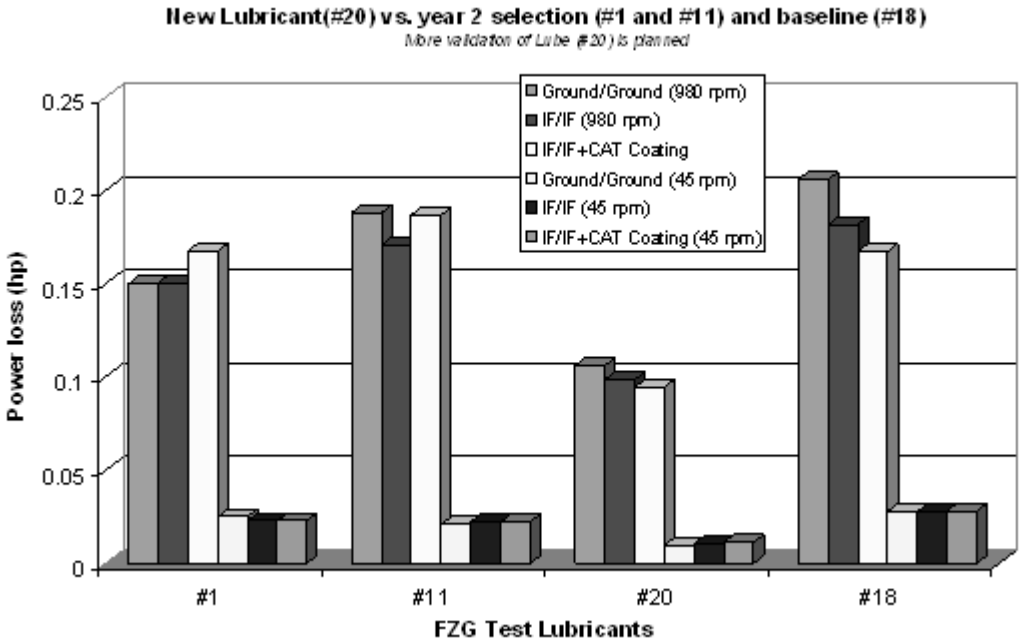

Figure 6.1.4-4: Power loss is significantly reduced with the new Caterpillar Oil #20.

6.1.5 Boundary Lubrication and Friction Modeling

Boundary friction is a most significant component of the total friction generated under the mixed lubrication regime. As a team member, Argonne had the best capabilities to conduct characterization of boundary films and associated friction. To that end, an in-situ boundary film X-ray characterization facility had been developed and functionality established. **Figure 6.1.5-1** below shows results of boundary film formation (Zn content) and associated friction measured during a *"steel ball-on-steel disk"* tribological testing.

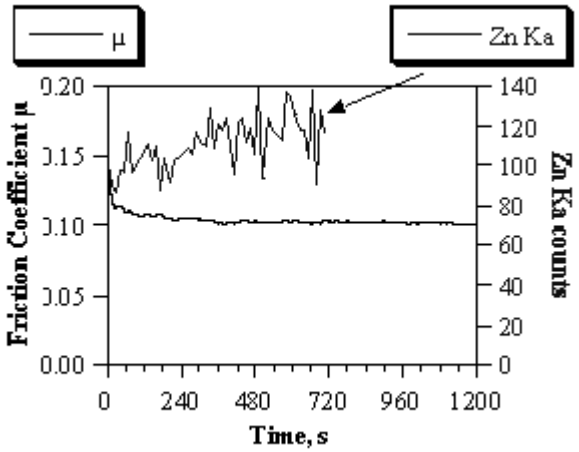

Figure 6.1.5-1: Formation of Zinc boundary film during ball-on-disk test.

Regarding boundary friction modeling, the approach of a "look-up" table with numerical modeling proved complex. Data was generated for selected lubricants and additives under specific tribological conditions of interest and interpolations between adjacent data points was useful. The initial look-up table from Argonne is presented below in **Table 6.1.5-1.**

Table 6.1.5-1: Look-up table for boundary friction for oils at room temperature

Oil	$\mu_{1cm/s}$	$\mu_{0.1cm/s}$	$\mu_{1cm/s}$	$\mu_{5cm/s}$	$\mu_{10cm/s}$	$\mu_{1cm/s}$ (Long run)	$\mu_{0.1cm/s}$	$\mu_{1cm/s}$	$\mu_{5cm/s}$	$\mu_{10cm/s}$
Anglamol	0.129	0.130	0.128	0.122	0.117	0.120	0.138	0.129	0.115	0.108
Std. Deviation:	*0.007*	*0.008*	*0.007*	*0.006*	*0.005*	*0.005*	*0.005*	*0.006*	0.008	*0.008*
Texaco 2276	0.118	0.116	0.117	0.116	0.114	0.118	0.118	0.119	0.114	0.112
	0.006	*0.005*	*0.005*	*0.005*	*0.004*	*0.004*	*0.004*	*0.005*	*0.005*	*0.005*
Optimol Optgear	0.125	0.128	0.124	0.117	0.111	0.110	0.111	0.109	0.107	0.106
	0.012	*0.013*	*0.009*	*0.005*	0.004	0.011	0.124	*0.010*	*0.007*	*0.005*
Mobillube HD LS	0.112	0.104	0.1120	0.112	0.111	0.109	0.095	0.108	0.110	0.108
	0.004	0.004	*0.004*	*0.004*	*0.003*	*0.003*	*0.003*	*0.003*	*0.004*	*0.004*
Circle 3	0.113	0.111	0.114	0.113	0.113	0.116	0.112	0.115	0.114	0.113
	0.009	*0.015*	*0.009*	*0.005*	*0.005*	*0.004*	*0.005*	*0.004*	*0.005*	*0.005*
Roadranger 50	0.128	0.131	0.126	0.118	0.114	0.123	0.131	0.124	0.118	0.115
	0.011	*0.013*	*0.009*	*0.007*	*0.006*	*0.005*	*0.005*	*0.005*	*0.006*	*0.006*
Syntec 75w90	0.122	0.123	0.123	0.120	0.117	0.125	0.128	0.125	0.120	0.115
	0.008	*0.009*	*0.007*	*0.006*	*0.006*	*0.005*	*0.005*	*0.005*	*0.006*	*0.007*
Red line Shockproof Gear Oil Light	0.110	0.104	0.109	0.111	0.110	0.108	0.101	0.108	0.108	0.107
	0.007	*0.009*	*0.006*	*0.005*	*0.004*	*0.004*	*0.005*	*0.004*	*0.004*	*0.005*

Caterpillar conducted a limited experimental study on boundary film formation. Effects of molybdenum phosphorodithioate and molybdenum phosphorodithioate plus zinc diamyldithiocarbamate on the boundary lubrication film formed on the worn surface were studied, using four-ball as well as pin-on-flat test geometries under fully submerged lubricant and oil dropping conditions, respectively. Based on the limited results of lab tests, it was found

that boundary film composition is dependent upon the condition under which the film was generated. Mild wear primarily led to phosphate formation whereas extreme pressure conditions will favor the growth of sulfides. It was also found that boundary film thickness as well as relative distribution of compounds constituting the film impact friction and wear properties.

Mixed-EHL (Lubrication) and Thin-Film Model

A novel 3-D line contact EHL model was developed through collaboration between Eaton and Northwestern University. The three-dimensional, line-contact, mixed-elastohydrodynamic lubrication model (3D L-EHL), designed specifically for solving mixed-lubrication problems involving line contacts, was used to analyze friction anisotropy with respect to surface topography. The results for sample rough surface cases have demonstrated that this 3D L-EHL model is effective and robust, capable of simulating line-contact mixed-EHL problems with 3D deterministic surfaces under severe operating conditions without requiring excessive computational cost or sacrificing the numerical resolution in the contact length direction. This model is a fundamental tool for gear performance analysis because gear tooth contacts, spur and helical, are all line contacts of 3-D engineering surfaces.

The three-dimensional numerical model for the simulation of the contacts of elastically dissimilar materials leads to surface real contact and stick areas, pressure, tangential tractions, and the subsurface stress field. It is verified through the comparison of the numerical results with analytical solutions. From its initial inception, the solution stability and convergence speed of the 3-D line contact EHL model improved substantially.

In order to validate this line contact EHL model, an un-lubricated line contact is analyzed with the current contact model and a 2D contact analysis. A smooth-surface EHL solution obtained from the current model is compared with that from a conventional 2D EHL model. Good agreements are observed. **Figures 6.1.5-2 and 6.1.5-3** show two examples, a line contact involving an isotropic sinusoidal rough surface and a line contact involving a transverse sinusoidal rough surface.

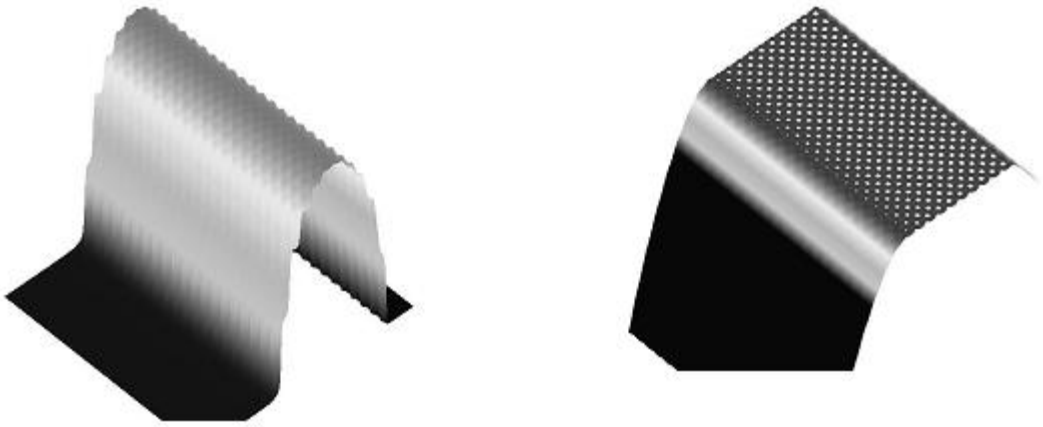

Pressure distribution Deformed surface

Figure 6.1.5-2: Mixed-EHL solution for a line-contact problem involving an isotropic sinusoidal surface.

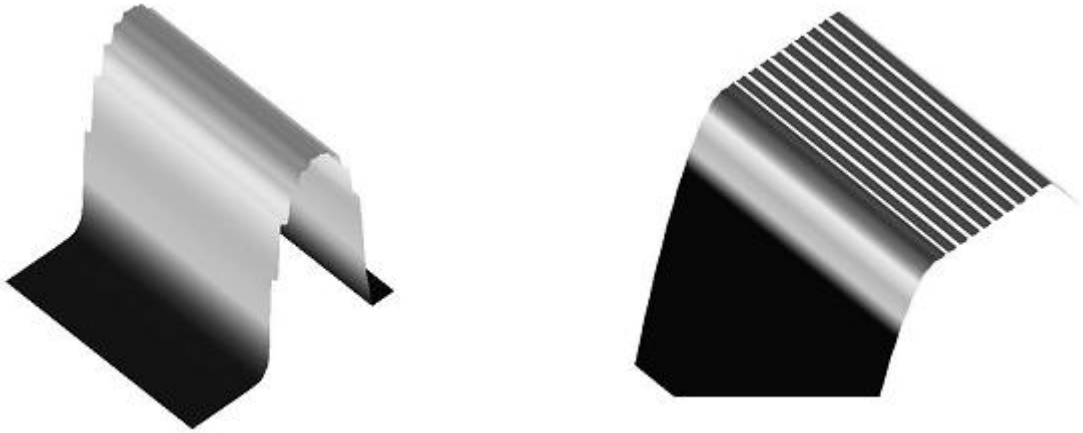

Pressure distribution Deformed surface

Figure 6.1.5-3: Mixed-EHL solution for a line-contact problem involving a transverse sinusoidal surface.

Figure 6.1.5-4 summarizes the average film thickness as affected by roughness orientations using generated sinusoidal surface. The results indicate the preference of transverse surfaces in such line contacts for lubrication enhancement.

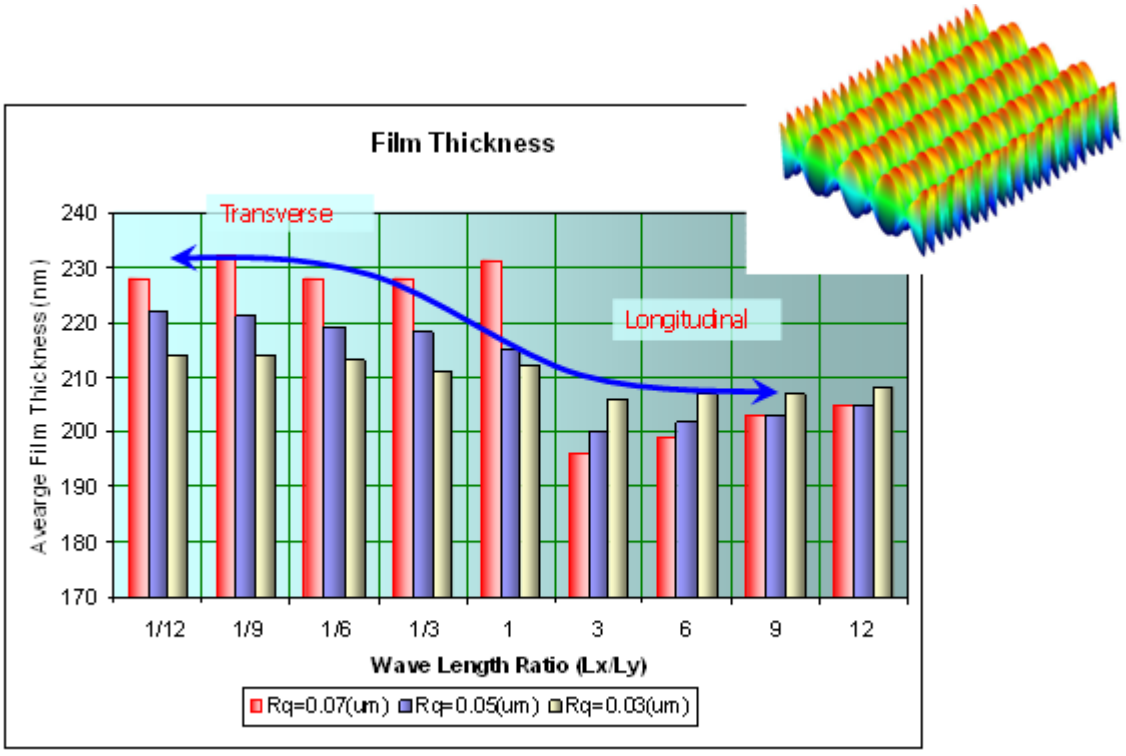

Figure 6.1.5-4: Effect of surface roughness orientation on film thickness

Lubricant Selection and Friction

An improved rough surface contact model for counterformal surface contact (gears) was developed and verified using both literature-reported data and laboratory coupon testing. The model used real surface topographies in contact captured as digitized arrays. The model computed friction, interfacial temperatures, and contact stresses for specific operating conditions and oils. The model has been used to compute friction levels for different surface conditions and effects of lubricant characteristics under different operating conditions. Examples of the results are shown in **Figure 6.1.5-5** for two lubricants, two different operating temperatures, and two different contact load conditions. Overall, the agreement between the predicted and measured traction (friction) coefficient are very good.

To improve model accuracy, Northwestern evaluated simulation methods for computing oil film thickness under varying pressures by developing a piezoviscous coefficient. For the calculation of Newtonian film thickness, the piezoviscous response was accurately quantified by a pressure related coefficient.

A similar model for conformal contacts (journal bearings) under mixed lubrication conditions also was examined. It was a macro-micro scale finite-element local enrichment (FE-LE) model for the deterministic analysis of conformal-contact mixed lubrication, in which a coarse mesh was used to determine the elastic deformation of a journal bearing surface, whilst locally refined meshes were used for the analysis of the roughness effect. A journal bearing rig was set up at Northwestern to verify the numerical model.

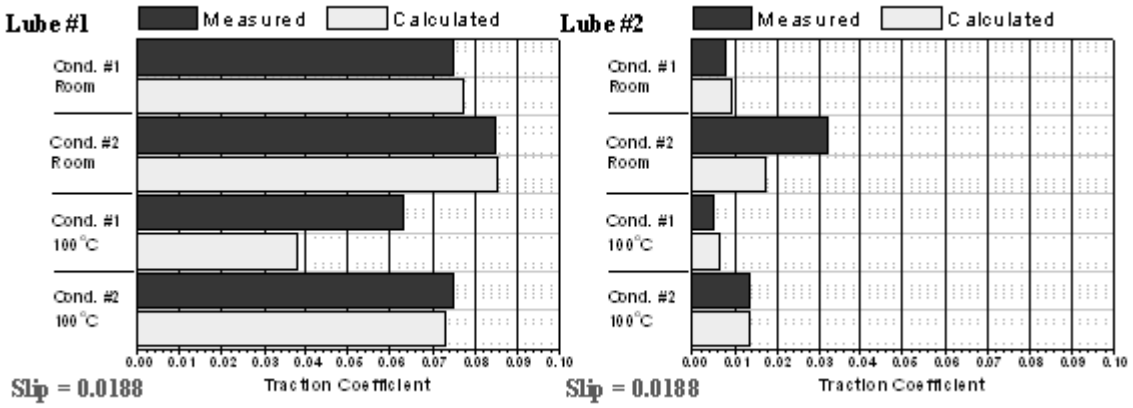

Figure 6.1.5-5: Output of rough surface contact model for two lubricants and two conditions.

6.1.6 Mixed Lubrication Models

Coating EHL-Background

Studies have been conducted on reducing the friction in the regime of mixed lubrication through introducing appropriate coatings, surface texture, and additives in lubricant. The mechanisms of friction reduction with a coating have been attributed to material properties, such as low shear strength or high hardness, that allow easy shear when contact occurs. However, little is focused

on the effect of coating on lubrication film thickness. Our studies on coating elastohydrodynamic lubrication (EHL) found that a coating may alter surface elastic deformation and affect film thickness and that a thin stiff coating is especially helpful for "hard" EHL working at the elastic piezoviscos regime whilst a thick compliant coating is useful for "soft" EHL working at the elastic isoviscos regime. Here, the stiff coating is referred to the coating with a higher Young's modules compared to its substrate while the compliant coating is vice versa. It is necessary to do a parametric study based on the newly developed coating EHL model for a wide range of load, materials, and coating/substrate material property ratios.

Coating EHL-Approach

Steady state hydrodynamic pressure is governed by the Reynolds equation expressed as follows:

$$\frac{\partial}{\partial x}\left(\varphi_x \frac{\rho h^3}{12\eta}\frac{\partial p}{\partial x}\right)+\frac{\partial}{\partial y}\left(\varphi_y \frac{\rho h^3}{12\eta}\frac{\partial p}{\partial y}\right)=U\frac{\partial(\rho h)}{\partial x} \tag{11}$$

Two flow factors φ_x and φ_y has been introduced to describe the non-Newtonian rheological behavior of the lubricant. For a lubricant with the Eyring type constitutive model (τ_0 is the Erying stress):

$$\gamma=\frac{\tau_0}{\eta}\sinh\left(\frac{\tau}{\tau_0}\right) \tag{12}$$

Two flow factors are [2]

$$\varphi_x=\cosh\left(\frac{\tau_m}{\tau_0}\right) \qquad \varphi_y=\frac{\sinh(\tau_m/\tau_0)}{\tau_m/\tau_0} \tag{13}$$

where τ_m is the shear stress in the middle layer along the rolling direction. It is determined by

$$\frac{\tau_m}{\tau_0}=\sinh^{-1}\left(\frac{\eta(u_2-u_1)}{\tau_0 h}\right) \tag{14}$$

For the Newtonian model, $\gamma=\tau/\eta$, the two flow factors reduce to $\varphi_x=\varphi_y=1$.

The gap between two deformed smooth surfaces is given below:

$$h=h_0+\frac{x^2}{2R}+\frac{y^2}{2R}+u_1(x,y)+u_2(x,y) \tag{15}$$

where u_1 and u_2 are the elastic deformations of two surfaces.

The pressure-viscosity relationship is described by the Barus equation:

$$\eta = \eta_0 \exp(\alpha p) \tag{16}$$

The pressure-density relationship is described by the Dowson-Higgison equation:

$$\rho = \rho_0 (1 + \frac{0.6 \times 10^9 p}{1 + 1.7 \times 10^9 p}) \tag{17}$$

The difference between uncoated and coated EHL lubrication model is the elastic deformation. For an uncoated half surface, the normal displacement by a pressure distribution is controlled by the Boussinesq integration

$$u_i(x, y) = \frac{1}{\pi E_i^*} \iint_{\Omega} \frac{p(\xi, \zeta)}{\sqrt{(x-\xi)^2 + (y-\zeta)^2}} \mathrm{d}\xi \mathrm{d}\zeta \tag{18}$$

Where

$$E_i^* = \frac{E_i}{1 - \nu_i}$$

The Green's function (integral kernel) for the convolution is

$$h_i(x, y) = \frac{1}{\pi E_i^* \sqrt{x^2 + y^2}} \tag{19}$$

The corresponding frequency response function (FRF) in frequency domain is

$$\tilde{\tilde{h}}_i(m, n) = \frac{2}{E_i^* \sqrt{m^2 + n^2}} \tag{20}$$

For a coated half surface, the explicit Green's function is not available for the normal displacement in space domain. But its FRF is available in the frequency domain [O'Sullivan and King, 1988].

$$\tilde{\tilde{g}}_i(m, n) = \frac{2}{E_{ic}^* w} \frac{1 + 4 w d_i \kappa \vartheta - \lambda \kappa \vartheta}{1 - (\lambda + \kappa + 4\kappa w^2 d_i^2)\vartheta + \lambda \kappa \vartheta^2} \tag{21}$$

Where

$$\kappa = \frac{\mu - 1}{\mu + (3 - 4\nu_{ic})} \qquad \lambda = 1 - \frac{4(1 - \nu_{ic})}{1 + \mu(3 - 4\nu_{is})} \qquad w = \sqrt{m^2 + n^2}$$

$$E_{ic}^* = \frac{E_{ic}}{1 - \nu_{ic}} \qquad \mu = \frac{E_{ic}(1 + \nu_{is})}{E_{is}(1 + \nu_{ic})} \qquad \vartheta = \exp(-2 w d_i)$$

In two limit cases, Eq. (21) will reduce to Eq. (20). One is to use the same material for both coating and substrate, that is $E_{ic}=E_{is}$ and $v_{ic}=v_{is}$, and the other is zero coating thickness for $h=0$. It should be noted that the above equations are all valid for one surface. If two surfaces are involved in contacts, the total normal elastic deformation is the superposition of values of two surfaces.

If the FRF in Eq. (21) is directly discretized in the size of the computational range in the frequency domain, application of the IFFT algorithm to get the convolution of normal displacement may result in a large computational error due to the aliasing phenomenon in the frequency domain. Therefore, in a more efficient and accurate way, FRF should be discretized in an extended domain in the frequency domain first. The extended domain is about 6-10 times of the original computational domain, which depends on different characteristic of FRF. The singularity of FRF at $w=0$ is overcome by the Gauss quadrature integration. Applying IFFT to the discrete matrix of FRF, the influence coefficients (ICs) are picked up from the transformed matrix. Once the ICs are obtained, elastic deformation is obtained by the DC-FFT fast algorithm. The advantage of this algorithm is that the most accurate solutions are obtained using the shortest time [Liu S.B. et al., 2000].

The EHL solver is based on the Hu & Zhu unified mixed-lubrication algorithm [Hu and Zhu, 2000; Zhu and Hu, 2001]. The Poiseuille flows, the left side of the Reynolds equation, are discretized by the 2nd-order central scheme. The 2nd-order backward scheme is employed to treat the Couette flow. In order to improve the convergence, the leading diagonal element of coefficient matrix is adjusted to satisfy the Dominance Theory. The contact pressure is obtained by the reduced Reynolds equation, so that the contact pressure and lubrication pressure can be solved simultaneously though the unified equation system. The discrete linear system is solved by the linear relaxation method.

Coating EHL-Results

The coating EHL point contact (C-EHL-P) model has been verified by two comparisons. In the first comparison, the elastic deformations from two approaches were compared: One from the Green's function in space domain, and the other from the response function in frequency domain. Through this comparison, an extension of twelve times the original domain was determined for the second approach with the relative error of elastic deformations between the two approaches smaller than 0.3 percent. Further validation of the model is conducted by comparing to Sullivan and king' coating results in a dry contact. The present mixed EHL model can simulate the dry contact results approximately by setting the entrainment speed to a very small value, such as U=0.0001m/s. Good agreements in the maximum contact pressure and contact radius were observed through the further comparison.

Simulations in the study were conducted based on an uncoated moving ball against a coated stationary flat. The computational parameters are listed in **Table 6.1.6-1.** For the contact without coating, the load, ball radius and the material parameters for the ball and the flat surfaces result in a Hertzian contact radius of 0.24 mm and maximum pressure of 0.86 GPa. The Hertzian contact radius and maximum Herzian pressure are used for normalization when a coating is involved. The Young's modulus of the coating varies from 1/4 of that of the substrate to 4 times of that. The dimensionless coating thickness increases gradually form 0.1 to 3.

Table 6.1.6-1: Calculating parameters in present simulation

Parameters	Value	Unit
Load, w	23	N
Young's modulus of steel ball, E_1	200	GPa
Poisson's ratio of both surfaces, $\nu_1, \nu_{2S}, \nu_{2C}$	0.3	
Young's modulus of the substrate on flat disk, E_{2s}	200	GPa
Young's modulus of the coating on flat disk, E_{2c}	(0.25, 0.5, 2, 4) * E_{2s}	GPa
Thickness of the coating on the flat disk, h_{2c}	(0.1~3.0)* a	mm
Ball radii, R	19	mm
Hertzian contact radii, a	0.24	mm
Maximum Hertzian contact pressure, p_h	0.86	GPa
Viscosity at inlet temperature, η_0	0.096	Pa.s
Pressure-viscosity coefficient, α	18.2	1/GPa

Coating Effect on Maximum Pressure and Contact Radius

As shown in **Figures 6.1.6-1 and 6.1.6-2**, a hard coating increases the maximum pressure and reduces the nominal contact radius while the situation is opposite for a soft coating. However, the change caused by the soft coating is larger than that by the hard coating even if the changes in the Young's modulus are identical for both the soft and hard coatings. As the coating thickness increases, the maximum pressure and contact radius gradually approach the limit where the substrate is replaced by the coating completely. It is shown that as the coating thickness approaches three times the Hertzian contact radius, the coating almost completely controls the behavior of the total elastic deformation.

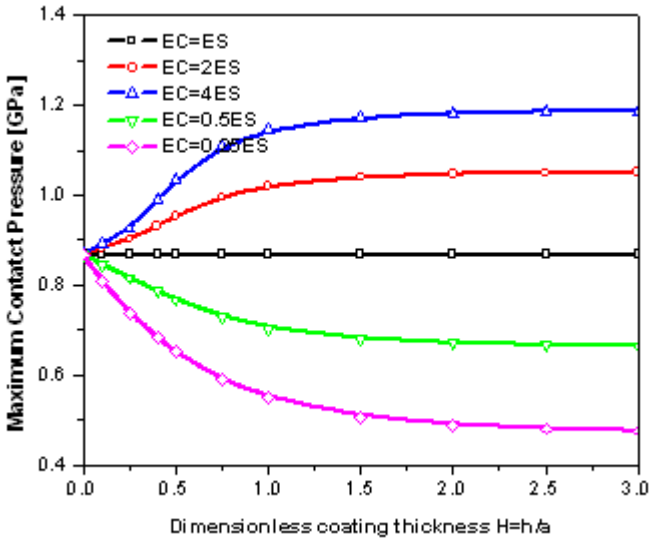

Figure 6.1.6-1: Effect of coating on maximum contact pressure

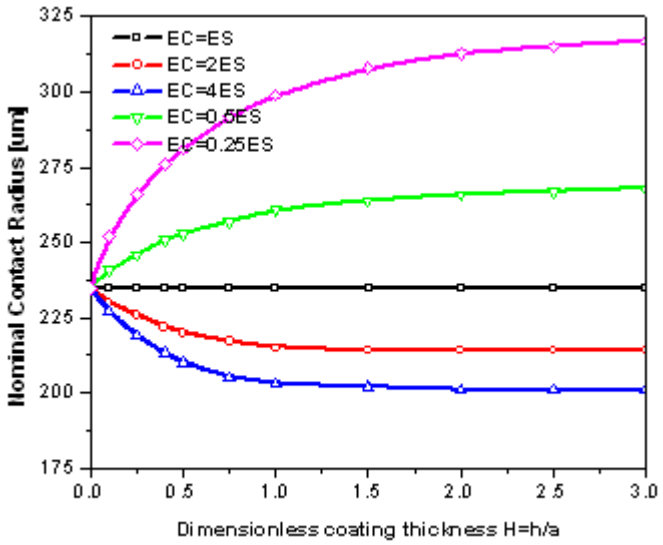

Figure 6.1.6-2: Effect of coating on nominal contact radius

Coating Effect on Friction Coefficient

Figure 6.1.6-3 presents the effect of coating on the friction coefficient in lubrication film. The friction coefficient is calculated by the integration of the shear stress on the ball surface and divided by the load. It is found that the hard coating intends to increase the friction coefficient while the soft coating to reduce the friction coefficients. But the influence of the soft coating is larger than that of the hard coating. The variation of the friction coefficient, that is the change of the shear stress, is related to the viscosity variation as well as different shear-thinning model. In the analysis of coating EHL for line contacts [Elsharkawy and Hamrock, 1994] using a circular limiting shear strength model, it was also found that the hard coating increases the friction

coefficient while the soft coating reduces the friction coefficient and the influence of the soft coating is larger than the hard coating.

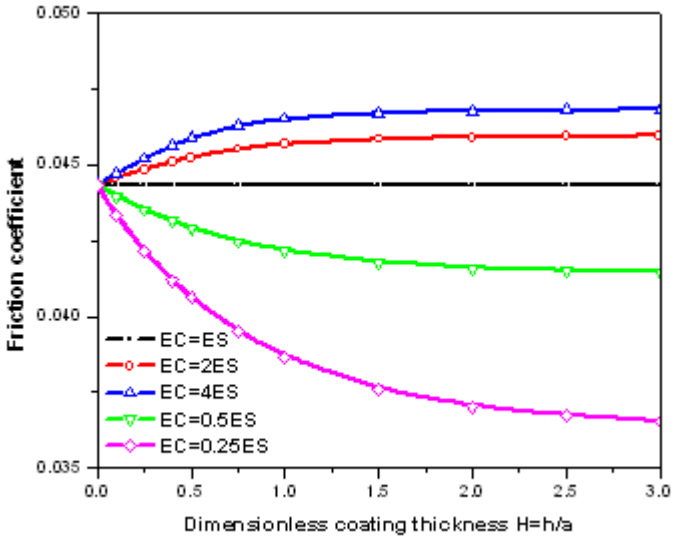

Figure 6.1.6-3: Effect of coating on friction coefficient in lubrication film

Effect of Coating on Film Thickness

Figures 6.1.6-4 and 6.1.6-5 present the coating influence on film thickness. For central film thickness, as shown in **Figure 6.1.6-4**, a general trend is that a soft coating tends to increase h_{cen} while a hard coating tends to decrease h_{cen}. The variation of h_{cen} is larger for soft coatings. However, when the coating thickness is very thin, h_{cen} first undergoes an inverse trend in contrast to that for the thick coating cases. The change in direction of the film thickness curve will be referred to as the turning trend. This type of variation gets more significant for h_{min}, as shown in **Figure 6.1.6-5**. A large turning can be observed in the regime of thin coating thickness. This turning tends to block the normal trend of coating effect and cannot be explained by any film thickness equation. As a result, h_{min} is nearly constant when the coating thickness is sufficiently thick, except for the case for very soft coatings.

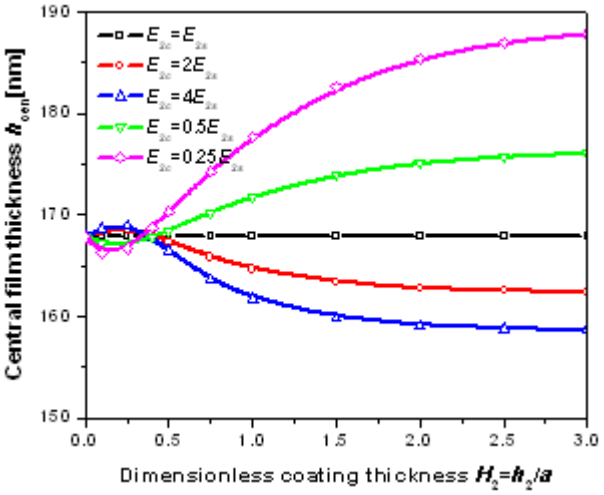

Figure 6.1.6-4: Effect of coating on central film thickness

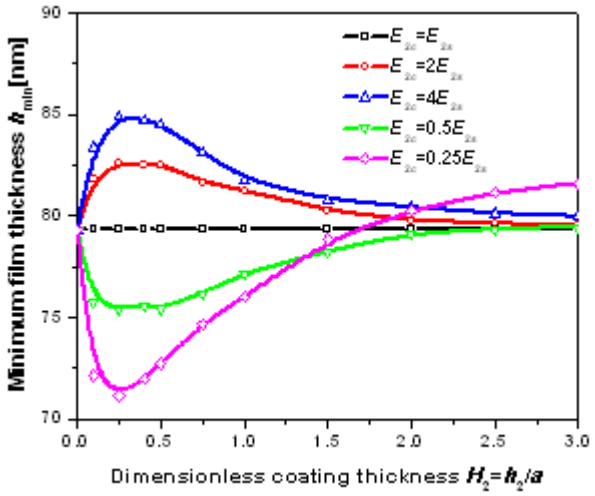

Figure 6.1.6-5: Effect of coating on minimum film thickness

Effect of Coating in Various Speed

The effect of speed on the coating EHL is explained in **Figure 6.1.6-6** by comparing two cases of u=0.2m/s and u=2m/s while other parameters are held constant. In order to increase comparability, the vertical coordinate is replaced by the normalized terms instead of the real values. The value in the corresponding uncoated EHL case is selected as the normalization parameter. **Figure 6.1.6-6** indicates that there is an overall increase in hcen from 168 nm to 689 nm due to the increase in speed. Furthermore, the influence of coating increases and the turning trend in the thin film disappears in high speed cases. The observation is further confirmed by the variation of hmin, as shown in **Figure 6.1.6-7.** The original large turning in low speed cases gradually reduces with speed increase. It is interesting to see similar curves for "h_{cen}" in low speed cases and "h_{min}" in high speed cases.

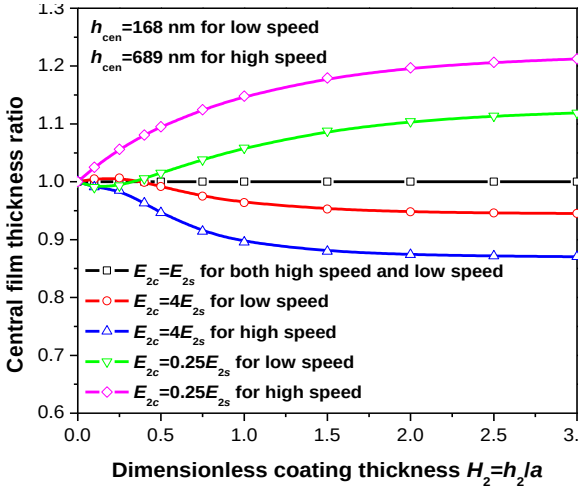

Figure 6.1.6-6: Central film thickness ratio

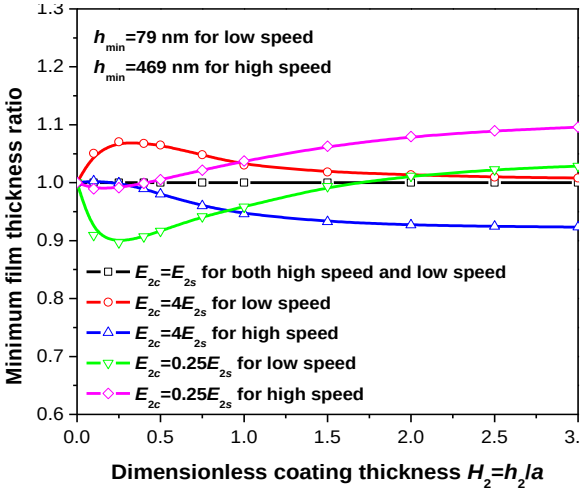

Figure 6.1.6-7: Comparison between the low-speed and high-speed cases

Effect of Coating in Various Load

Two cases at the same speed of 2m/s but different load of 100N and 800N are also compared in **Figures 6.1.6-8 and 6.1.6-9** to reveal the load effect. As shown in **Figure 6.1.6-8** for h_{cen}, the coating influence in the heavily loaded cases becomes more significant, as compared to that in the lightly loaded cases. For h_{cen} as shown in **Figure 6.1.6-8**, the turning trend is completely removed due to the increased load. However, for h_{min} in **Figure 6.1.6-9**, the turning effect becomes stronger for the heavily loaded cases.

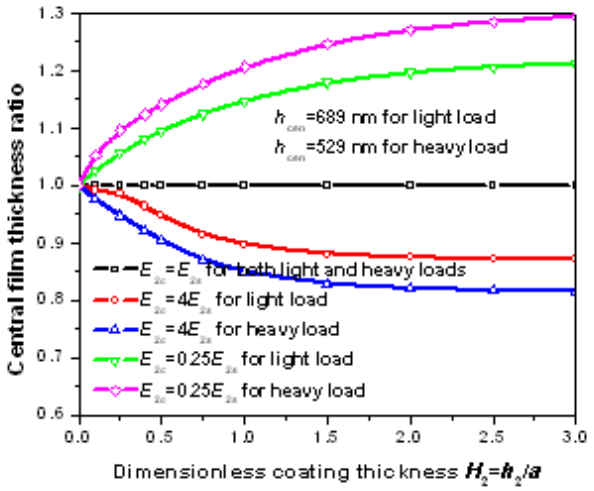

Figure 6.1.6-8: **Central film thickness ratio**

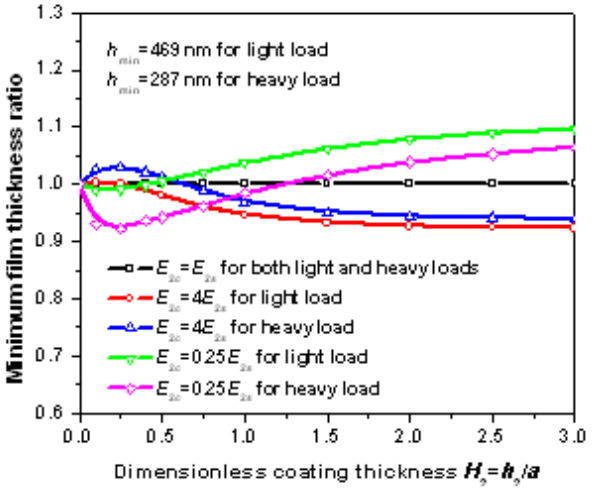

Figure 6.1.6-9: Minimum film thickness ratio

These figures compare lightly loaded and heavily loaded cases.

Effect of Coating Using the Newtonian Rheological Model

Figure 6.1.6-10 and 6.1.6-11 presents the influence of rheological model consideration. It is found that when using the Newtonian model the turning trend is enlarged but the magnitude of variation is not significant.

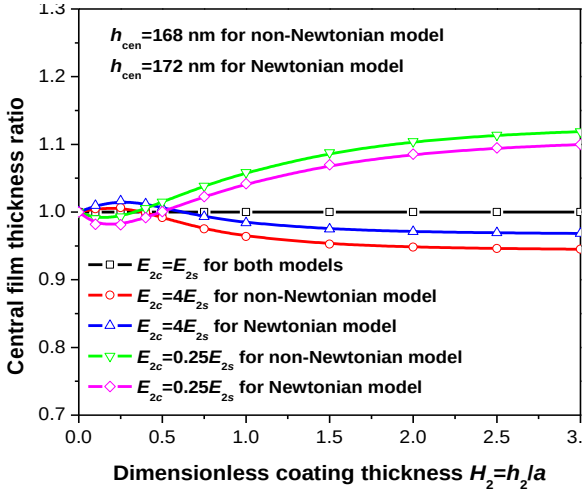

Figure 6.1.6-10: Central film thickness ratio

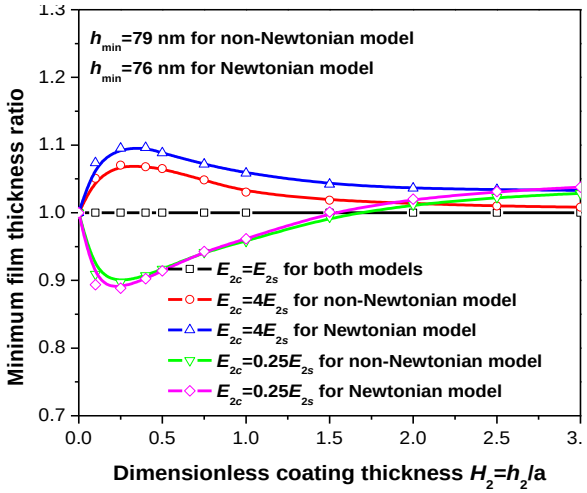

Figure 6.1.6-11: Minimum film thickness ratio

These figures compare the non-Newtonian and Newtonian cases.

Effect of Coating in Reduced Pressure Viscosity Effect

Elsharkawy & Hamrock concluded that the turning trend in the thin film regime for coating EHL resulted from the pressure viscosity effect [Elsharkawy and Hamrock, 1994]. In this research, the pressure viscosity effect was investigated by reducing the value of the pressure-viscosity coefficient by a factor of 1000. **Figure 6.1.6-12 and 6.1.6-13** shows the results, where the turning trend was completely removed for both h_{cen} and h_{min}. Moreover, the influence of coating turns to be more significant in the cases with the smaller pressure-viscosity coefficient value. For the cases with the higher coefficient value, the influence of coating does not exceed a maximum of 30 percent for the high speed and heavily loaded cases. However, if the pressure viscosity coefficient is reduced by a factor of 1000, the influence of coating increases by 50 percent even for the low speed and lightly loaded cases. This analysis reveals an important approach to improve h_{min} and avoid wear by using a soft coating and increasing the compliance. It also suggested a method to design lubricants and lubrication for film thickness enhancement. Soft coatings have a more significant influence on the EHL in the elastic isoviscous regime than the conventional EHL in the elastic piezoviscous regime. The comparison in **Figure 6.1.6-13** further verifies that the pressure viscosity effect tends to counteract the effect of coating.

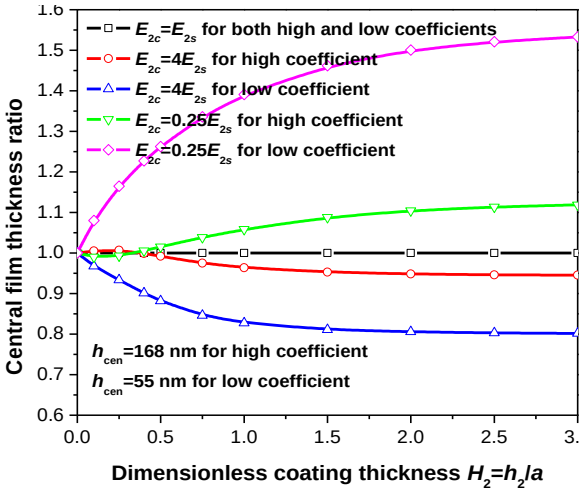

Figure 6.1.6-12: Central film thickness ratio

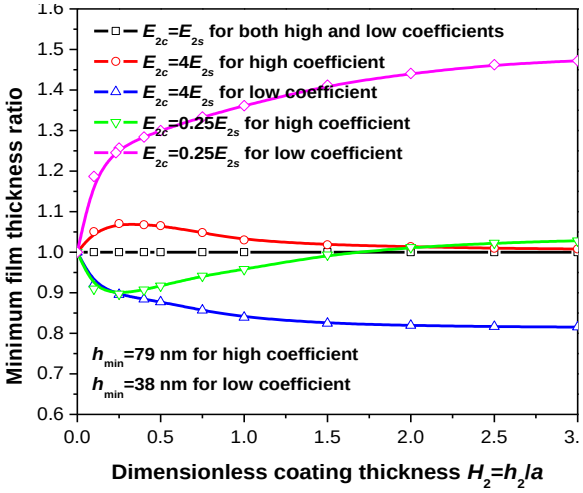

Figure 6.1.6-13: Minimum film thickness ratio

These figures compare the high coefficient and low coefficient cases.

Two dimensionless parameters *M* and *L* suggested by Moes and Bosma [1972] are employed as independent variables to describe the EHL behaviors since no redundant equalities are introduced into the system. Their definitions are

$$M = \frac{w}{E'R^2}\left(\frac{\eta_0 u}{E'R}\right)^{-3/4} \tag{76}$$

$$L = \alpha E'\left(\frac{\eta_0 u}{E'R}\right)^{-1/4} \tag{77}$$

Here *M* and *L* denotes the working conditions for uncoated EHL contact because the reduced Young's modulus, *E'*, is used.

Two dimensionless coating parameters are employed to describe the coating properties. One is the dimensionless coating thickness

$$H_2 = \frac{h_{2c}}{a} \tag{78}$$

The other is the material parameter ratio of the coating – substrate system

$$R_2 = \frac{E^*_{2c}}{E^*_{2s}} = \frac{1-\nu^2_{2s}}{1-\nu^2_{2c}} \frac{E_{2c}}{E_{2s}} \tag{79}$$

A parametric study is conducted to investigate the effect of dimensionless load *M*, dimensionless material parameter *L* and coating material parameter ratio R_2 on the minimum film thickness improvement based on a coating EHL model for point contacts developed by the authors. Based on numerical simulation results, the maximum improvement I_{max} of minimum film thickness h_{min} and corresponding optimal dimensionless coating thickness H_2 are correlated to *M*, *L* and R_2 through multiple regressions. Two regressed formulas are reported

$$I_{max} = 0.766 M^{0.0248} R_2^{0.0296} L^{0.1379} \exp(-0.0245 \ln^2 L) \tag{80}$$

$$H_2 = 0.049 M^{0.4557} R_2^{-0.1722} L^{0.7611} \exp(-0.0504 \ln^2 M - 0.0921 \ln^2 L) \tag{81}$$

These formulas address two critical questions for engineers in the design of stiff coating in "hard" EHL applications, which are, the selection of the coating thickness and the improvement in surface performance. In order to obtain the maximum improvement in minimum film thickness indicated by I_{max}, the optimal coating thickness should be selected from H_2 with respect to the actual material system and working conditions, and how much improvement it will gain from the use of the coating.

6.2 Budget Period 2

Deliverables

7. Component surface design model and benefits evaluation
8. Optimized sump and reduced churning loss for axles & transmissions
9. Feasibility study for low friction materials and coatings for driveline components
10. Advanced wear model with surface evolution
11. The effect of lubricant rheology, boundary film properties, sump starvation, and severe conditions on friction
12. Models for improved gear design, bearing and seal design/selection
13. Friction, wear and pitting bench test results
14. Preliminary technology implementation strategy for axles and transmissions.
15. Improved design guidelines for lubricant selection

6.2.1 Component Surface Design

The surface pitting model required the use of three modeling modules:

a) One, to predict maximum contact stress location and its magnitude for actual surface topographies in contact
b) The second one, to compute residual stress level and distribution in the contact area due to localized surface displacement,
c) The third one, to compute pitting crack formation and growth, preferably capable of handling multiple cracks.

A simple model for prediction of the results of an elastic-perfectly plastic contact simulation was developed. The location and magnitude of the maximum stress was found to be a function of the size of the smallest significant asperity, material properties, and operating conditions. This model was used as a tool for quick estimates of the upper bound of the maximum stress distribution in rough surface contact. The model also was capable of determining the transition load, for a given set of tribological conditions, required to maintain the maximum shear stress in the sub-surface region for specific rough surface contact conditions. To obtain high durability, the stress level needs to be reasonably low and located below the surface. **Figure 6.2.1-1** shows the effect of combined surface roughness on the contact stress so as to maintain it under the surface.

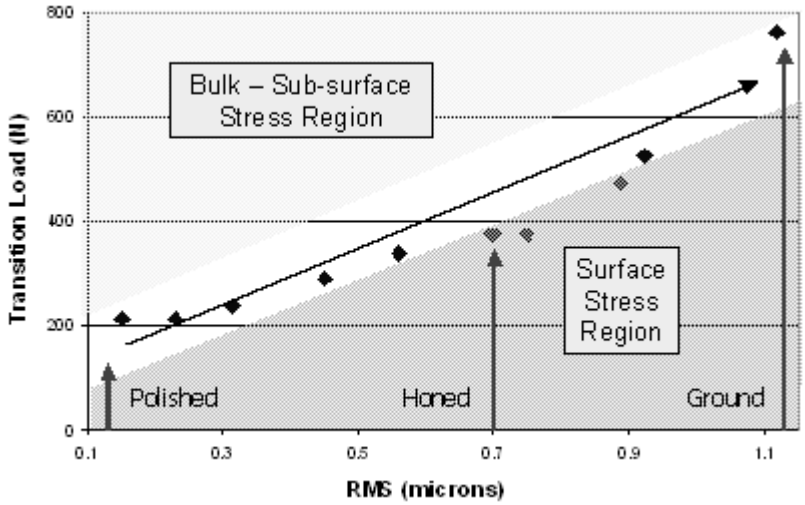

Figure 6.2.1-1: Output from model for predicting the results of elastic-perfectly plastic contact. Ground surfaces require high transition load to keep shear stress in the sub-surface region. Polished surface require a very low load, potentially improving durability.

A modified semi-analytical method to simulate contact mechanics (SAM) was developed to simulate 3D elastic-plastic contact with different hardening behavior. An additional code was developed to simulate normal indentation of a smooth sphere on a rough surface, incorporating materials with linear hardening behavior.

Three typical types of machined surfaces are utilized in the contact simulation cases: Polished surface, honed surface, and turned surface, see **Figure 6.2.1-2.**

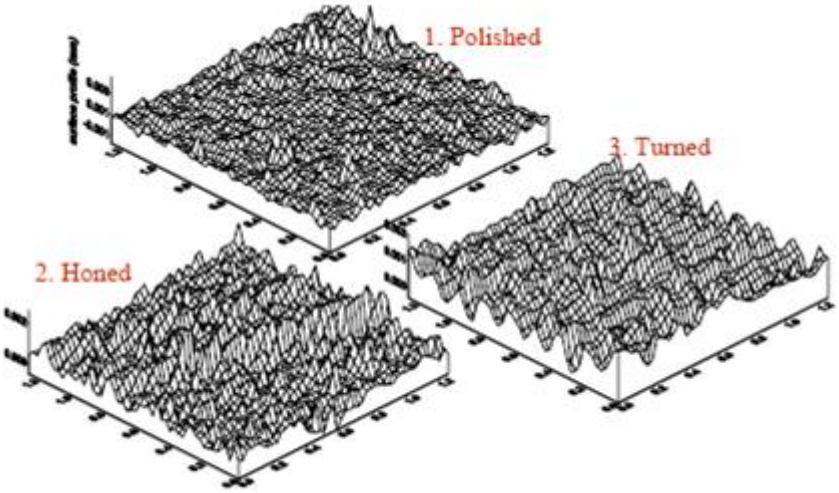

Figure 6.2.1-2: Typical types of rough surfaces

The pressure distribution obtained for a typical rough contact case is compared with the Hertz pressure, see **Figure 6.2.1-2.** It is found that rough contact pressure becomes irregular, and the maximum value is enlarged from 2 *GPa* to 5 *GPa*.

Figure 6.2.1-3: Comparison of 3D pressure distributions

The calculated results show that the complicated surface geometry leads to an irregular and often higher than smooth surface contact distribution of contact pressure and the greater surface roughness results in the more irregular pressure distribution, as shown in **Figure 6.2.1-4.**

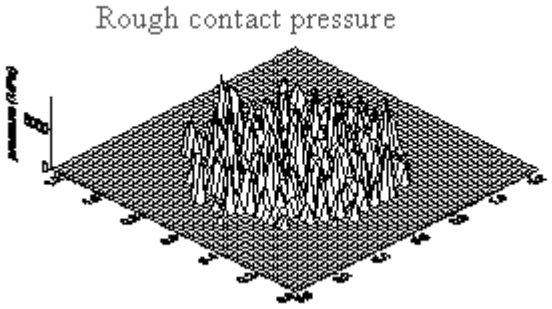

Figure 6.2.1-4: Irregular pressure distribution results from rough surface contact.

This rough surface contact, along with the irregular and localized high contact loads will lead to surface deformation and result in both surface hardening and creation of sub-surface residuals stresses, which can either retard or enhance pitting crack propagation. **Figure 6.2.1-5** shows such surface deformation (top) and resulting compressive residual stresses in the cross-section (bottom).

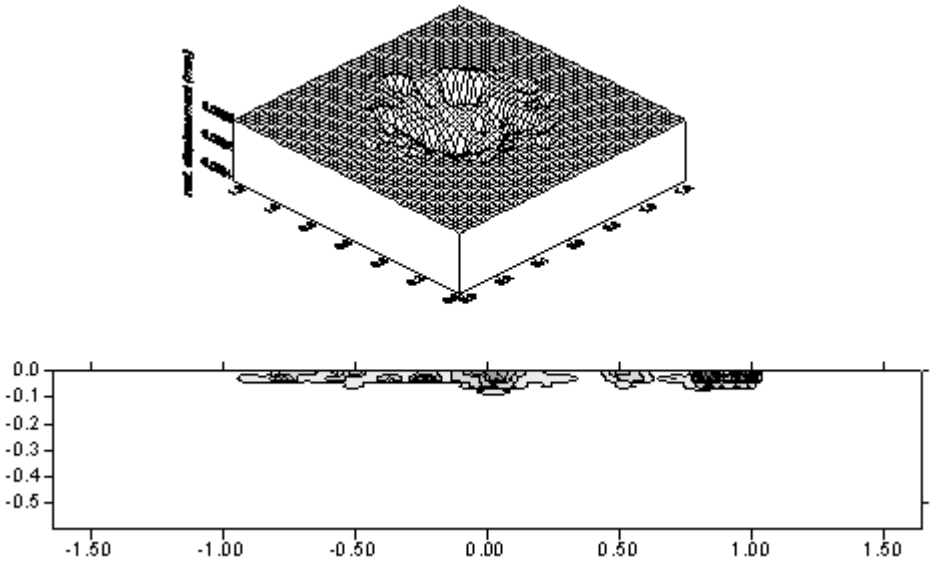

Figure 6.2.1-5: Irregular contact loads cause subsurface residual stresses.

Once the maximum stress location and magnitude is known, then the crack formation and growth needs to be predicted. An assessment has been made that the FATG3D, previously developed at Northwestern University, can yield an accurate analysis of intensity factors and it is capable of dealing with multiple cracks and their coalescence into larger cracks or one large crack. Therefore, it was used as a module in the integrated model. A revised Paris law was applied to predict crack growth under fatigue load. An example of coalescing cracks as a function of number of load/contact cycles is shown in **Figure 6.2.1-6.**

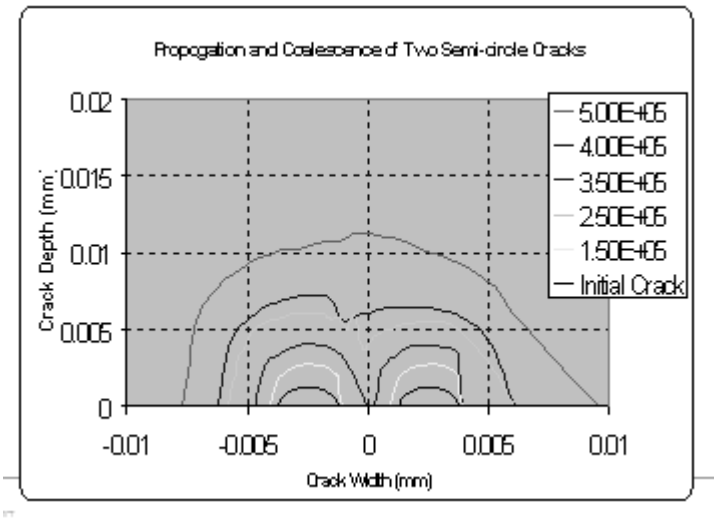

Figure 6.2.1-6: Prediction of crack propagation and coalescence for two semi-circular cracks.

6.2.2 Optimized Sump- A

Lubricant fill level on lubricant temperature was tested at both Eaton and Caterpillar to indirectly assess potential for minimizing parasitic losses due to lubricant churning, and thereby affect fuel economy. Test results from both companies indicated that reduced fill levels reduce oil temperatures, thereby offering potential additional efficiency improvements. **Figure 6.2.2-1** shows oil temperature under different levels of fill as a function of speed and torque for Caterpillar's the final drive axle.

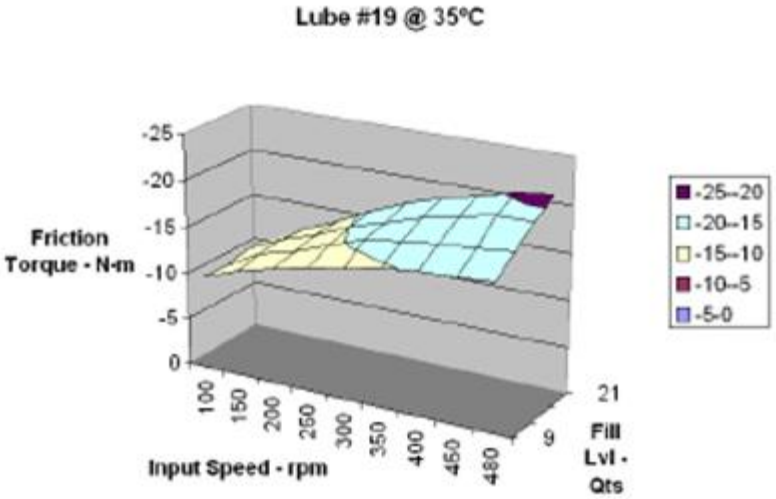

Figure 6.2.2-1: Effect of fill level on the churning torque as well as the lubricant temperatures

Figure 6.2.2-2 shows sump temperature versus power for two transmission oils at two fill levels.

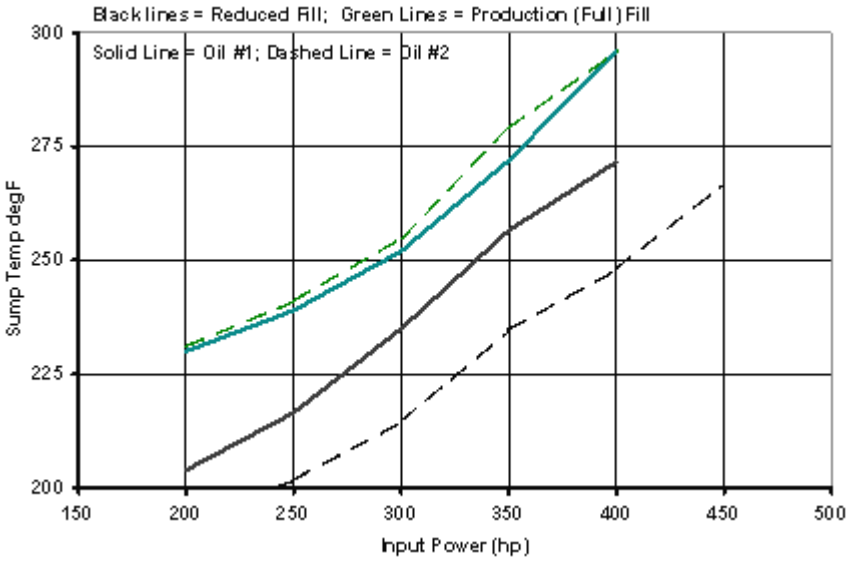

Figure 6.2.2-2: Low fill level reduce operating temperatures.

6.2.3 Low Friction Materials

Argonne previously developed near frictionless carbon (NFC) coatings with potential application to truck drivelines. These coatings appeared to be attractive for gearing applications as the substrate deposition temperature is approximately 150º C, with high hardness (1600 – 3000 Hv) and thickness up to 10 µm. The NFC coating was evaluated at Eaton for frictional characteristics under sliding motion. Another family of coatings considered was that of super hard nano-coatings, also studied at Argonne, but not directly under this project. One nano-coating from Argonne was tested at Eaton and compared against baseline uncoated as well as a commercially available tungsten carbide hard coating (3000 – 3500 Hv) from Hardide Coatings Ltd., UK. The testing was done using a standard test of *3 mailbox pins-on-ring* configuration with step-increase of load. **Figure 6.2.3-1** shows the test results.

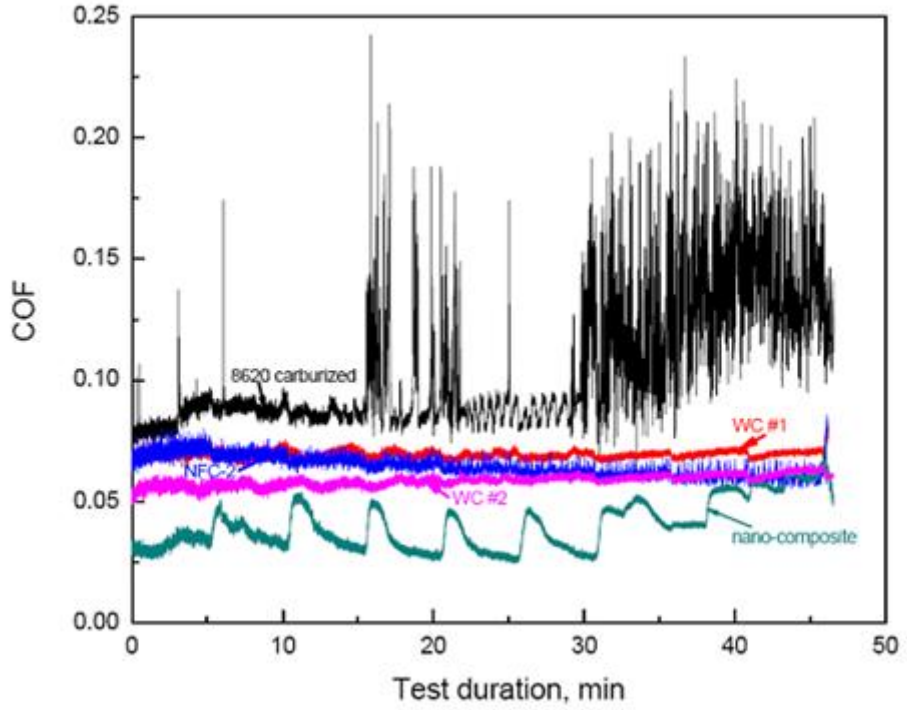

Figure 6.2.3-1: Pin-on-ring Falex test shows effectiveness of coatings.

The baseline steel showed not only higher friction level, but also exhibited highly undesirable friction instability as higher loads were imposed. All of the coatings showed lower friction than bare steel, with the Argonne NFC coating being comparable to the Hardide coating. The nano-coating, although on average showed lower friction, exhibited a relatively high friction as the load step was made and then stabilized over time during that load period. These results demonstrated that coatings can significantly reduce sliding friction and maintain it at a low level.

6.2.4 Wear Model

Wear model development is based on the rough surfaces contact model already developed with a modification that a wear coefficient is applied to the contacting asperities thereby gradually removing them. This wear model, developed at Eaton, was used to analyze several sample cases and the results make good sense physically showing good qualitative agreement with experimental observations. Key cases include using a mathematically describable model having the stationary surface with sinusoidal asperities in contact with mathematically smooth moving surface, and at least one real surface condition capable of being tested. The example below shows a development of a wear track as a function of time step equivalent to sliding distance, **Figure 6.2.4-1.**

Animations were developed to better illustrate the surface evolution, friction variation, contact pattern changes and accumulated wear, etc. The animated showed that friction is initially high due to asperity contacts in mixed lubrication. However, when sliding wear occurs, the friction goes down first due to asperity peak removal during the running-in, and then goes up gradually

due to the increase of contact area after running. This model is capable of simulation sliding wear with different operating conditions, materials, lubricants and boundary additives based on experimentally estimated wear coefficients and friction. Use of that model provided a better understanding during the break-in phase and subsequent stable wear phase, which impact both friction and durability. Lubricant test data from traction tests performed at Wedeven Associates enabled analysis of the break-in wear.

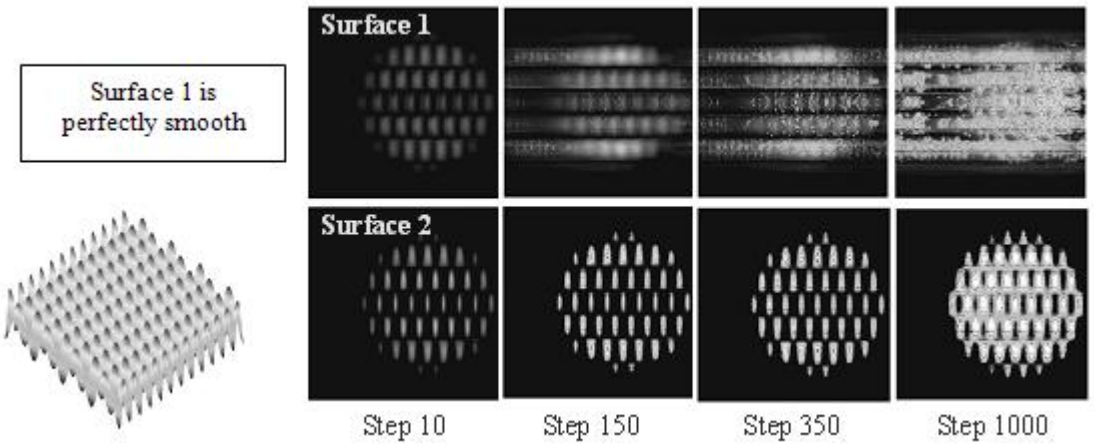

Figure 6.2.4-1: Results from the wear model show developing wear tracks as a function of time.

The lubricant effects on friction were studied utilizing a WAM machines at Wedeven Associates, Inc., an FZG tester at Caterpillar, a ball-on-disc friction tester at Argonne and a modified Falex 6 tester at Eaton. Eighteen axle lubricants and eight transmission lubricants were evaluated under different conditions of speed, load, and surface topographies. The assessment was that significant potential existed for friction reductions of 20 to 30 percent, depending on the lubricant and additives used. **Figure 6.2.4-2** shows the data with two potential fluids selected for future gear efficiency testing using modified FZG machine.

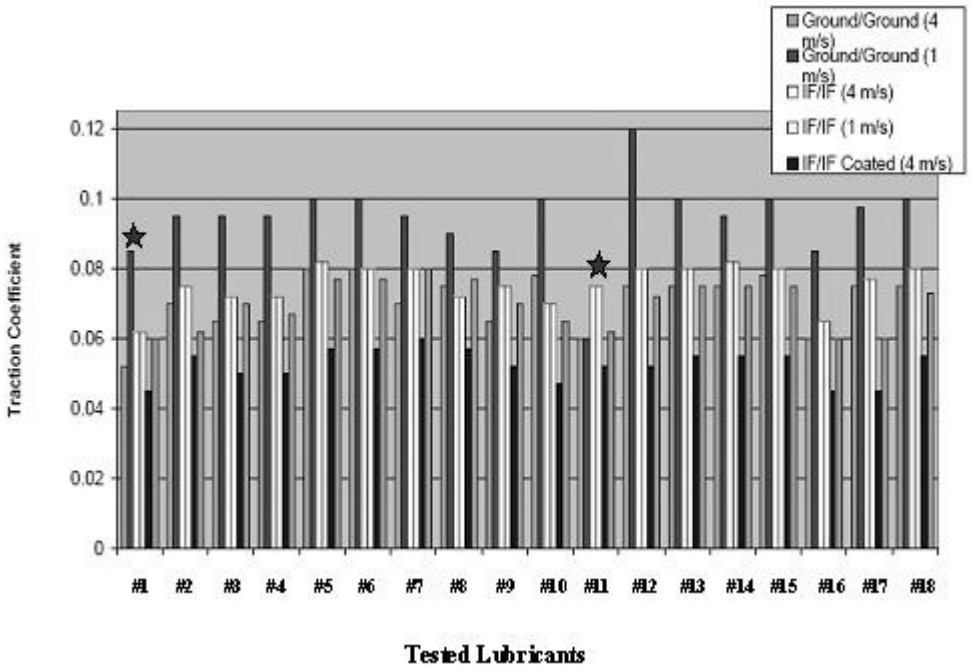

Figure 6.2.4-2: Lubricants and surface finishes for use on gears.

6.2.5 Lubricant Rheology

Argonne National Laboratory (ANL) evaluated the friction and wear performance of six oils provided by Caterpillar and Eaton. These tests were conducted for steel-on-steel sliding at lubricant temperatures up to 125 degrees C, **Figure 6.2.5-1.** Upon completion of the tests, a look-up table was prepared for the friction data, **Figure 6.2.5-2.**

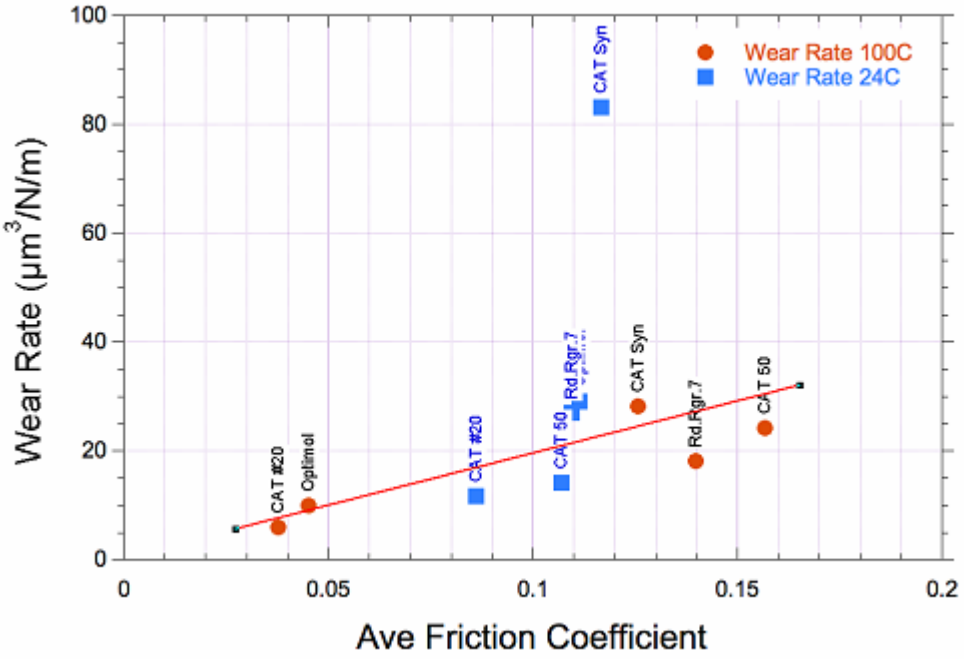

Figure 6.2.5-1: ANL-developed relationship between average friction and overall wear for steel on-steel sliding lubricant temperatures of room temperature and 100 degrees C.

	Optimol	Roadranger 7	CAT #20	Circle 3	CAT Syn	CAT 50
RT	0.11	0.111	>0.092	0.115	0.117	0.108
50°C	0.059					
70°C	0.043		0.052			
100°C	0.045	0.138	0.037	<0.122	0.126	0.153
125°C	0.033	0.099			0.105	0.118

Figure 6.2.5-2: ANL look-up table for friction coefficient after friction drop (if any) for 1 cm/sec sliding.

ANL summarized the friction test results in the following:

- All oils have high initial friction (0.12-0.15) coefficients
- Optimol exhibits a time-dependent friction drop at elevated temperatures, with higher temperatures being an advantage for both friction and wear
- CAT#20 exhibits the largest friction drop of all the oils, with higher temperatures being an advantage for both friction and wear

- Cat Syn 75W140 has steady friction coefficient that is not lower than ≈0.1 and highest wear rate
- CAT FDAO 50 produces higher friction coefficients at higher temperatures and fairly high wear
- Circle 3 has generally high friction (0.15) which decreases slightly during the test to about 0.12
- Roadranger 7 friction has steady friction behavior that is between 0.1 and 0.14 for all test temperatures Optimol exhibits a time-dependent friction drop at elevated temperatures, with higher temperatures being an advantage for both friction and wear
- CAT#20 exhibits the largest friction drop of all the oils, with higher temperatures being an advantage for both friction and wear
- Cat Syn 75W140 has steady friction coefficient that is not lower than ≈0.1 and highest wear rate
- CAT FDAO 50 produces higher friction coefficients at higher temperatures and fairly high wear
- Circle 3 has generally high friction (0.15) which decreases slightly during the test to about 0.12
- Roadranger 7 friction has steady friction behavior that is between 0.1 and 0.14 for all test temperatures

6.2.6 Bearing Design and Testing

A testing protocol was developed for the efficiency tests. The bearings were broken in as normal by ramping radial force from 1875lbf/bearing (25 percent of full load) to 7500lbf/bearing (100 percent of full load) linearly in five hours at full speed with the baseline oil #18. A second break-in period of the bearings (run at constant load and speed) was run for each oil tested to ensure an acceptably low rate of change in torque level for the test block. A reduced load of 4038lbf/bearing (54 percent of full load) was chosen for this break-in to reduce the chance of failure of the bearings over the course of testing. The load chosen still corresponds to the contact pressures seen in the bearings in differentials of medium sized wheel loaders.

The test matrix has been expanded from the original 10 points over 4 speeds and 4 loads to 23 data points taken over 4 speeds at 4 loads plus the no load (churning) condition. This was done to ensure all intermediate loading conditions were examined and to eliminate interpolation errors. Each data point was taken after four minutes of holding at constant load and speed to allow the torque to stabilize. The baseline oil was run at three separate times throughout the testing (1^{st}, 4^{th}, and 6^{th} oil tested) to check for any 'drift' in the measured torque at steady state and for consistency of the test matrix results. An additional break in period was added due to the observation that the measured torque under constant load and speed continued to drop. This break in period lasted for 90 hours until the rate of change in the measured torque dropped to approximately 0.01in-lbf/hr.

At high load, **Figure 6.2.6-1**, and low speed, a boundary lubrication condition is expected to dominate. In this regime the additive package should have maximum effect, and the results of

testing suggest that this is the case. A 29 percent drop in input torque was seen from baseline Oil #18 to Oil #11, a natural base stock oil with the additive package. The drop in input torque to the synthetic base stock oils was even more pronounced. Oil #20 is the prime low friction candidate for highly stressed gear contacts. The measured torque in this oil was 39 percent lower than in the baseline. Surprisingly, friction torque with Oil #1 was about 47 percent lower than the baseline Oil #18 at these conditions. One possible contributing effect which needs to be investigated is differences in viscosity. In the natural base stock oil the viscosity difference from the baseline was fairly low (<1cSt). In the synthetic base stock oils the viscosity differences were much greater.

Input torque variation between oils is much less pronounced as loading conditions become less severe. As speed is increased the input torque drops rapidly, and this effect itself becomes less apparent as the load is decreased and reverses under the lowest load and no load conditions. This can be seen most prominently in Oil #1 between the 100 percent and 50 percent loading conditions, **Figure 6.2.6-2**. At 100 percent load Oil #1 has an input torque minimum at 50 percent speed; at 50 percent load the minimum has moved to the lowest speed. This relationship of input torque to load and speed for each oil resembles the Stribeck type curve, which describes the likely conditions for boundary, mixed, and full film (either hydrodynamic or elastohydrodynamic) regimes. Boundary lubrication dominating in the high load/low speed conditions, and full film dominates in the low load/high speed conditions. Under no load conditions churning losses correlate with calculated viscosity of the oils as shown in **Figure 6.2.6-3**

Based on the testing results, it has been concluded that: a combination of synthetic base stock with the additive package (oil #20) results in a 39 percent drop in input torque at the most severe loading conditions when compared to the baseline Oil #18. This improvement decreases at higher speeds, but remains 11 percent lower even at the highest speeds tested. The difference also decreases as the load decreases, but the no load results suggest that this may be simply be due to the higher viscosity of Oil #20 at temperature.

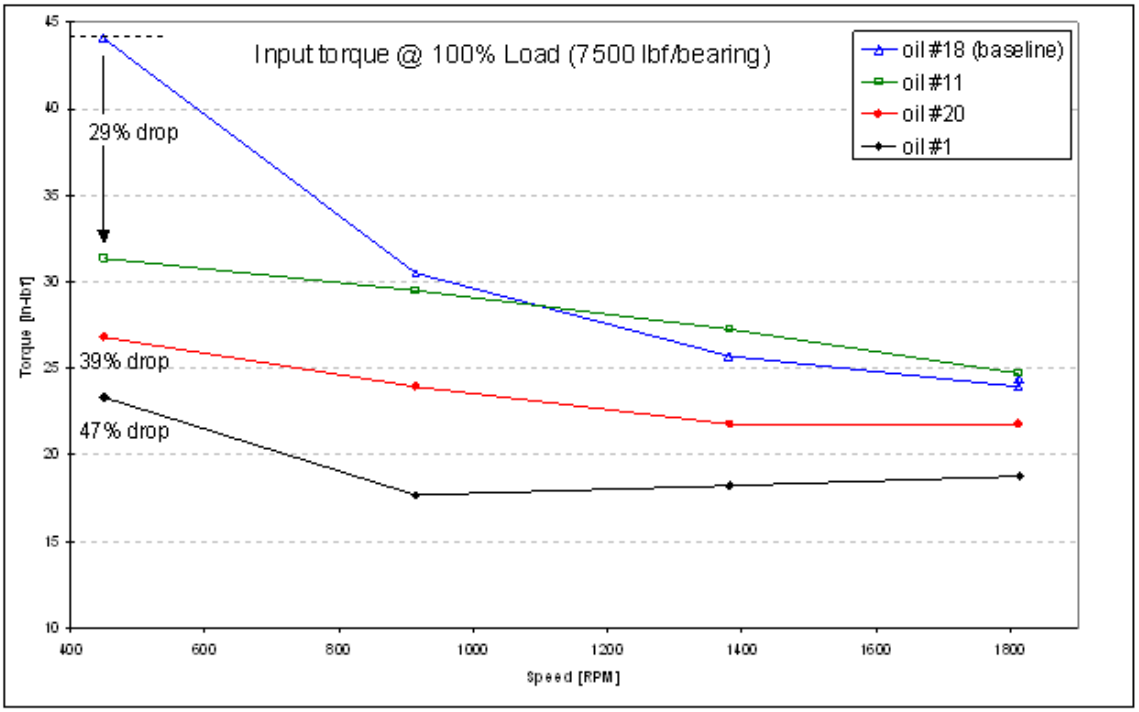

Figure 6.2.6-1: **Graph of measured input torque at 100 percent loading and various speeds. Friction torque at low speed with Oil #1 was 47 percent lower than the baseline Oil #18.**

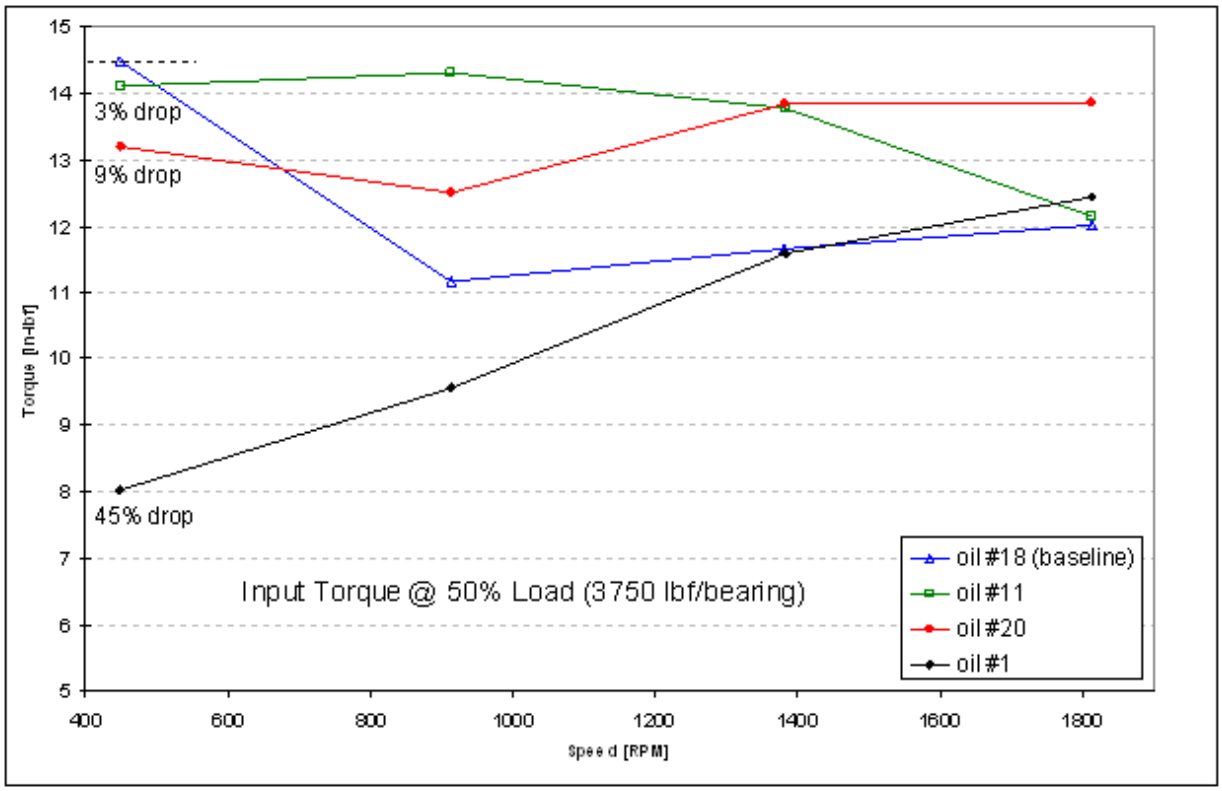

Figure 6.2.6-2: Measured input torque at 50 percent loading and various speeds. Friction torque with Oil #1 is 45 percent lower than the baseline Oil #18.

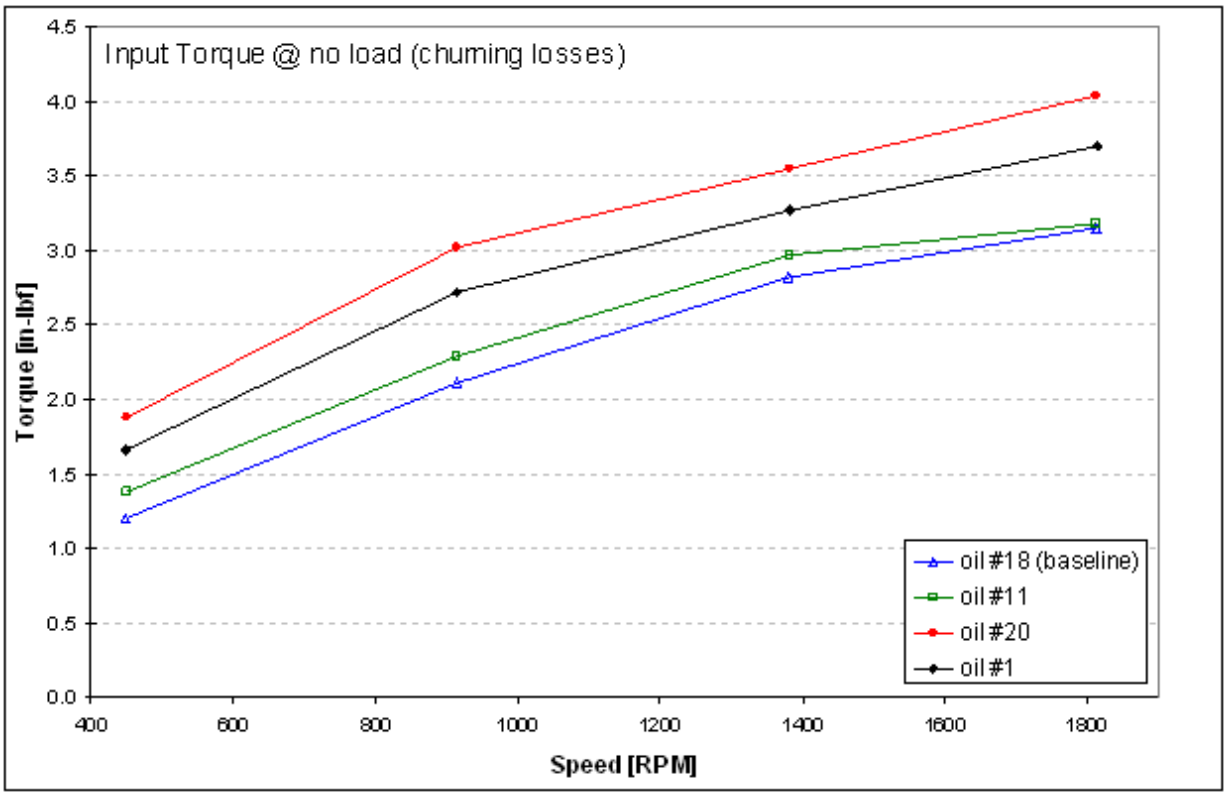

Figure 6.2.6-3: Measured input torque at no load across various speeds. Under no load conditions churning losses correlate with calculated viscosity of the oils.

Bearing Friction Torque Testing

New equipment was designed and manufactured to more accurately measure bearing endplay, **Figure 6.2.6-4.** This was done to ensure correct assembly of the bearing test block and to minimize variation in bearing endplay, therefore to avoid spallation of inner and outer races occurred during the test run for the procedure development. Development and validation of procedures using this tooling were completed.

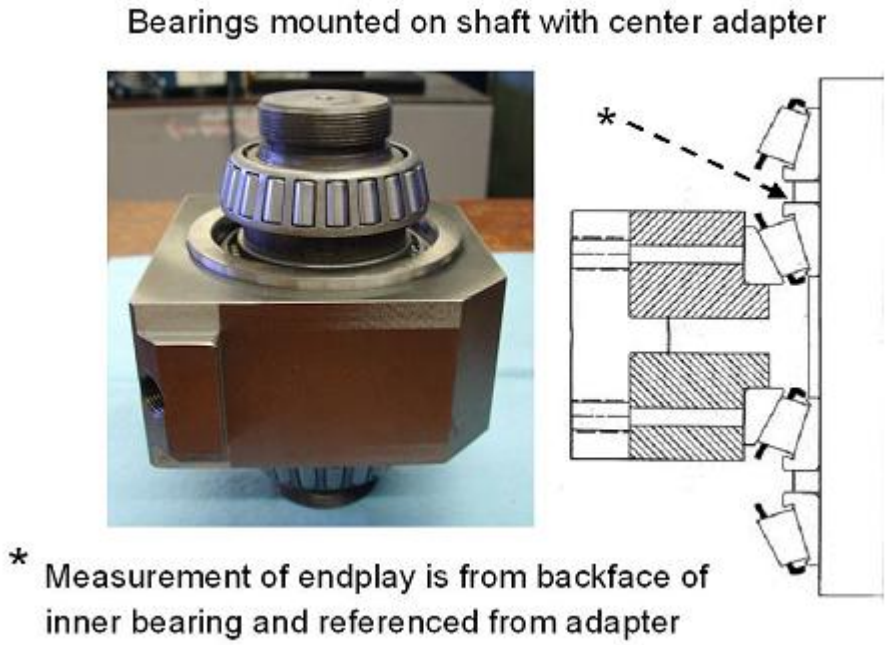

Figure 6.2.6-4: Caterpillar's new device for accurately measuring bearing endplay

6.2.7 Bench Top and Fixture Testing of Coupons

Eaton's Cemecon PVD (physical vapor deposition) system was used to deposit Diamond-Like Carbon (DLC) and other coatings on gears and Falex rings. Prior to the coating, the samples were prepared with 2 to 4 micro-inch super finish. **Figure 6.2.7-1** shows a representative PVD coated gear along with PVD coated roller contact fatigue samples and a PVD coated Falex ring.

These samples were used in various bench top tests to evaluate the performance of the PVD coating in reducing torque and friction while increasing durability. Specifically the objective of this work is to develop a low friction gear coating that reduces friction while retaining sufficient durability to survive 750,000 miles service in a heavy duty truck transmission.

Results from an Eaton Falex 3 ball-on-ring test using PVD coated rings appear in **Figure 6.2.7-2**. Three fixed, bare, SAE 52100 steel balls are run against PVD-coated, SAE 8620 carburized steel rings. All 3 ball tests are run with circulated Eaton Roadranger SAE 50 Revision 7 (Rev 7) lubricant held at 250 degrees F. The axial force is set at 120 lbf generating an initial contact stress of 322,000 psi (2.22 GPa). Speed is stepped upward from 100 rpm to 3,000 rpm.

Figure 6.2.7-1: Eaton spur gear, contact fatigue rollers and Falex ring that have been coated with Diamond-Like Carbon by physical vapor deposition.

The baseline is a bare SAE 8620 carburized steel ring. **Figure 6.2.7-2** clearly shows the benefit of running PVD coatings. At the upper left of the figure, torque data for the baseline sample, SAE 8620 steel, can be seen ranging from over 14 inch-pounds (in-lbs) down to 9.0 in-lbs. The baseline sample failed catastrophically at about 1 hour and 40 minutes into the test, corresponding to a speed of about 1100 rpm. In comparison the Diamond-Like Carbon (DLC) coating sample DLC1 completed the test producing considerably lower torque (friction) that ranged from 10.0 in-lbs to 3.75 in-lbs. Similarly the DLC2 coating completed the test and exhibited torque from 9.0 in-lbs to 3.0 in-lbs. In fact the bundle of the PVD coatings tested produced substantially lower torque than the baseline carburized steel. These 3 ball-on-ring tests indicate that the DLC coatings *reduce torque (friction) from 25 to 50 percent or more*, depending on the test conditions.

The PVD coatings not only reduce torque and friction, but they also reduce wear. Photographs of the wear scars for Balls 1, 2 and 3 for the baseline, bare SAE 8620 carburized steel sample and for the DLC2 sample are compared in **Figure 6.2.7-3**. Balls at the top, run against bare SAE 8620 carburized steel, exhibit large diameter wear scars with deep grooves. Balls run against DLC2, middle and lower rows, show smaller diameter wear scars and shallow grooves. The data is impressive in that *the DLC2 coating reduced wear by 80 percent.*

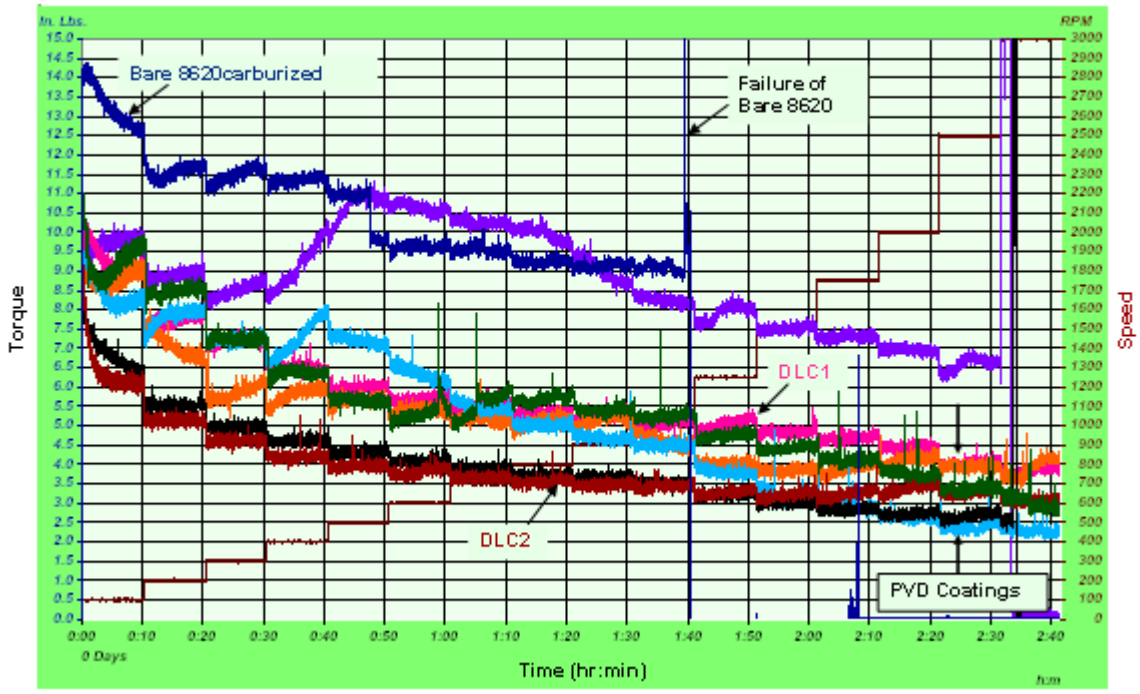

Figure 6.2.7-2: Torque curves for various PVD Diamond-Like Carbon (DLC) coatings compared to bare, SAE 8620 carburized gear steel Falex tested in Eaton Roadranger SAE 50 Rev 7 lubricant. The DLC coatings effectively reduce torque and friction.

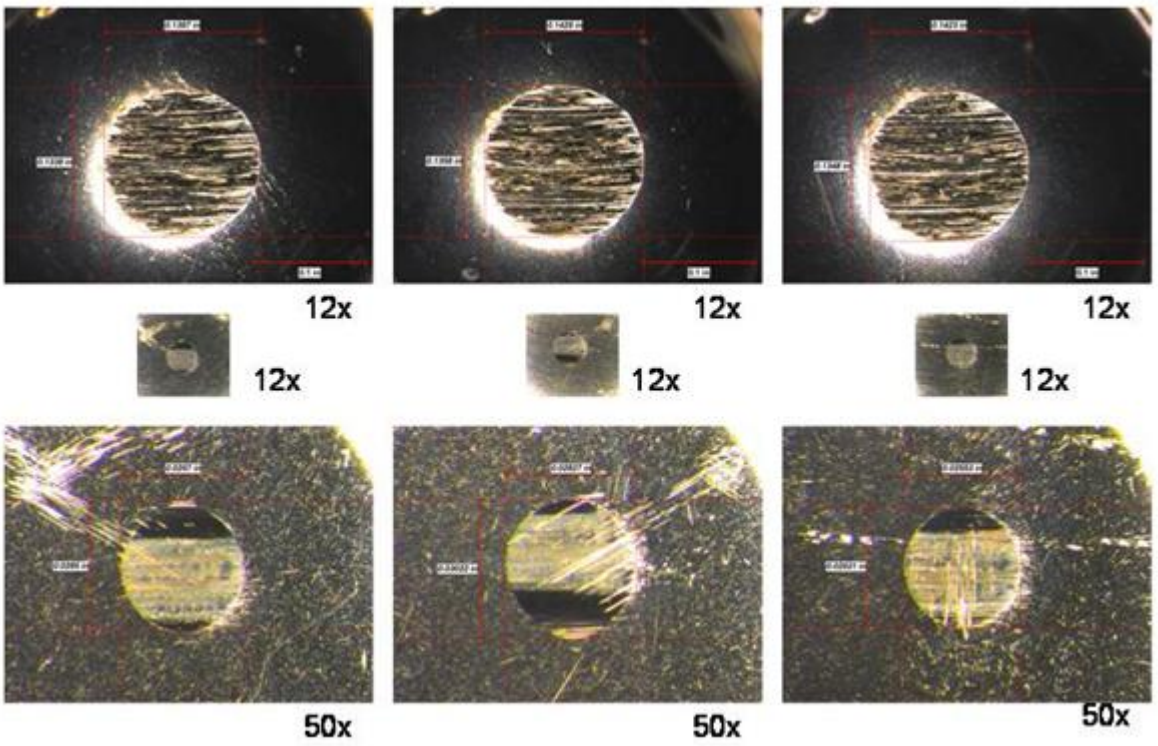

Figure 6.2.7-3: Wear scars on 3 SAE 52100 steel balls run against a bare SAE 8620 carburized gear steel ring (top row) are shown at 12x. Wear scars on balls run against a DLC2 coated ring (middle and bottom rows) exhibit 80 percent less wear.

6.2.8 Implementation Strategy

A strategy for implementing efficiency improvements on heavy duty truck transmissions and axles has been formulated. The strategy identifies specific technical factors that can reduce friction and parasitic losses and, in turn, that can be exploited to reduce the US consumption of petroleum by trucks. Among the technical factors are the following:

1. Lubrication
2. Churning
3. Surface roughness
4. Coatings
5. Textures

The order in which the factors are presented, implying their relative importance, may be the subject of debate, but the items on the list remain firm. Previous work under this program identified a realistic target for fuel economy gains from the reduction of friction and parasitic losses in driveline components. The target is two to four percent more miles per gallons. Attainment of this goal requires reducing friction and parasitic losses in the driveline by thirty to fifty percent.

It should be remembered that the implementation strategy was formulated for heavy duty trucks. However, the approaches described also have applicability to light duty vehicles and to passenger vehicles.

6.2.9 Lubricant Selection Guidelines

1. Use a synthetic base oil like a PAO
2. Use low viscosity oils
3. Use oils containing dissolved, solid lubricant-forming compounds like organo-Molybdenum
4. Suspend small particle (0.5 micrometers)solid lubricants in the oil
5. Reinstate well established anti-wear agents like ZDDP

6.3 Budget Period 3

Deliverables

16. Commercialization potential of low friction materials and coatings
17. Failure criteria for driveline component design
18. Integrated design procedure to reduce friction in gears, seals and bearings
19 Friction, wear, and pitting bench test results

(8)-B Optimized sump and reduced churning loss for axles

6.3.1 Low Friction Materials and Coatings

Eaton continued to examine PVD (physical vapor deposition) coatings for use on gears. Eaton supplemented the bench top Falex test data with data from the roller contact fatigue tester. This fixture utilized larger samples more representative of transmission gears. In the roller contact fatigue test (RCFT) a 2.33-inch diameter roller with a 0.0002-inch diameter crown ran against a flat, 3.6 inch diameter roller. The load on the samples was 3,000 pounds force (lbf) producing a contact stress exceeding 300,000 psi, a typical value for gear contact stress. The base material was SAE 8620 carburized steel. Prior to these RCFT all samples were super-finished to a surface roughness of 2 to 4 microinches. During the test the rollers were lubricated with Eaton Roadranger Revision 7 transmission fluid. As an initial test criterion, the test was scheduled to run 100 hours at 3,000 rpm. Every 24 hours the test was halted and the rollers were inspected.

Eaton subjected a baseline sample and two PVD coatings to roller contact fatigue testing. A base line set of rollers and two PVD coatings, Diamond Like Carbon (DLC) and Tungsten Carbide-Carbon (WC-C), were tested:. The SAE 8620 carburized steel baseline sample completed 96 hours test time before the onset of pitting. In comparison the PVD DLC coated rollers lasted only 48 hours of test time before the coating stripped off, **Figure 6.3.1-1.** Similarly the PVD WC-C survived only 24 hours of run time at 3,000 rpm. The short lives of the PVD coatings were not a favorable outcome and surprised Eaton engineers. Subsequent analysis of the roller revealed an abrupt step in the crown of the small rollers. The step apparently increased the

contact stress beyond the capability of the PVD coatings. New rollers with proper crowns were prepared and the test was scheduled to be repeated.

Figure 6.3.1-1: Because of improper machining, the PVD coating on these rollers was stripped off in 48 hours.

Twelve new sets of large and small rollers were machined and inspected. Surfaces roughness from machining varied from 4 to 10 microinches. This surface roughness is slightly high for PVD coatings. Ten of the twelve sets were sent out for super finishing to a surface roughness of 2 to 4 microinches. After super finishing, these roller sets were PVD coated and tested.

Solid Lubricants

The "-sl" suffix of the AlMgB-TiB coating designates the use of a solid lubricant within the coating. Solid lubricants reduce friction and parasitic torque. In this case the solid lubricant is co-deposited (deposited simultaneously) with the AlMgB-TiB hard coating. This is a unique approach to maintain the presence of a solid lubricant at a very high contact stress. Other solid lubricant approaches have been used in the past with varying degrees of success. Lowest tolerance for high contact stress is demonstrated by resin (polymer) bonded solid lubricants. These coatings perform superbly in low contact stress applications. However, at the high contact stress encountered in transmissions and axles, these coatings provide low friction at the beginning of gear tests but soon disappear after a short run time.

Frustrated with the short life of resin bonded solid lubricant coatings at high contact stress, engineers turned to adding solid lubricant to the lubricant. This is a technically sound approach but success depends on getting solid lubricant particles or dissolved compounds to create a beneficial film at the contact interface. Usually the protective barrier forms only under the right combination of temperature and pressure. Also the real estate of the gear tooth surface must be available and not encumbered with a myriad of other compounds trying to provide wear resistance and oxidation resistance films. Part of the challenge with lubricant-borne solid lubricants is to break down the cohabitating films from lubricant additives so that the solid lubricant films can form. The desirable combination of temperature and pressure for forming solid lubricant film also seems ephemeral, occurring for precious minutes during long hours of run time.

These challenges reinforce the beauty of adding solid lubricant within the PVD hard coating. There is no reliance on a low strength polymer to keep the solid lubricant at the contact interface. There is no need for ideal conditions of temperature and pressure to establish the beneficial film, and there is no chemical fight over clean steel, gear tooth real estate. PVD "-sl" hard coatings position solid lubricants precisely at the contact interface. The rigid PVD coating maintains its integrity preventing the solid lubricant from being pushed away, even at high contact stress.

6.3.2 Failure Criteria for Driveline Components

General

Throughout geared products, the predominant failure mode of concern is pitting. Gear tooth fatigue failure is the secondary failure mode. Pitting is described by numerous names determined by severity of the discontinuity. Frosting and micro-pitting denote the onset of pitting. Spalling, thermal fatigue cracking and pitting are the terms associated with the most severe damage. The various degrees of pitting are produced by high contact stress from the roll-sliding contact of the teeth in mesh. High stress exceeding 350 ksi and high sliding cause pitting. Material strength, hardness and toughness are primary factors determining pitting resistance. Good lubricants can influence pitting by preventing metal-to-metal contact, reducing friction, providing anti-wear compounds and reducing interface temperatures.

Gear tooth fatigue failure often initiates subsurface. The initiation site most often is associated with the presence of subsurface inclusions or with the depth of the carburized and hardened case for carburized steels. Reducing the size and number of inclusions in the steel base metal improves the fatigue strength dramatically. Good carburizing and heat treating practices that minimize decarburization and minimize grain boundary oxidation improve fatigue strength. Increasing tip relief on the involute profile also can provide higher fatigue strength.

Pitting is a mode of fatigue failure of gear surfaces; it causes high friction, vibration and noise. Pitting life prediction, therefore, is vital to design and performance and reliability improvements. Conventional prediction methods, commonly found in industrial standards, are based on the Hertzian contact theory under the assumptions that surfaces are ideally smooth with no lubrication. Today, the trend of high power density, high reliability compact design requires the life prediction to consider severe operation conditions in mixed lubrication and the effect of surface roughness and topography. Also, it has been well known that ductile material failures in concentrated contacts are *better correlated with the subsurface von Mises stress, rather than the normal Hertzian pressure*. The present study aims to develop a pitting life prediction approach for line-contact components based on a 3-D line contact mixed elastohydrodynamic lubrication (EHL) model recently developed, which is capable of simulating the entire transition from full-film and mixed EHL down to dry contact of real machined rough surfaces under severe operating conditions.

Overall Approach:

a. Mixed lubrication analysis based on the model by Ren, Wang, and Zhu

b. Fatigue life analysis based on the model developed by Zaretsky and extended by Epstain et al.

Accomplishments:

- A pitting life prediction approach for gears, roller bearings and some other line-contact components is obtained based on the newly developed 3-D line-contact mixed-EHL analyses and subsurface von Mises stress calculation using digitized 3-D machined surface topography as input data.
- Fifteen transmission gear sets have been analyzed and life prediction results compared with available testing data. With adjusted materials parameters in the life model, predicted pitting life results agree well with available experiments. Gear tooth surface finish appears to have a significant influence on the pitting life, and the effect of surface topography should be sufficiently estimated in fatigue life prediction.

6.3.3 Integrated Design Procedure

Integrated Design Methodology

The strategy of model integration was defined to integrate the modules developed through this program. The flowcharts for gear design and metal face seal design were developed to lay out the module definition and the link between modules for advanced design in consideration of surface performance optimization for efficiency improvement and interface failure prevention.

Representatives from Eaton, Caterpillar and Northwestern formulated a roadmap for the combined modeling efforts. A collaboration strategy was summarized. The integrated gear design flowchart is illustrated in **Figure 6.3.3-1.**

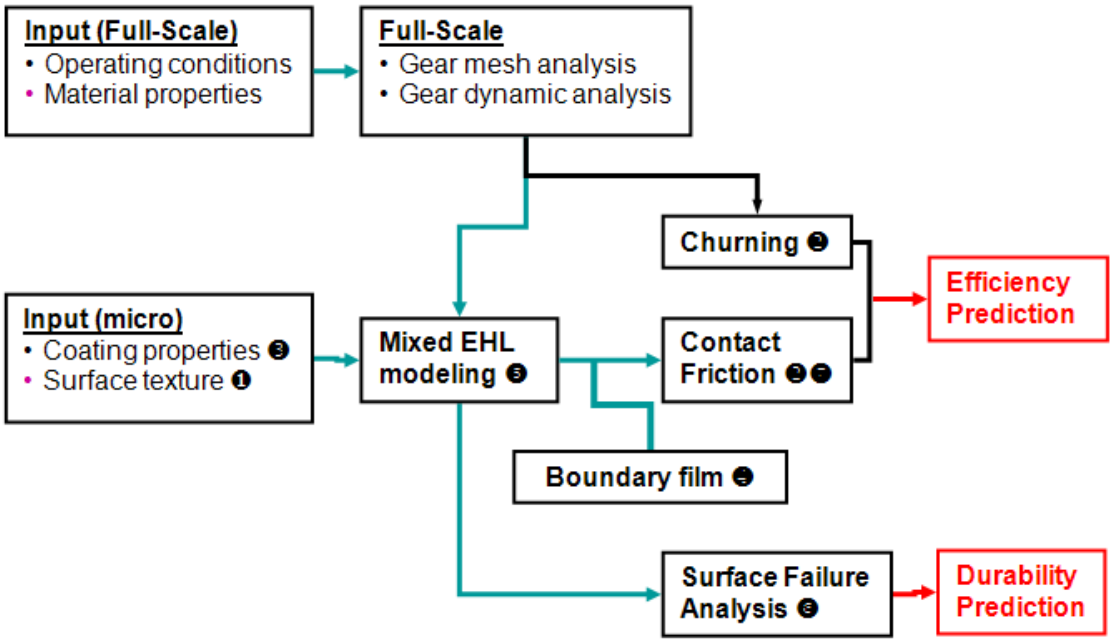

Figure 6.3.3-1: Integrated design methodology flowchart.

In the flowchart, the tasks under Project are represented by the number and listed here:

❶ Optimized surface design & manufacturing processes
❷ Lubrication, additives & churning control
❸ Low friction materials & coatings
❹ Boundary film behavior & prediction
❺ Mixed lubrication modeling
❻ Surface failure analysis & prediction
❼ Friction reduction in gears

The technology developed with each task was integrated into this advanced design model to consider the effects of manufacturing, lubricant, surface texturing and coatings with an improved performance prediction. The integrated model was to become a multi-scale design tool, which covers full-scale design concerning operating conditions and gear mesh/dynamic analysis, as well as improved models at micro-scale dealing with surface texture and coating issues. Gear efficiency and durability will be predicted and the benefit of technology implementation will be demonstrated.

6.3.4 Bench Top and Fixture Test Results

Lubricants

An implementation of the lubricant strategy materialized in August 2006 with the commercial introduction of a new Eaton transmission fluid, SAE 50 Revision 7 (Rev 7). The commercial release of this resulted in a 1 percent improvement in fuel economy for user fleets. Further gains over commercial lubricants can be made with functionally formulated oils and additives.

Figure 6.3.4-1 presents results from Falex four-ball testing of Roadranger Revision 7 lubricant along with another commercially available product Mobil SHC 50. Two friction coefficients are shown for Mobil SHC 50, 0.119 and 0.123. Under similar test conditions Roadranger Revision 7 oil yields a friction coefficient of 0.066. The reduction in friction coefficient, one commercial transmission fluid compared to another, *exceeds 40 percent*. While the reduction in friction is significant, this gain in efficiency would be an empty improvement if it was accompanied by increased wear. Fortunately, Roadranger Revision 7 reduces friction and produces a *corresponding 30 percent decrease in wear* compared to Mobil SHC 50. Similar improvements are shown in **Figure 6.3.4-2.**

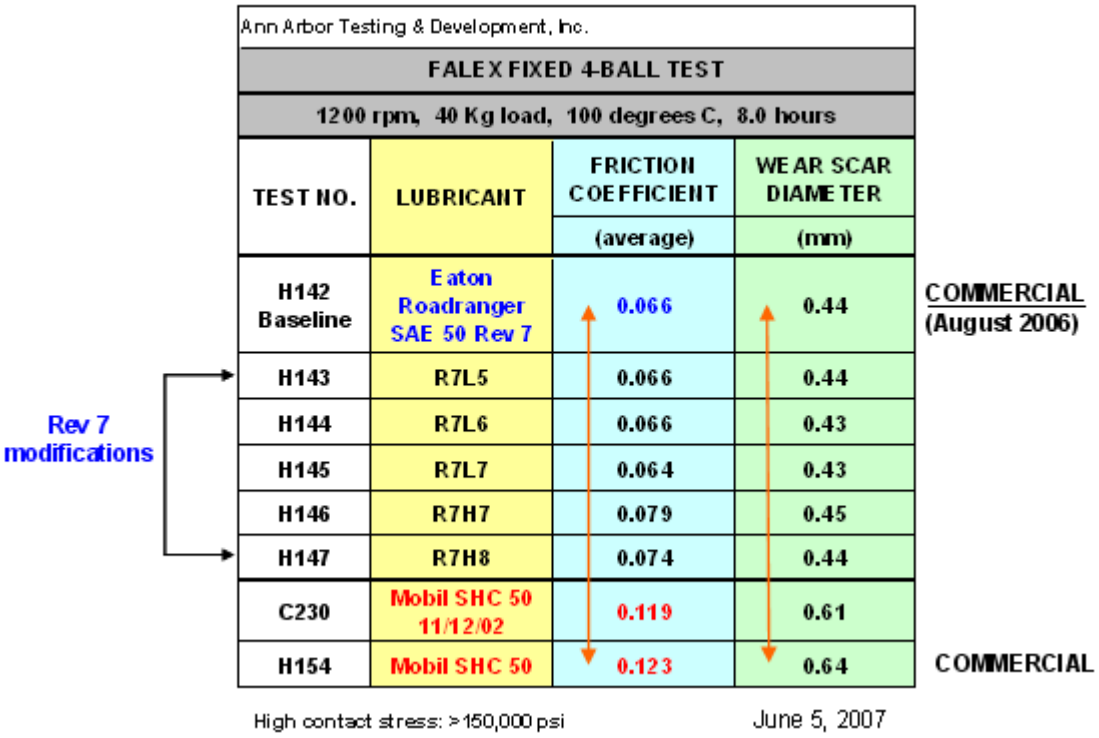

Figure 6.3.4-1: Falex four-ball test results for commercial and experimental oils.

TEST NUMBER	DESIGN CODE	LUBRICANT COMPOSITION	FRICTION COEFFICIENT	WEAR SCAR DIAMETER (mm)
H142	RFN4	Roadranger SAE 50 Rev 7 Baseline	0.066	0.44
H154	RFN4	Mobil SHC 50 tested 5/25/07	0.123	0.64
H204	RFY4	PAO + CK3D + RFF2 + RFY2 + H121	-42% 0.038	0.33 -25%

Figure 6.3.4-2: Falex four ball test data. Note the reduced friction coefficient and reduced wear of RFY4 oil compared to the already low values of Eaton Roadranger Revision 7 lubricant.

Eaton investigated two paths for reducing the friction coefficient in transmission fluid. The first path relied on modifications to the existing Roadranger Revision 7 lubricant, with the resulting fluid representing a hybrid Revision 7 lubricant. Hybrid Revision 7 lubricant was modified with an additive package designated RJK5. **Figure 6.3.4-3** compares Roadranger Revision 7 lubricant to the hybrid Revision 7 oil that contains the new RJK5 additive. Running Revision 7 oil with blended RJK5 additive reduced torque by 30 percent. The RJK5 additive (1) can be blended gradually into the oil before a test or (2) the additive can be injected rapidly, "dosed", into Revision 7 oil while a test is running. **Figure 6.3.4-4** compares torque results for the RJK5 additive blended into Revision 7 oil versus dosing the additive into the Revision 7 oil. The blended additive and the dosed additive tests show torque reductions of 25 and 24 percent. It is interesting that there is no apparent difference between blending the additive into Revision 7 oil before the test versus dosing the additive into Revision 7 oil during the test.

The capability of injecting an additive into a lubricated system and realizing a near-instant effect is very significant. Under conditions of high loading, high torque and high temperature, a special additive containing low friction and anti-wear compounds could be injected, provided extra protection for highly stressed components.

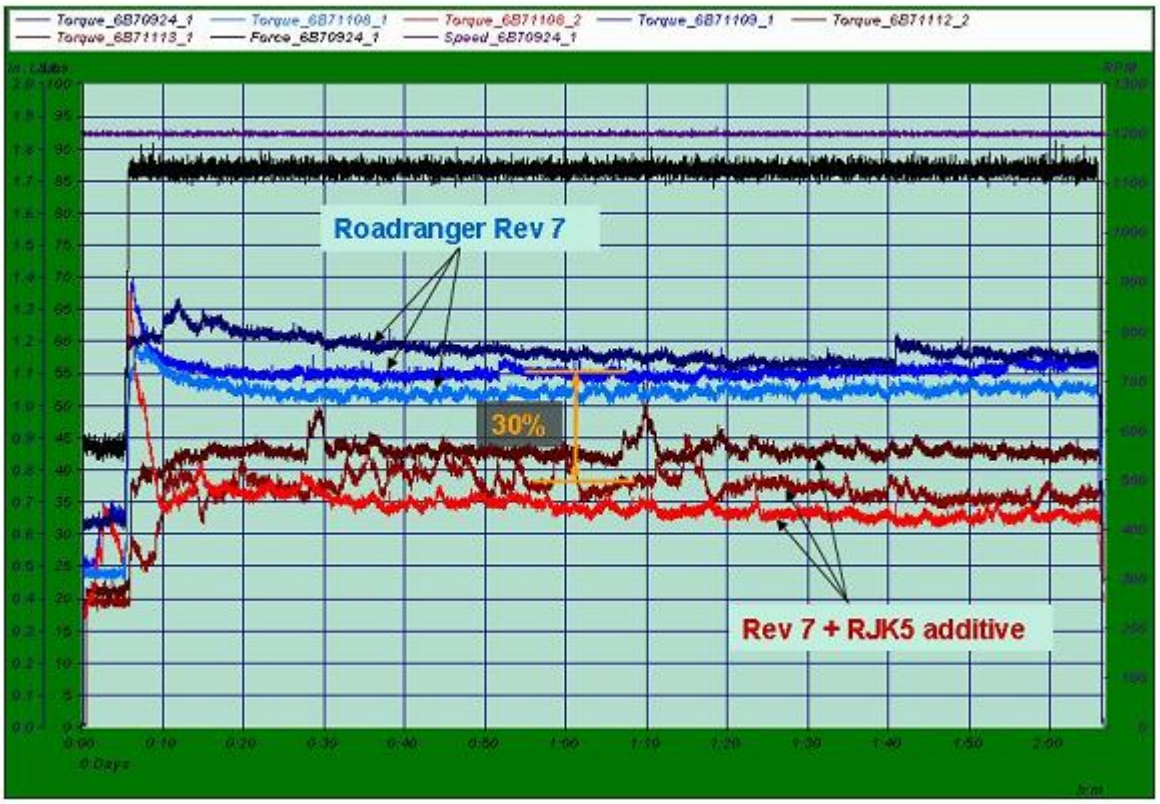

Figure 6.3.4-3: Roadranger Revision 7 lubricant compared to hybrid Revision 7 oil containing the new RJK5 additive. The blended additive reduces torque by 30 percent.

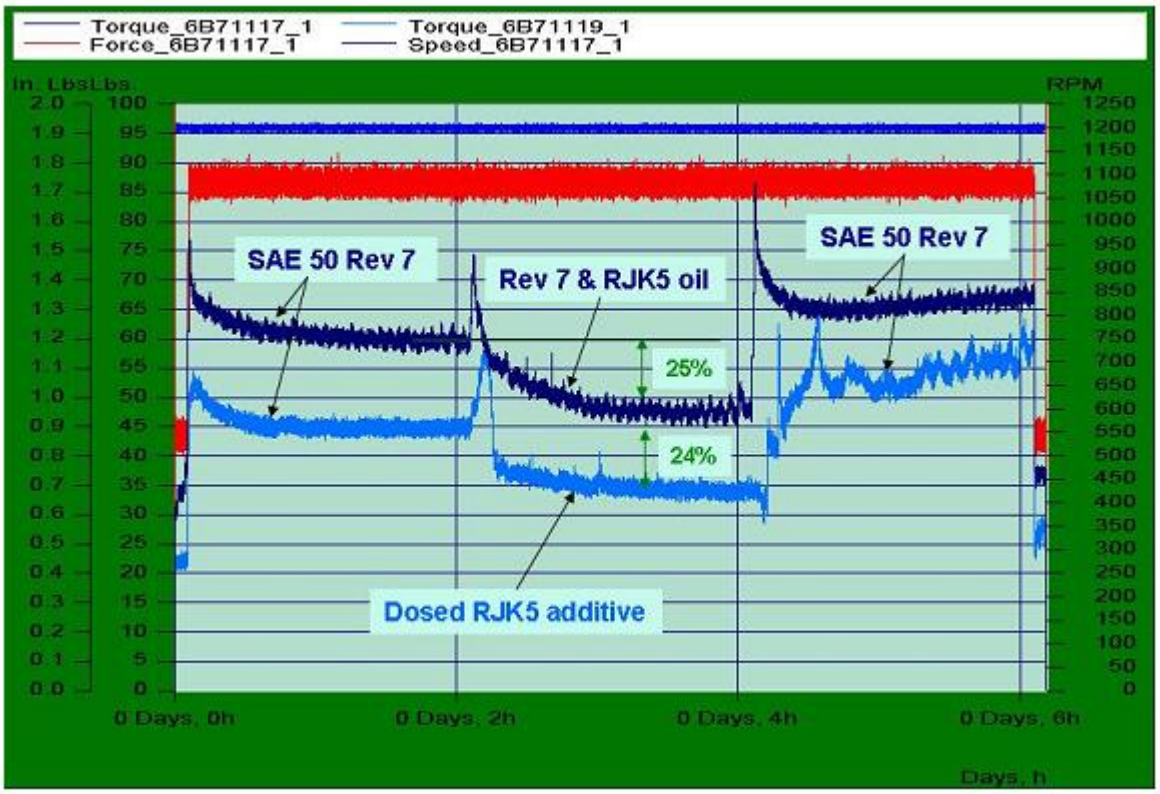

Figure 6.3.4-4: Varied-oil, Falex four ball tests results comparing Revision 7 oil and the new hybrid Revision 7 oil with the RJK5 additive. For the upper, dark blue curve, the central 2-hours of the test ran with RJK5 additive blended into the Revision 7 oil before testing. For the lower, light blue curve, RJK5 additive was dosed into Revision 7 after slightly more than 2-hours test time.

6.3.5 Optimized sump and reduced churning loss for axles and transmissions- B

Eaton engineers began compiling a history of dry sump tests that were run but did not result in a production dry sump transmission. The feasibility of producing an Eaton transmission incorporating a dry sump had been discussed repeatedly. A dry sump generally is known to reduce churning and thereby to reduce lubricant temperature. Because of the lower oil temperature, Eaton Truck engineers postulated that the dry sump would enable a cost-out by eliminating the need for transmission oil cooler. This small water-oil heat exchanger normally is mounted low on the transmission and has delivery and return lines running to the engine radiator. Heat load from the transmission can influence the duty cycle of the engine cooling system causing the cooling fan to run more often. A running fan typically pulls 84 horsepower (hp) from the engine.

While a number of previous tests had proven the feasibility of using a dry sump on a production transmission, the risk still has seemed too high. The potential for gear and bearing damage due to insufficient lubrication is the issue. To minimize churning and to prevent component damage, oil must be delivered precisely to the frictional contact interfaces. Auxiliary spray tubes and

lubricant injectors (some are electronic) are the key to the successful implementation of a dry sump.

Eaton Truck began pursuing this cost-out, eliminating the oil cooler, in Year 2002. Six cooperative truck fleets, well established Eaton Customers, were provided Eaton dry sump transmissions. A total of 20 dry sump transmissions were tested. The fleet applications ranged from an 80,000 pounds (lb) GCW (gross combined weight for tractor and loaded trailer) over-the-road bulk hauler to a 137,000 lb GCW on/off highway carrier. Sump temperature data from the dry sump fleet tests was accumulated from February 2002 through March 2005. Eliminating the oil cooler was the primary motivation for these tests; efficiency improvements were not considered initially. At the conclusion of the test none of the vehicles has sustained gear or bearing damage.

One specific incident stands out. Eaton requested that the fleets return the dry sump transmissions for post-test analysis; one fleet refused. When questioned regarding their refusal, the fleet replied that they were keeping the non-standard, dry sump transmissions due to improvement in fuel economy. The experimental transmission gave them 0.3 more miles per gallon, a 5 percent improvement based on the average of 6 miles per gallon. This fleet reported no specific issues with gear or bearing failures throughout the test period.

While reduced oil churning in the transmission was the major factor in obtaining this gain in efficiency, the improvement associated with eliminating the transmission heat load to the engine radiator must not be overlooked. The duty cycle of the cooling fan was lowered, in turn reducing the number of times the fan consumed 84 hp from the engine.

To show the impact of churning, Eaton engineers ran dynamometer tests on a conventional transmission and on a similar transmission incorporating a reduced fill, dry sump. For the overdrive gear ratio, under “no load” conditions, the dry sump reduced the parasitic torque by 31 percent, see **Figure 6.3.5-1.** With a direct, 1:1 gear ratio, the dry sump yielded a 24 percent reduction in torque, **Figure 6.3.5-2.** Clearly the dry sump technology provides a reduction in parasitic loss due to churning.

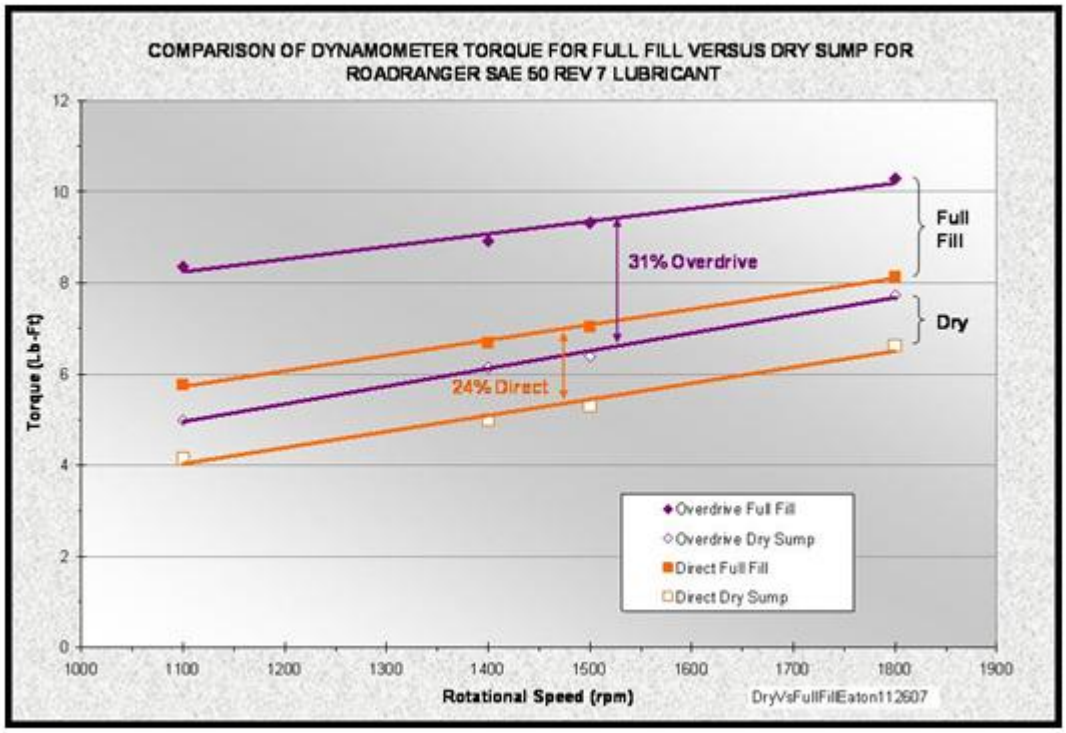

Figure 6.3.5-1: Eaton dynamometer test run with a conventional transmission and a similar transmission with a reduced fill, dry sump. The dry sump significantly reduced parasitic torque.

Caterpillar – Oils, Dry Sump and Churning

Caterpillar continued to examine the relationship between oil formulations and churning loss. Caterpillar systematically reduced the number of candidate oils to four. Oil #1 uses a synthetic polyalphaolefin (PAO) base stock, while Oil #11 has mineral oil base stock. Synthetic base stock oils like Oil #1 provide high efficiency at high speed hydrodynamic lubrication. Mineral oil base-stock lubricants like Oil #11 provide high efficiency at low speed where boundary or mixed lubrication is prevalent. Oil #20 is a fully synthetic product using the PAO base stock of Oil #1 and the Oil #11 additive package. It performs like Oil #11 at low film thickness (1 m/s) and like Oil #1 at high film thickness (4 m/s). Oil #20 is an excellent choice to provide high efficiency in highly stressed gear contacts that operate for significant portions of their life in both boundary/mixed and full film lubrication regimes. Further details on the four Caterpillar oils appear below in **Table 6.3.5-1.**

Table 6.3.5-1: Data for Caterpillar candidate oils.

Candidate Lubricants					
Number	Type	Basestock	Viscosity - cSt		Comments
			@40°C	@100°C	
1	Gear Oil, API GL-5	PAO Synthetic	185	25.5	
11	Industrial Gear Oil, AGMA 5EP	Mineral	183	19	
18	Final Drive & Axle Oil	Mineral	215	19	Baseline
20	Industrial Gear Oil	PAO Synthetic	338	35	

Figure 6.3.5-2 presents the parasitic torque for the four Caterpillar oils tested at 30 degrees C (86 degrees F), a temperature selected to simulate start-up or cold weather operation. The test shown in **Figure 6.3.5-2** provides friction torque measurements across a speed range approximately twice as large as typically experienced by large on-highway trucks. The large speed range provides data pertinent to certain off-highway equipment as well. Measurements were made with two lubricant sump configurations: 1) "full sump", conventional dip lubrication with an oil fill level at the center of the bevel gear and 2) "dry sump", with no oil in the gear housing. For the dry sump test, forced lubrication is provided to all bearings and the bevel gear. The dry sump eliminates dipping of the components into the bath of oil and thereby should eliminate the accompanying higher churning loss.

Figure 6.3.5-2 documents significant parasitic torque for all lubricants, and for both full sump (centerline fill) and dry sump configurations. Oil additives seem to have little impact but viscosity seems to be a key in determining the churning loss at low temperature. Oil #20 having the highest viscosity (338 cSt @ 40 degrees C) exhibits the greatest parasitic torque for both sump configurations. Oils # 1, #11 and #18, with 40 degrees C viscosities ranging only from 183 to 215 cSt, cluster together for both full sump and dry sump conditions.

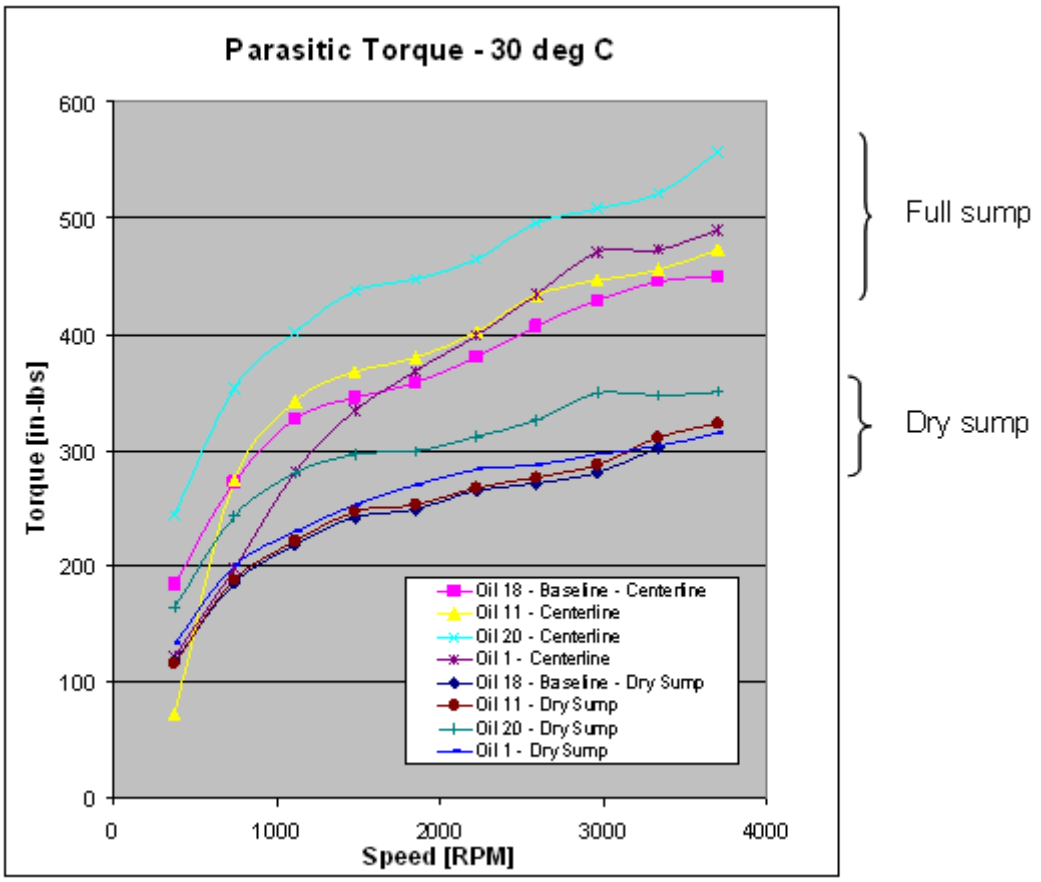

Figure 6.3.5-2: Parasitic torque for four Caterpillar oils tested at 30 degrees C (86 degrees F), a temperature selected to simulate start-up or cold weather operation.

The dry sump system clearly shows reduced parasitic loss compared to the full sump (centerline fill). For high viscosity Oil #20 the reduction in parasitic torque due to the dry sump exceeds 30 percent (at 2000 and 3000 rpm). For lowest viscosity Oil #11 the reduction in parasitic torque approaches 35 percent. If a full sump with Oil #20, 338 cSt, is compared to a dry sump with Oil #11, 183 cSt, at a speed of 2000 rpm, *the reduction in parasitic loss approaches 45 percent.*

Figure 6.3.5-3 shows the same type of data as **Figure 6.3.5-2** but for a lube temperature of 60 degrees C (140 degrees F), a temperature cooler than a typical operating condition. The point was used to see whether a significant difference would be seen with steady, incremental increases in temperature. In **Figure 6.3.5-3** the lubricant candidates are generally separated by viscosity *with higher viscosity lubricants showing higher churning loss in each lubrication configuration*. If a full sump with Oil #20, 338 cSt, at 60 degrees C is compared to a dry sump with Oil #11, 183 cSt, at a speed of 2000 rpm, the reduction in parasitic loss approaches 25 percent.

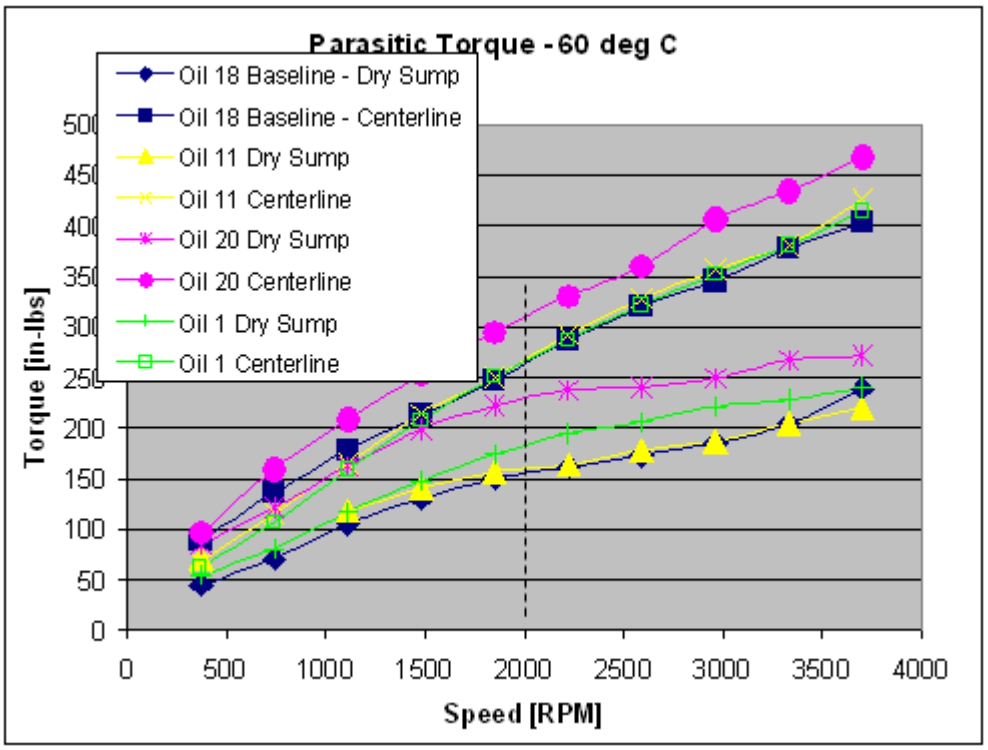

Figure 6.3.5-3: Parasitic loss for four Caterpillar oils tested at 60 degrees C (140 degrees F), cooler than the typical operating condition. Dry sump data clearly separates from the full sump (centerline fill) data.

A higher temperature of 90 degrees C (194 degrees F), a typical operating condition, is investigated in **Figure 6.3.5-3**. Dry sump data clearly separates from the full sump (centerline fill) data. Separation by viscosity also is apparent. High viscosity lubricant gives high churning loss for each sump configuration.

At the increased temperature the full sump (centerline fill) parasitic torque is much higher than the dry sump. For a speed about 2000 rpm, the dry sump used with Baseline Oil #18 (19 cSt viscosity at 100 degrees C) exhibits *over 47 percent reduction in parasitic loss* compared to the full sump. For the higher speeds of many off-highway applications, the benefit of dry sump is even greater, 55 percent at 3330 rpm.

If a full sump of high viscosity Oil #20 (25.5 cSt at 100 degrees C) is compared to a dry sump of lower viscosity Oil #11 (19 cSt at 100 degrees C), then the difference in parasitic loss is staggering, shown in **Figure 6.3.5-3**. The combination of *dry sump and low viscosity oil reduces parasitic loss by 57 percent.*

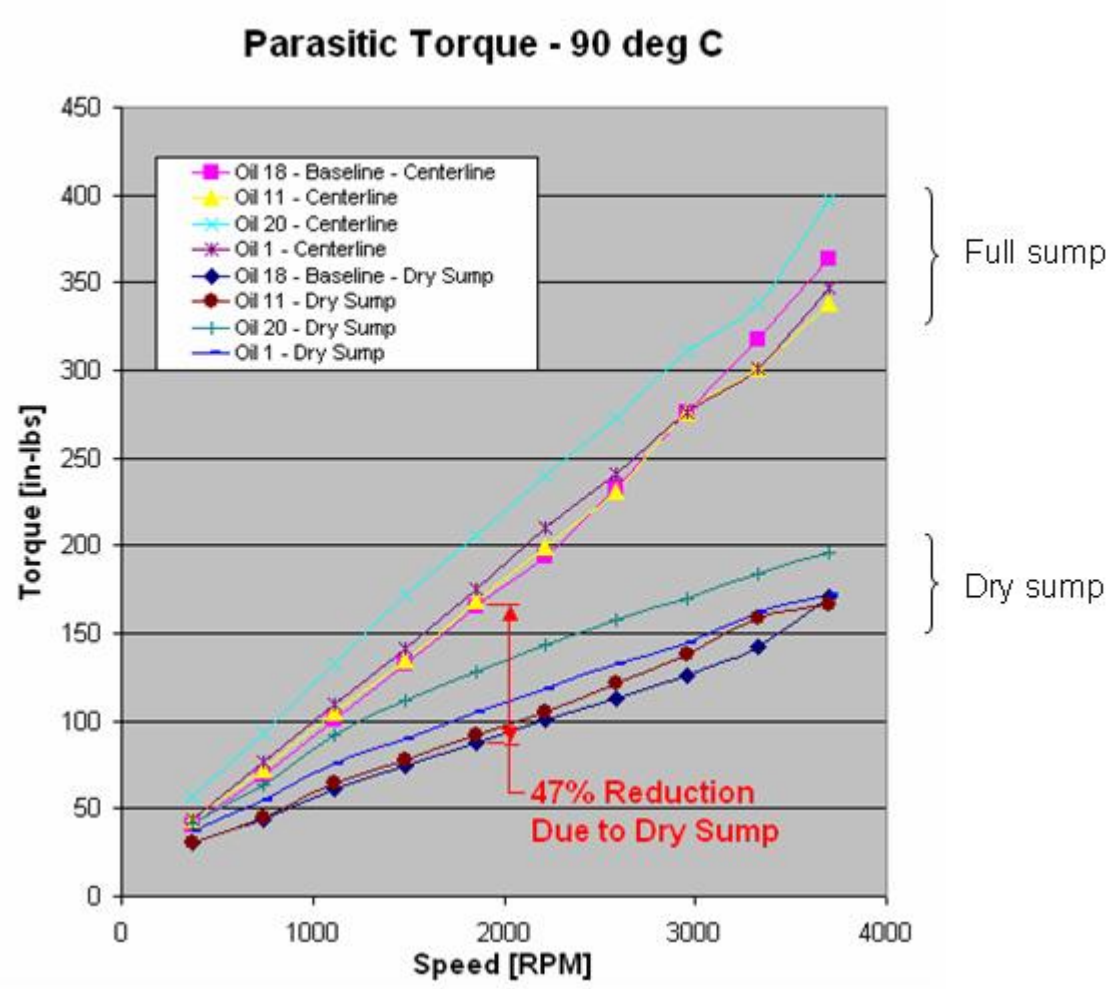

Figure 6.3.5-4: **Parasitic loss for four Caterpillar oils tested at 90 degrees C (194 degrees F), a typical operating condition. Dry sump data clearly separates from the full sump (centerline fill) data. Dry sump provides 47 percent reduction in parasitic loss.**

Caterpillar also tested the Baseline Oil #18 at the centerline fill (full fill) and at levels below the centerline (low fills), **Figure 6.3.5-5.** This data clearly shows the progressive change in parasitic torque as the fill level is decreased. As the oil level decreases, the churning loss decreases. At 2000 rpm *the parasitic torque with Oil #18 filled only to the dry sump level (low fill) is 49 percent less than the torque for a centerline fill (full fill).*

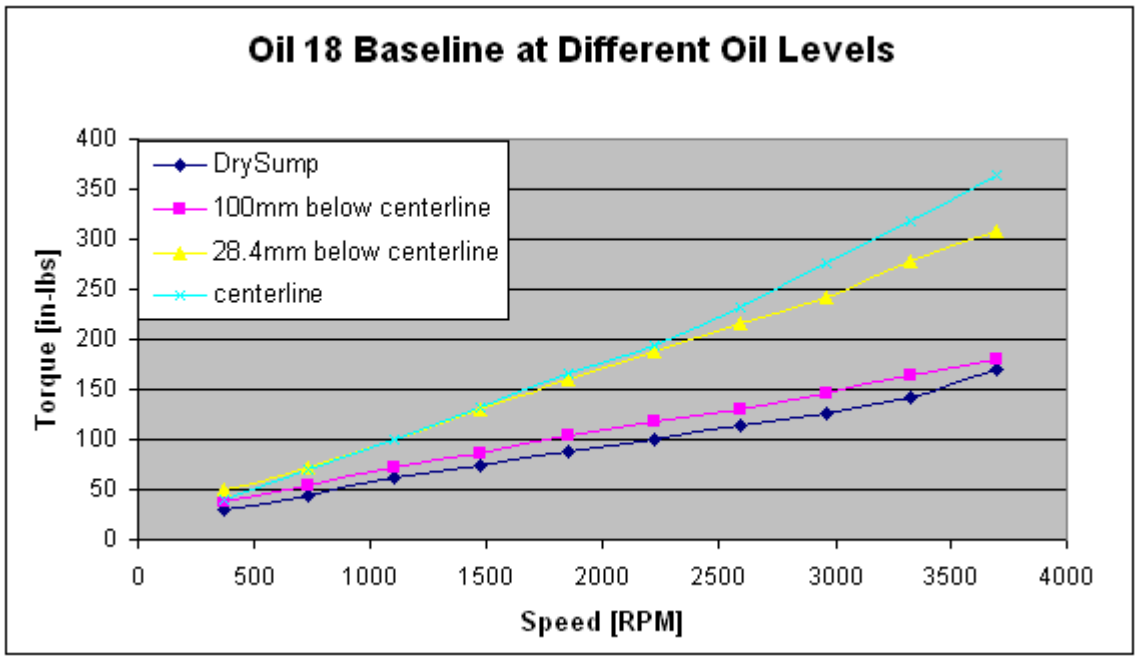

Figure 6.3.5-5: Baseline Oil #18 was tested at four fill levels. As the fill level decreases from a centerline fill (full fill) to the dry sump level (low fill), the parasitic torque decreases by 49 percent.

6.4 Budget Period 4

Deliverables

20. Integrated design model for low friction gears, bearings and seals
21. Integrated efficiency and durability predictive tools
22. Process techniques to overcome difficulties with gear geometry effects and temperature effects
23. Test data to support use of coated gears in transmission dynamometer tests
24. Dynamometer and durability test results for low friction driveline components
25. Dynamometer test results using a low friction axle and transmission prototypes

6.4.1 Integrated design model for Gears

Figure 6.4.1-1 illustrates the strategy (flow chart) for designing gear systems with high efficiency and high fatigue life that considers gear geometry, surface finish, material selection, and lubricant usage. The fatigue life prediction result mentioned in area (1) is an example of the application of this strategy.

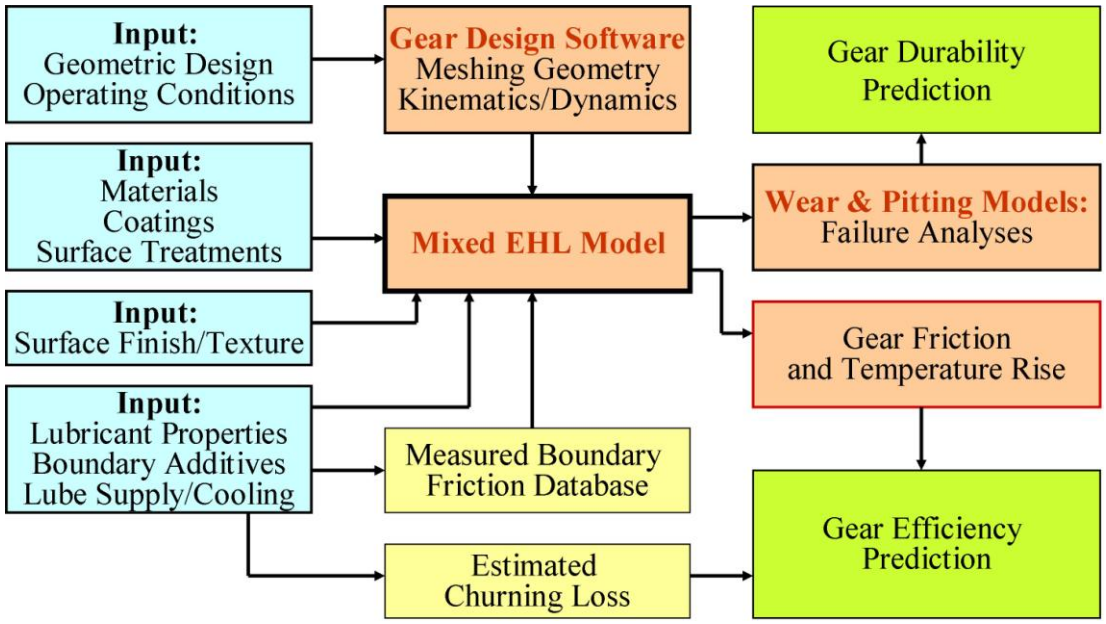

Figure 6.4.1-1: Strategy for designing high efficiency and high fatigue resistant gear systems.

Reduction of boundary friction via use of lubricant additives, reduction of the total contact area in the interface area by optimization of surface finish/texture and operating conditions, and reduction of hydrodynamic friction by the choice of low-shear lubricants are three elements for energy efficiency. One key advantage of the present mixed EHL model is its ability to evaluate the impact of these friction reduction methods in combination. The simulation was run with the same operating conditions as were introduced in the individual friction reduction elements using a high limiting shear stress mineral oil and a representative synthetic low-shear lubricant, with and without low friction additives, and six different rough surfaces. **Figure 6.4.1-2** illustrates the resultant friction predicted by the simulation under varying surface roughness, lubricant, and additive combinations. This figure clearly illustrates the potential for friction reduction through combination of the methods discussed in this paper. The baseline (identified as *Current* in **Figure 6.4.1-2**) for many drive train components in heavy-duty machinery are ground or shaved surfaces lubricated by a mineral oil. The simulation predicted friction coefficient under these conditions is in the range of 0.07-0.08 which can typically be found in transmission gears. Through introduction of smoother, polished surfaces, a low-shear lubricant and use of a friction modifier (identified as *Target* in **Figure 6.3.4-7**) a significantly reduced friction coefficient of around 0.02-0.03 can be obtained. Each of these friction reduction means is currently available in the market, and therefore can be implemented in drive train components such as gears, bearings, cams and followers, etc. to feasibly achieve frictional loss reduction and efficiency improvement.

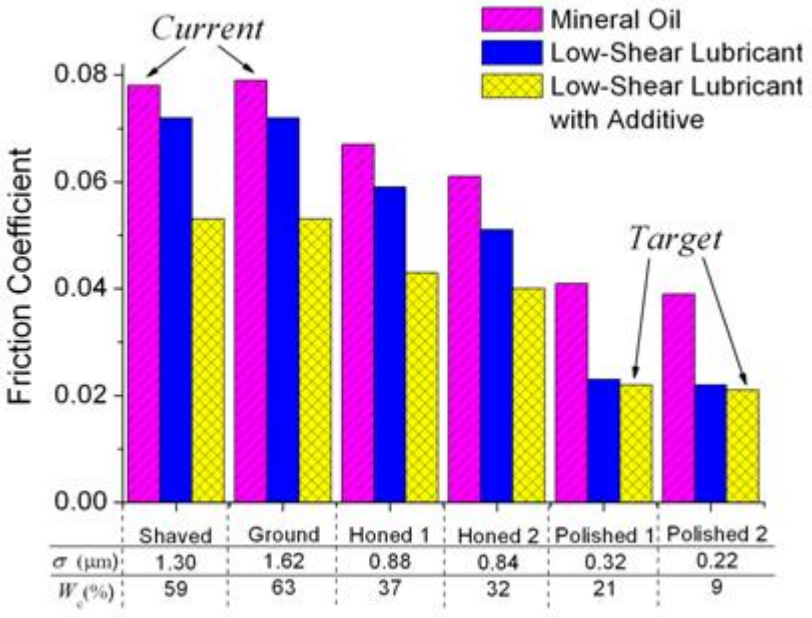

Figure 6.4.1-2: Illustration of the combined effects of surface topography (composite roughness decreasing from left to right) and lubricant selection (mineral oil, low-shear lubricant, and low-shear lubricant with additive) on friction reduction in mixed lubrication. The current and target conditions are identified.

Pitting life prediction-Background

Surface pitting due to contact fatigue is a major failure mode of many mechanical components, such as various gears and rolling element bearings. Pitting life prediction is therefore vital to design and performance and reliability improvements. In practice, pitting strength has been evaluated by design engineers with procedures documented in various industrial standards that were originally developed under assumptions that surfaces were ideally smooth with no lubrication. Empirical parameters have then been introduced for modifications. Examples of the standards include ANSI/AGMA 2001-C95(1995), ISO-6336(1996) and DIN-3990(1987) for gears, and DIN ISO 281 (2007) for rolling element bearings. For spur and helical gears, for example, gear tooth contact geometry is simplified to two equivalent cylinders under a normal load *F*, and the maximum contact pressure is calculated with the Hertzian theory. The maximum Hertzian contact pressure, P_H, is then employed for the failure criterion:

$$\sigma_{\max} = P_H = \sqrt{\frac{FE'}{2\pi R_x l}} \leq [\sigma] \qquad (1)$$

In the above formula, *E'* is the effective Young's modulus, R_x the effective radius of curvature, and *l* the contact length. Design engineers need to ensure that σ_{max} is always smaller than a predetermined permissible stress value $[\sigma]$ in order to avoid unacceptable surface pitting. As more and more testing data have been accumulated, the pitting strength evaluation methods have been experimentally/empirically improved to include many modification factors in the formula. In ANSI/AGMA 2001-C95, for example, the modified design criterion is expressed as

$$\sigma_{\max} = P_H = Z_E \sqrt{\frac{F K_o K_v K_S K_H Z_R}{d_{w1} l Z_I}} \le \frac{\sigma_{\lim} Z_N Z_W}{S_H Y_\theta Y_Z} \qquad (2)$$

Equation (2) is basically in the same form as Equation (1), except that modification factors, K_o, K_v, K_S, K_H, Z_R, Z_I, Z_W, S_H, ……etc, were added to take into account the effects of overloading, dynamic loading, non-uniform load distribution, gear size, surface condition, gear geometry, hardness ratio, and safety factor, and so on. It appears that even in the updated ANSI/AGMA standard, no sufficient attention has been paid to the effects of lubrication condition and surface finish/texture, which may indeed have great influences on gear pitting life.

It is well known that for commonly used ductile materials (such as steels) in concentrated contact problems, material failures are better correlated with the subsurface von Mises stress, rather than the normal Hertzian pressure, according to the maximum distortional strain energy theory. The following failure criterion, therefore, is theoretically more appropriate:

$$\sigma_{vM\max} = \left[\frac{1}{2}\left((\sigma_1 - \sigma_2)^2 + (\sigma_2 - \sigma_3)^2 + (\sigma_1 - \sigma_3)^2\right)\right]^{1/2} \le [\sigma] \qquad (3)$$

The von Mises stress is much more difficult to calculate, especially if the effects of lubrication condition and the surface roughness/topography need to be considered. Basically, simplified pitting strength analyses were employed in the past, mainly because only simple manual calculation tools, such as slide rules and calculators, were available to engineers at that time. Today's trend of high power density, high reliability compact design, which requires the life prediction to consider severe operation conditions in mixed lubrication and the effect of surface roughness and topography, and the powerful advancement of computer technologies encourage re-thinking in gear design and fatigue life analysis.

Pitting Life Prediction-Results

Fifteen sets of transmission gears have been analyzed and their pitting lives predicted by employing the 3-D line contact mixed-EHL model, the von Mises stress calculation procedure, and the fatigue life model described above. The prediction results are correlated with available experimental data. Before the mixed-EHL analysis, the gear tooth contact geometry, entraining and sliding velocities, the normal load applied to each pair of teeth and the local maximum Hertzian contact pressure at "SAP" locations are determined by using the "Helical Gear Code" originally developed by Zhu and Cheng [1991]. Note that "SAP" stands for "start of active involute profile" below pitch line, which is where the most severe gear tooth pitting failure is often observed. It is well known that the actual contact between gear teeth in spur and helical gears can be simplified as 2-D straight lines, whose location, length and movement can be precisely determined by gear analysis programs such as the Helical Gear Code [Zhu and Cheng, 1991]. However, the gear tooth surface topography is usually 3-D. That is why the 3-D line contact mixed-EHL model is needed in order to obtain detailed contact and lubrication characteristics.

Digitized surface topography data for different machined gear teeth have been used as input data to the 3-D line contact mixed-EHL analyses. The von Mises stress distributions obtained are

used in Equation (9). If the probability of survival and other materials related parameters, stress exponent c and Weibull slope e, are given, one can then readily solve Equation (9) for pitting life as the number of contact cycles before pitting failure. Notice that, from the previous studies mentioned above, fatigue life under a certain probability is closely related to material parameters, including the Weibull slope e and the stress exponent c. In the present study, the probability of survival is assumed to be 50 percent.

Predicted pitting lives for the 15 sets of gears are given in **Figure 6.4.1-3** in comparison with available testing results. The predicted life, shown as a blue dot for each gear set, is often located close to the average of the test data expressed by the red dots for the same gear set. It appears that the agreement between the prediction and tests is good for most cases.

In order to see the correlation more clearly, the same data in **Figure 6.4.1-3** are reorganized in **Figure 6.4.1-4**, in which the predicted life is compared directly with the experimental mean taken from the tests for each gear set. Note that if a dot sits exactly on the diagonal line in **Figure 6.4.1-4**, it would represent a perfect agreement between the prediction and the experiments. This figure shows that the dots for most gear sets are located quite close to the diagonal line. Such a good agreement suggests that the pitting life model and the material parameters used in the present study are appropriate for this type of transmission gear applications under the same or similar conditions.

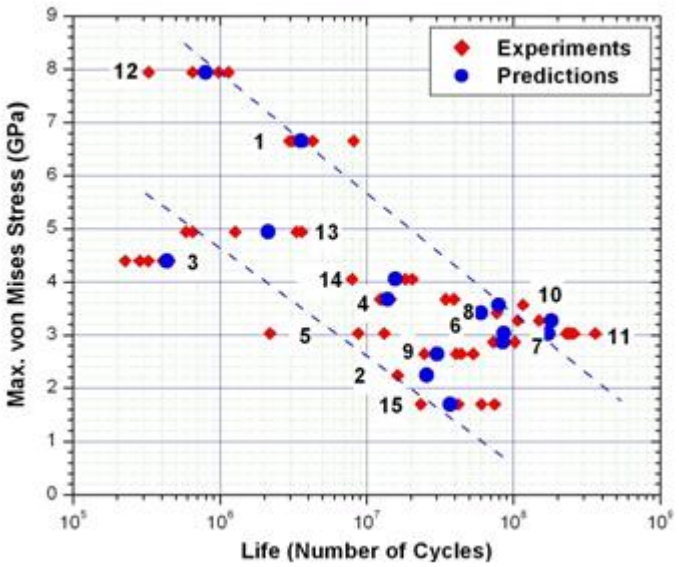

Figure 6.4.1-3: Pitting Life Prediction Results in Comparison with Gear Test Data

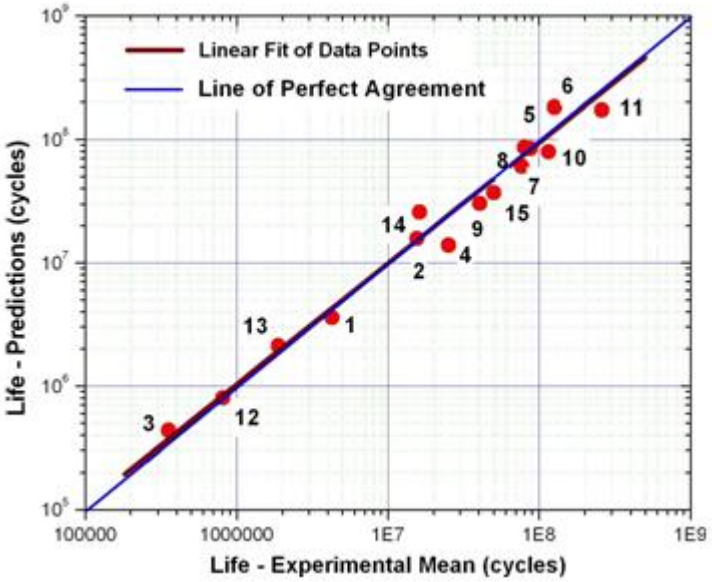

Figure 6.4.1-4: Pitting Life Prediction Results Showing Good Correlation with Test Data

Rolling Fatigue Prediction-Background

Contact fatigue is one of the major failure mechanisms for engineering surface under cyclic rolling loads. Theoretical and empirical models have been developed to predict it over the decades. Among them, Lundberg-Palmgren equation is a widely used stochastic method. The effect of plasticity was not considered in the traditional Lundberg-Palmgren model however. A modified Lundberg-Palmgren equation is used in this report, which employed the subsurface stress, including both elastic stress and residual stress.

Rolling Fatigue Prediction-Results

Rolling contact simulation was performed between a rigid smooth ball and an elastic-plastic ball with rough surface. The subsurface space of the elastic-plastic ball was cut and extended to a flat space, **Figure 6.4.1-5**. The rough surface used here is a chemical-mechanical machined surface with *RMS* roughness 179 *nm*. The corresponding friction coefficient is 0.1. The calculated von Mises stresses, residual stresses, and plastic strains in the center cross section are shown in **Figure 6.4.1-6.** The track of the equivalent stress at point A and B was shown in **Figure 6.4.1-6**. It is found that the stress reach stable after the third cycle.

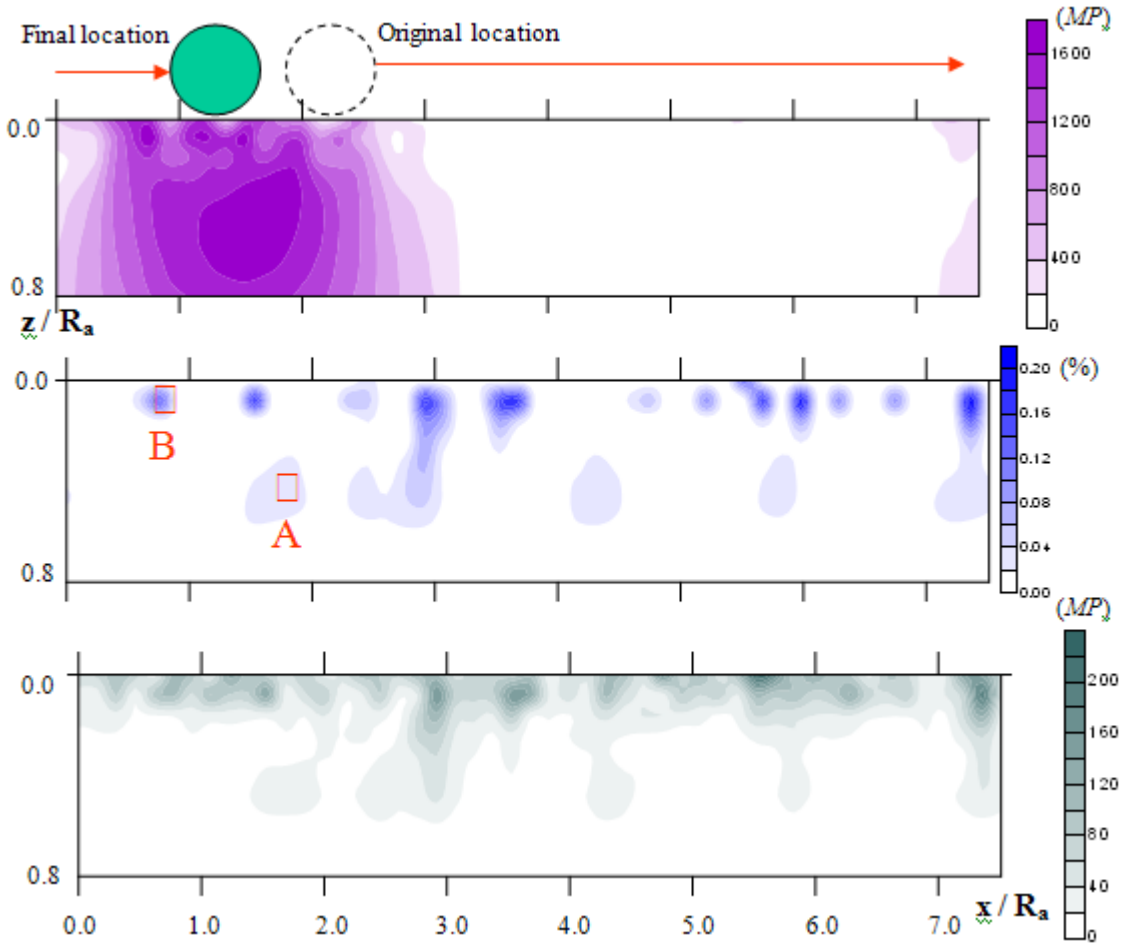

Figure 6.4.1-5: Subsurface stress and strain fields after one rolling cycle.

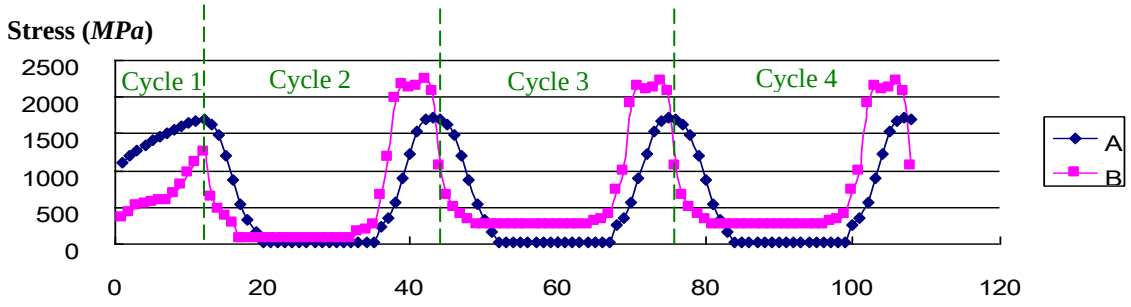

Figure 6.4.1-6: Traction of equivalent stress at point A and B for the first 4 cycles

The predicted fatigue life with elastic-plastic model and elastic-perfectly plastic model for smooth and rough contact cases are obtained using modified Lundberg-Palmgren equation. They are normalized by N_0 (fatigue life of smooth contact with elastic-perfectly plastic model) and shown in **Figure 6.4.1-7**. It is found that the larger fatigue life occurs for smooth contact. Because the rough surface induces the stress concentration at local contact regions, decreasing the integral of the effective stress in the entire volume, therefore decreases the fatigue life.

The results also show that the fatigue life calculated from elastic-plastic model is larger than the corresponding results from elastic-perfectly plastic mode. The elastic-plastic model is more robust than the elastic-perfectly plastic model because the former incorporates the plastic limit, the residual stress, and the surface modification due to the plastic deformation when determining the subsurface stress field. The letter however only considers the pressure limit effect. **Table 6.4.1-1** gives the von Mises stress and the six components of deviatoric stress at a particular point where the maximum von Mises total stress occurs. In the elastic-plastic model, the total deviatoric stress equals the sum of elastic and residual deviatoric stresses. The results indicate that the sign of S_{ij}^{e} is always the reverse of the sign of S_{ij}^{r}. Therefore, the value of each component of S_{ij}^{total} is always smaller than the corresponding S_{ij}^{e}. The von Mises total stress is therefore smaller than the von Mises elastic stress, which leads to the deduction of the fatigue life of elastic-perfectly plastic model.

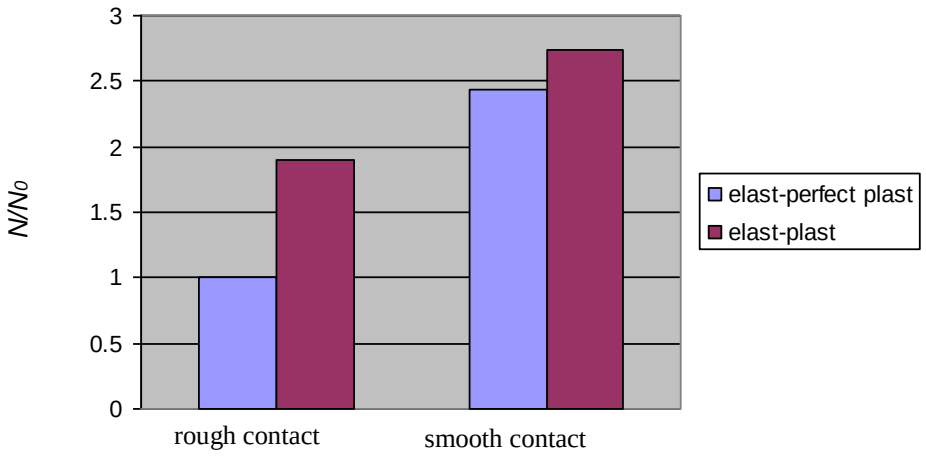

Figure 6.4.1-7: Normalized contact fatigue lives for different models

Table 6.4.1-1: Stress components at a particular point for different models, unit (MPa)

Model	Stress components	S_{11}	S_{22}	S_{33}	S_{12}	S_{13}	S_{23}	σ_{VM}
Elastic-plastic	Elastic, S_{ij}^{e}	453	343	-796	99	-281	205	1351
	Residual, S_{ij}^{r}	-57	-30	87	-20	20	-17	145
	Total, S_{ij}^{total}	396	313	709	79	-261	188	1210
Elastic-perfectly plastic	Elastic, S_{ij}^{e}	456	344	-801	106	-275	209	1360

6.4.2 Durability Prediction

Wear simulation

Sliding wear is a significant surface failure mode in many mechanical components. The magnitude of changes in surface topography due to wear may be comparable to or larger than the original surface roughness and elastic deformation. In addition, wear induced changes in the size and shape of the contact area may alter the direction and magnitude of forces that act on the surface. As a consequence, machine component functionality may be affected. However, these effects have rarely been incorporated into numerical simulation models used as predictive tools in engineering practice. There are two primary difficulties that have been obstacles in the wear simulation research. First, the amount of wear is directly related to local lubrication effectiveness and contact severity, which are difficult to quantify in mixed lubrication, especially when a full-scale deterministic model is not available. Smooth surface assumption and stochastic surface models may not be satisfactory for the prediction of local contact severity and application of material failure criteria. A good model needs to incorporate the effects of hydrodynamic flow, elastic deformation of the contacting bodies, surface roughness and topography, as well as possible change of viscosity and density with pressure. Simple models with one or two stochastic parameters may not be sufficient to describe these integrated and complicated phenomena. The second difficulty is the mutual dependency of wear and mixed lubrication characteristics. Wear changes the surface topography in real time. The surface topography may, in turn, significantly affect mixed lubrication characteristics and the contact severity. Contact severity may then greatly influence the wear process immediately. This interdependency is difficult to describe with simplified time-independent models, and satisfactory solution may require a transient deterministic simulation.

Wear takes place at locations where surfaces are in direct contact. The amount of material removal is directly correlated to "contact severity", which is a complicated concept that may involve contact pressure, sliding speed, asperity deformation, interfacial temperature, friction, subsurface stresses and some other parameters. Depending on the problem, contact severity may need to be described in different ways. Recently, deterministic mixed lubrication models have been developed (such as those presented by Zhu and Hu [2001]), which solve both hydrodynamic lubrication and surface contact simultaneously, and predict the distributions of pressure, film thickness, asperity deformation, subsurface stresses, friction and interfacial temperature, etc. as functions of location and time. Also, the deterministic simulation is based on real measured digitized surface topography, so that arguments on selection and application of stochastic parameters can be avoided. This enables application of a more sophisticated approach that provides a full numerical transient mixed lubrication model, capable of predicting contact severity at local spots, and the ability to handle the mutual dependency between wear and mixed lubrication characteristics.

Surface Topography Evolution

One analysis that can be performed using the transient solution generated by the present wear model is that of surface evolution over time. This is an important investigation because the evolution of surface topography is readily captured using experimental techniques and therefore may be used for model validation. The evolution of the two surfaces predicted by the ball-on-disk simulation is shown in **Figure 6.4.2-1.**

There is no visible wear track on the disk, or scar on the ball before wear is introduced. Then, the contrast between the worn and unworn areas on the surfaces increases. Both the ball and disk exhibit characteristic wear patterns typically observed in experimental studies of lubricated sliding contact. The worn disk surface contains a track with texturing parallel to the direction of sliding. And the ball surface is worn first at the contact inlet. Both of these trends agree with experimental observations.

A similar surface evolution analysis was performed for the ground surface simulation. Snapshots of the two surfaces as they change over time are shown in **Figure 6.4.2-2.**

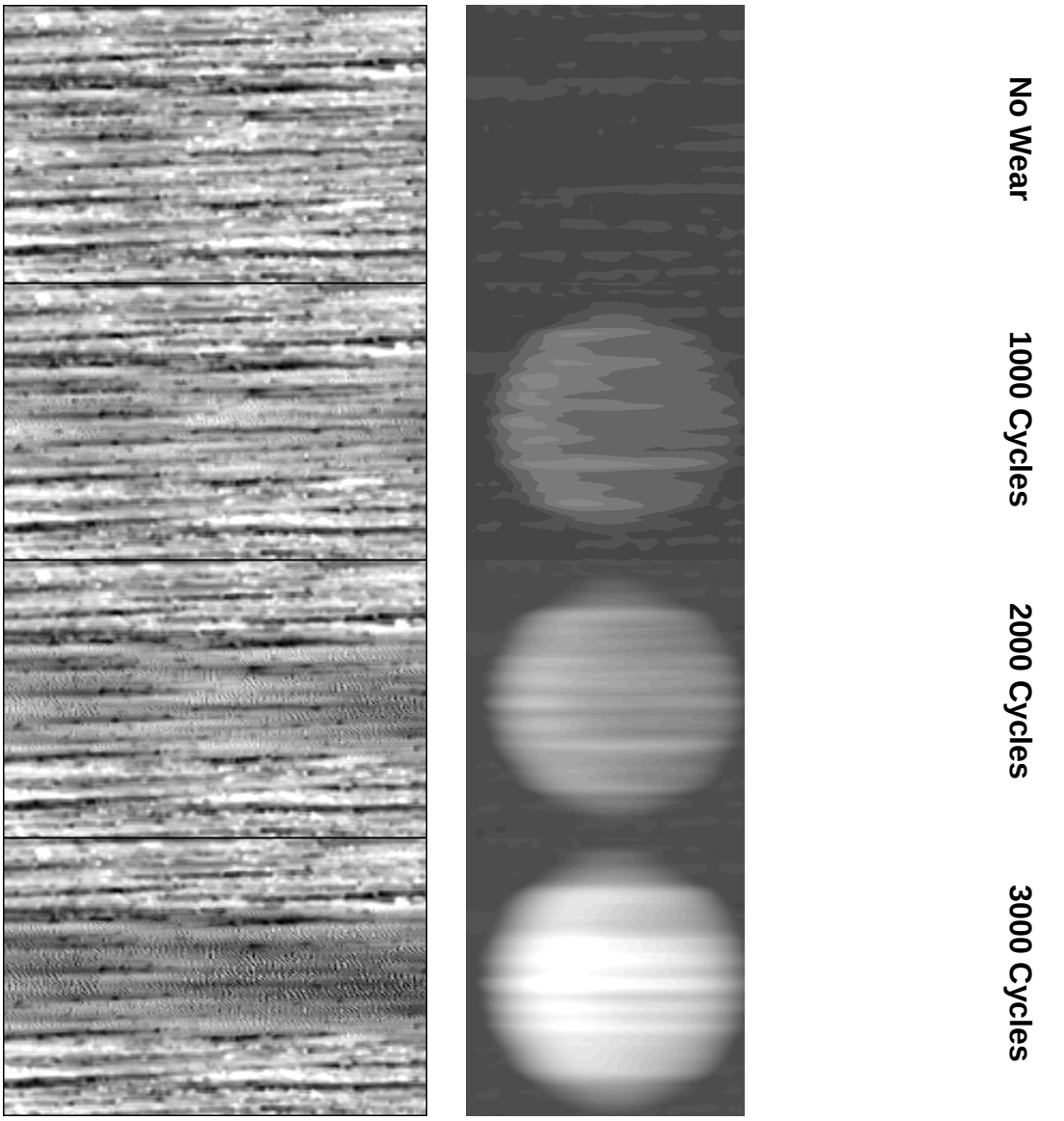

Figure 6.4.2-1: Evolution of the disk wear track (left) and ball wear scar (right) over time. Ball image length scale is larger than that of the disk to facilitate visual analysis.

Snapshots of the surfaces are shown without wear and at 1000, 2000, and 3000 cycles after the wear process begins.

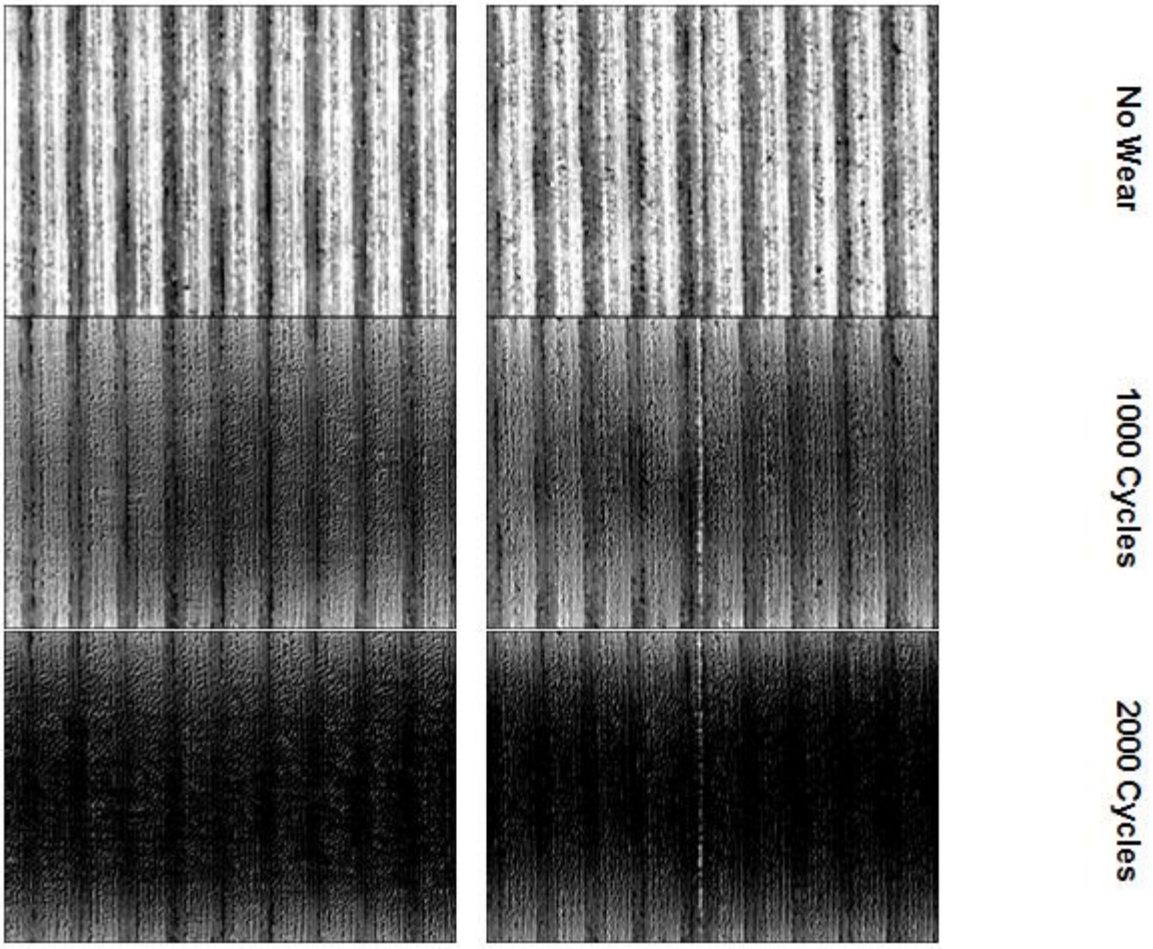

Figure 6.4.2-2: Evolution of the two ground surfaces moving at 3.75 m/s (left images) and 6.25 m/s (right image). Snapshots of the surfaces are shown without wear, and at 1000 and 2000 cycles after the onset of wear.

Contact Properties Before and After Wear

EHL simulations are frequently used to predict film thickness and pressure distributions in the contact area. Therefore, it is of interest to analyze these parameters before and after wear is incorporated into the simulation. Film thickness is represented by a contour plot where regions of dimensionless film thickness (normalized by the Hertz contact radius) less than 0.000002 (corresponding to small dimensional values less than 0.53-0.94 nm depending on the simulation case) are in white. Contact pressure is represented by a contour plot in which regions where the dimensionless pressure (normalized by Hertz pressure) greater than 1.3 are in white. For the sinusoidal surface case, this comparison is illustrated in **Figure 6.4.2-3.**

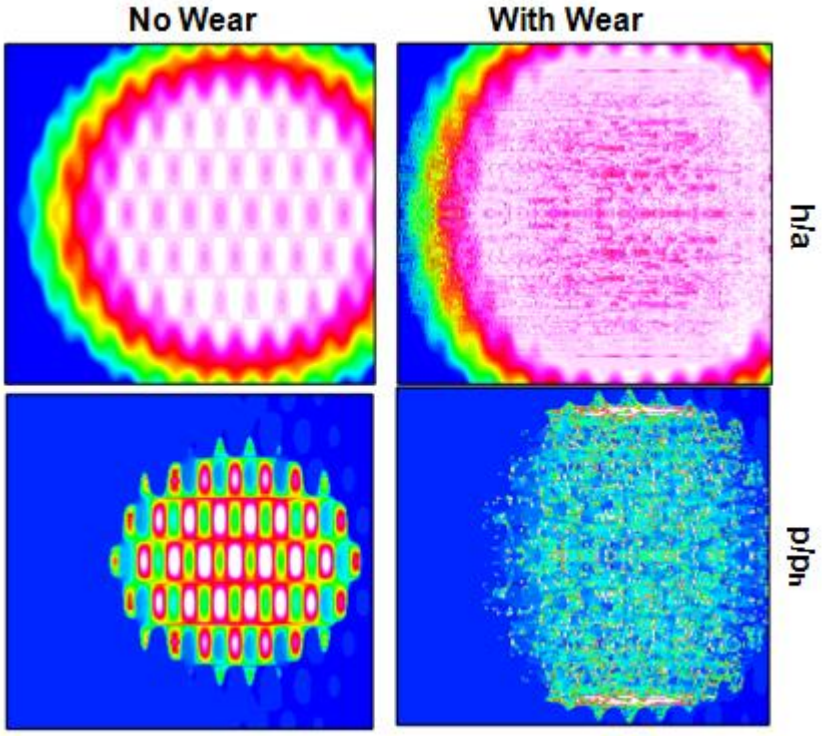

Figure 6.4.2-3: Film thickness (top) and pressure (bottom) distributions for the sinusoidal surface contact case simulated with (right) and without (left) wear.

Comparison of these images reveals two significant differences between the contact behavior before and after wear. First, the overall contact area is larger in the case with wear after 3,000 cycles. And second, the sinusoidal asperity peaks are reduced resulting in a more uniform overall appearance of the contact pressure and film thickness distributions.

The trends observed in the sinusoidal case were also found in simulation of ground surface contact. The contact pressure and film thickness distributions for the ground case are shown in **Figure 6.4.2-4.**

The ground surface film thickness and pressure distributions exhibit the same trends of larger contact area and increased uniformity as were observed with the sinusoidal case. In addition, the effect of an established wear track in each case is also to change the shape of the contact area from circular to elliptical. This phenomenon is described graphically by the simplified contact illustrations in **Figure 6.4.2-5.**

The effect of wear can also be identified through analysis of subsurface stress. The pre and post wear stress distributions for the ground case (shown with the centerline film thickness and pressure for clarity) are illustrated in **Figure 6.4.2-6.**

Analysis of the ground surface stress distributions reveals that the changes in the contact area due to wear have a significant effect on subsurface stress. The large stresses just below the surface (caused by severe contact between asperity peaks) move closer to the surface due to the

reduction of asperity size with wear. As larger asperity peaks are removed, the smaller, high frequency asperities become more prevalent. This results in an increase in frequency of the corresponding near surface stress peaks. Wear also affects the stress further below the surface due to the change of the contact shape and the corresponding redistribution of the overall stress field. The effects that wear-induced contact area changes have on stress are particularly critical as they have been found to accelerate failure modes in addition to material loss.

Pre and post wear analyses were also performed for the ball-on-disk case. The film thickness and pressure distributions for this simulation case are illustrated in **Figure 6.4.2-7.**

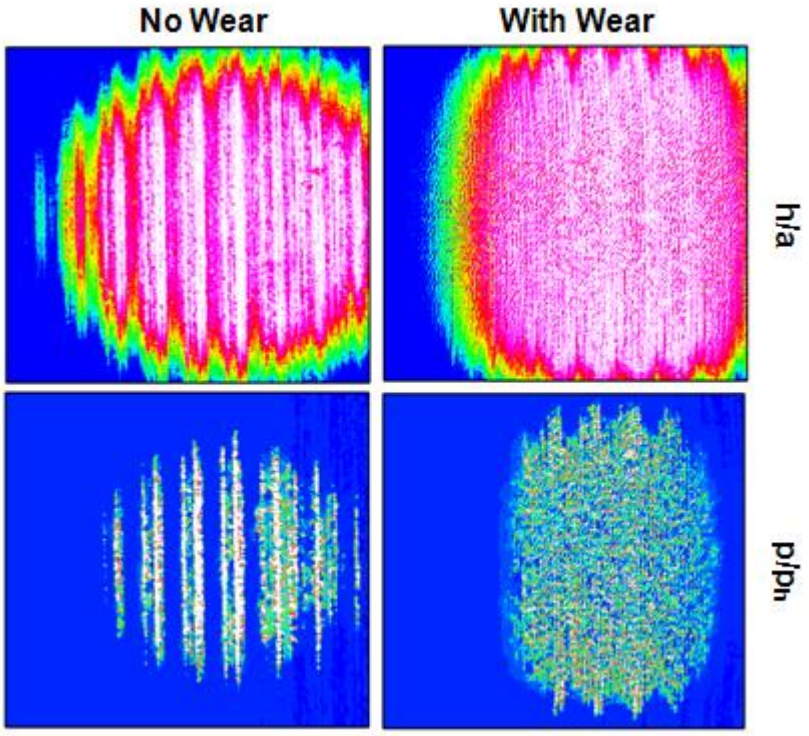

Figure 6.4.2-4: Film thickness (top) and pressure (bottom) distributions for the ground surface contact case simulated with (right) and without (left) wear.

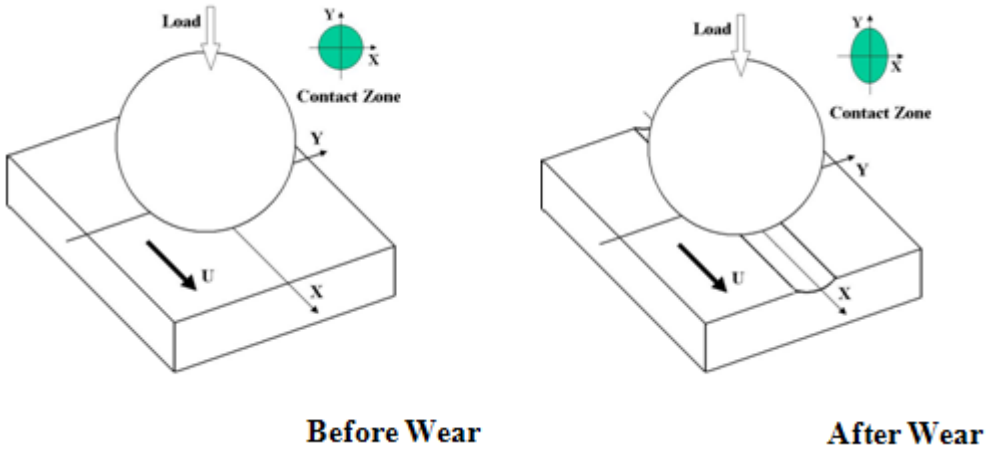

Figure 6.4.2-5: Illustration of the shape change of the contact zone due to an established wear track.

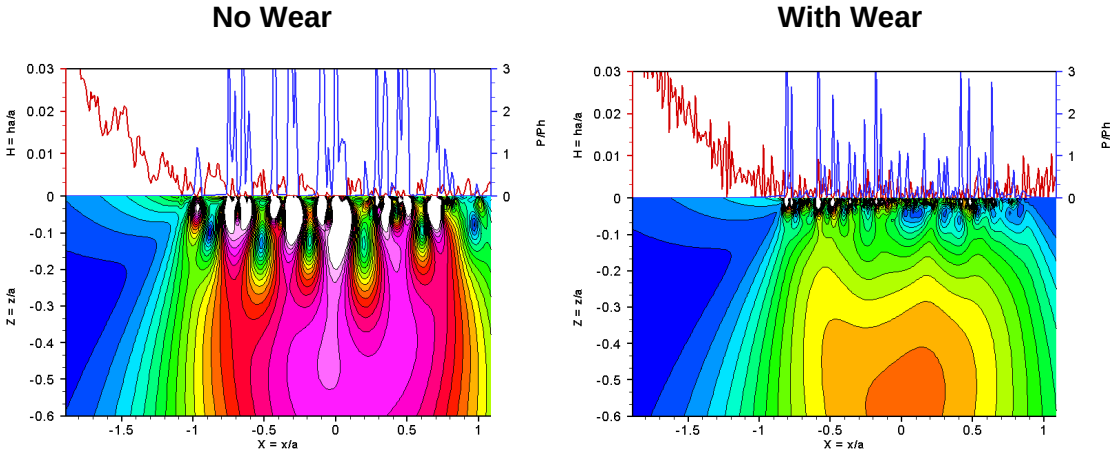

Figure 6.4.2-6: Centerline subsurface stress distribution with (right) and without (left) wear for the ground surface contact case. Dimensionless centerline pressure and film thickness shown above the stress distribution for clarity.

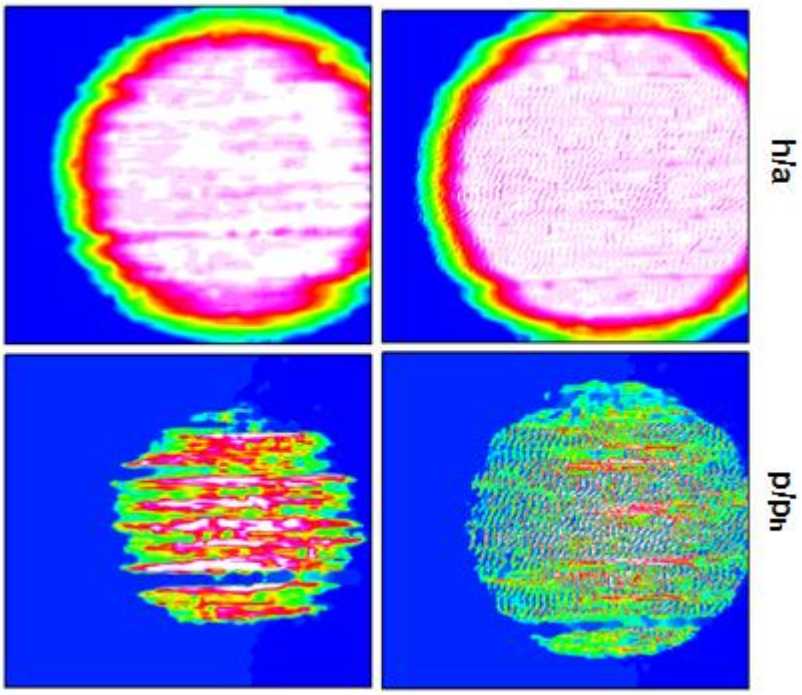

Figure 6.4.2-7: Film thickness (top) and pressure (bottom) distributions for the ball-on-disk contact case simulated with (right) and without (left) wear.

The ball-on-disk contact simulation exhibits the same trends of contact area expansion and increased uniformity as were observed in the sinusoidal and ground cases. However, the shape of the contact area does not appear to change as much as it did the ground case. The ball-on-disk case exhibited one feature not observed in the ground case where the center of the contact area in the direction of sliding was more affected by the wear than the outer edges. This is due to the fact that only one of the surfaces is moving in the ball-on-disk case whereas both are moving in the ground contact. The effect of wear on subsurface stress for the ball-on-disk case was analyzed as illustrated in **Figure 6.4.2-8.**

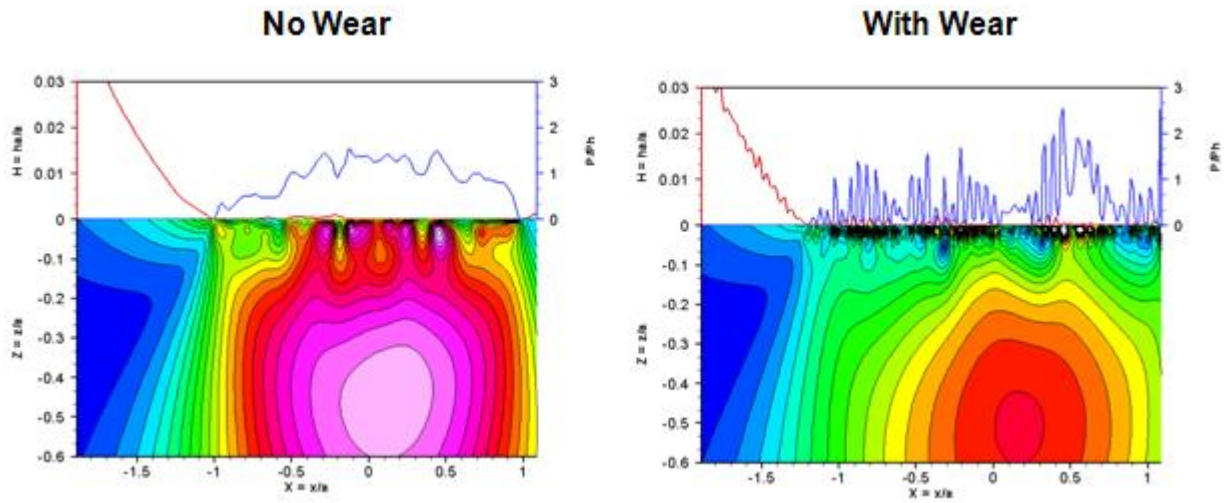

Figure 6.4.2-8: Centerline subsurface stress distribution with (right) and without (left) wear for the ball-on-disk case. Dimensionless centerline pressure and film thickness shown above the stress distribution for clarity.

The subsurface stress in the ball-on-disk case underwent redistribution due to wear similar to that observed with the ground surfaces. The near surface stress peaks moved closer to the surface and increased in frequency while the global contact stress decreased. In addition, wear causes the location of the global contact stress to move further from the surface. This is a direct result of the increased overall contact area.

Phases of Wear

A typical system may be subject to wear in three phases: Initial running-in, relatively steady state, and accelerated or catastrophic wear. The running-in phase occurs in the beginning and is associated with a high wear rate. During the running-in phase, tall asperity peaks are quickly removed and the surfaces become smoother. After the tallest peaks are removed, the wear rate decreases and gradually stabilizes. In the steady-state stage, the wear rate is relatively stable, and it is in this phase that it is desirable for machine components to operate as long as possible. Lastly, in some cases, steady-state gives way to catastrophic wear in which the wear rate once again increases. This is only a general description of the overall wear process, and specific cases differ from one to another. In some cases, for example, the running-in may be too short to observe, while in other cases, a system may not undergo catastrophic wear even after a very long time. The expected phases of wear were evaluated using the present simulation by analysis of the change in wear volume removed from the surface over time. This analysis is illustrated in **Figure 6.4.2-9**.

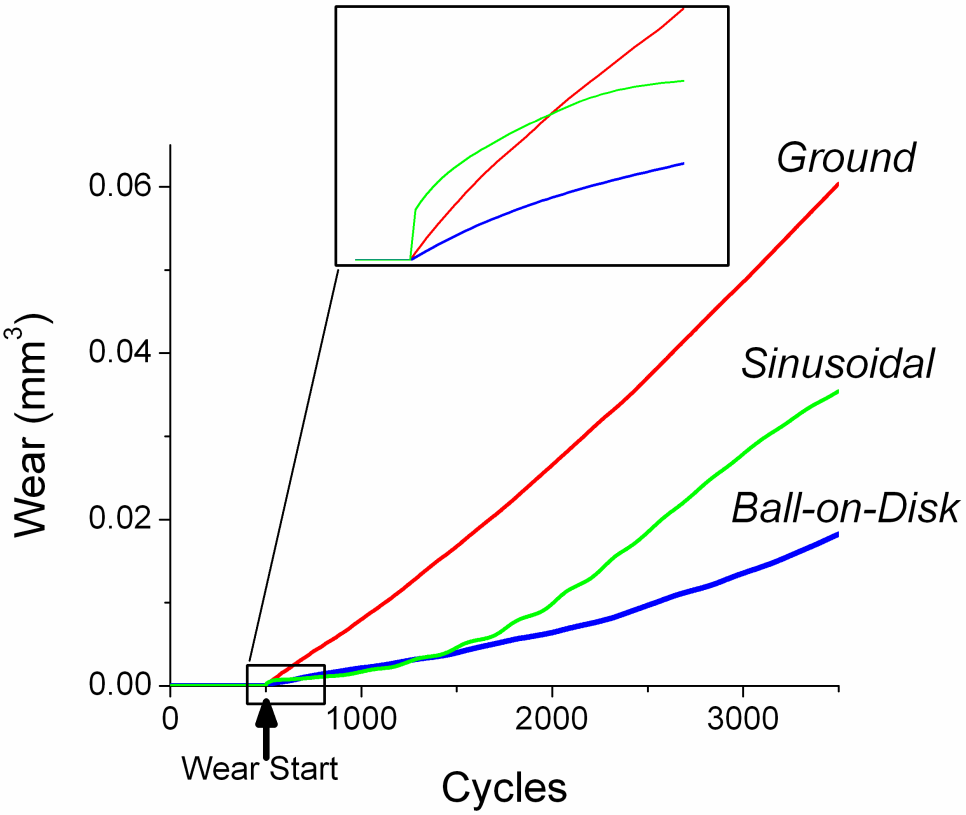

Figure 6.4.2-9: Wear volume as a function of time for the three contact simulation cases analyzed. Inset shows a close-up of trends observed at the onset of wear.

The first 500 cycles of the simulation run without wear. During this phase, as expected, there is no wear volume generated. Then, wear is introduced to the simulation. A close up view of the immediate response is illustrated in the inset of **Figure 6.4.2-9**. It can be seen from this image that there is a brief running-in period where the wear increases rapidly for all three cases. However, this increase is found to be most significant in the sinusoidal surface case and least significant in the ground surface case. These results are consistent with experimental observations of the running-in phase. Both rapid wear increase and variation of the intensity of this increase with different operating conditions have been reported by other researchers.

After running-in, the wear enters the steady state phase where the wear rate is relatively constant (i.e. constant wear-time curve slope); this phase appears to last quite long. The wear rate during the steady state phase is different for the three contact cases evaluated as seen from the slope of the curves in **Figure 6.4.2-9** where the ground surface wear rate is higher than the other two. This is consistent with experimental observations that fractional contact area increases due to wear most significantly on surfaces with transverse roughness such as the ground surfaces evaluated here. After this phase of relatively steady wear, the wear rate appears to gradually increase again indicating a transition to accelerated or catastrophic wear.

The phases of wear that a system goes through can, in some cases, be correlated to the change in the friction coefficient over time. The friction coefficients for each case calculated by the present simulation are given in **Figure 6.4.2-10.**

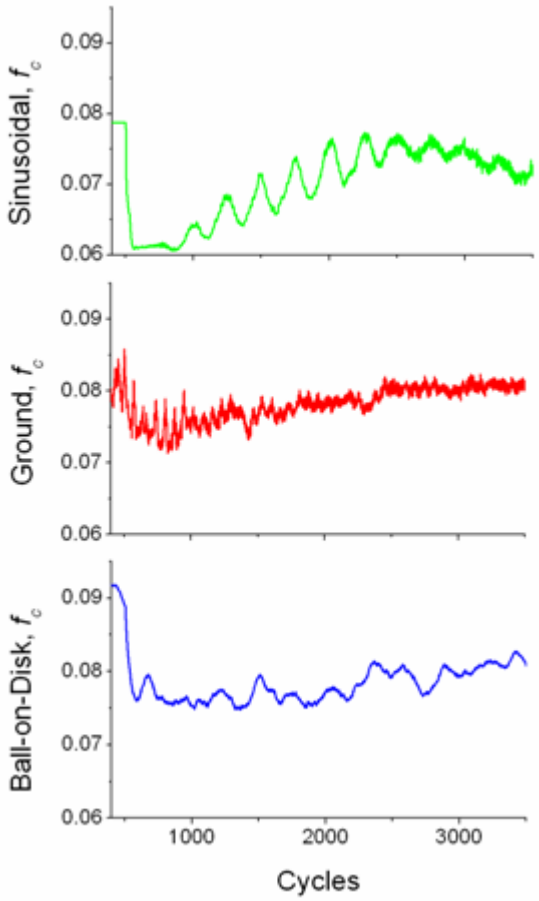

Figure 6.4.2-10: Friction coefficients as a function of time after the introduction of wear (plots start at 500 cycles) for each simulated contact case.

In all three cases it is assumed that the contact friction coefficient is 0.1, which provides an upper limit of possible friction variation. It is observed that at the beginning where there is no wear yet, the friction coefficient is quite high, close to 0.1, due to severe asperity peak contacts. Then, there is a sharp decrease of the friction coefficient immediately after wear is introduced into the simulation. This corresponds to the running-in phase in which tall asperity peaks are worn away quickly and the surface undergoes mechanical polishing. After this initial drop off, the friction gradually goes up. This is consistent with similar trends observed experimentally in both dry and lubricated contacts. In analysis of experimental results, the increase of friction with sliding distance has been directly related to measured values of both real and apparent contact area.

The direct relationship between friction and contact can be seen through the correlation between the friction coefficient and the contact load ratio. This relationship is illustrated in **Figure 6.4.2-11** for the ball-on-disk case.

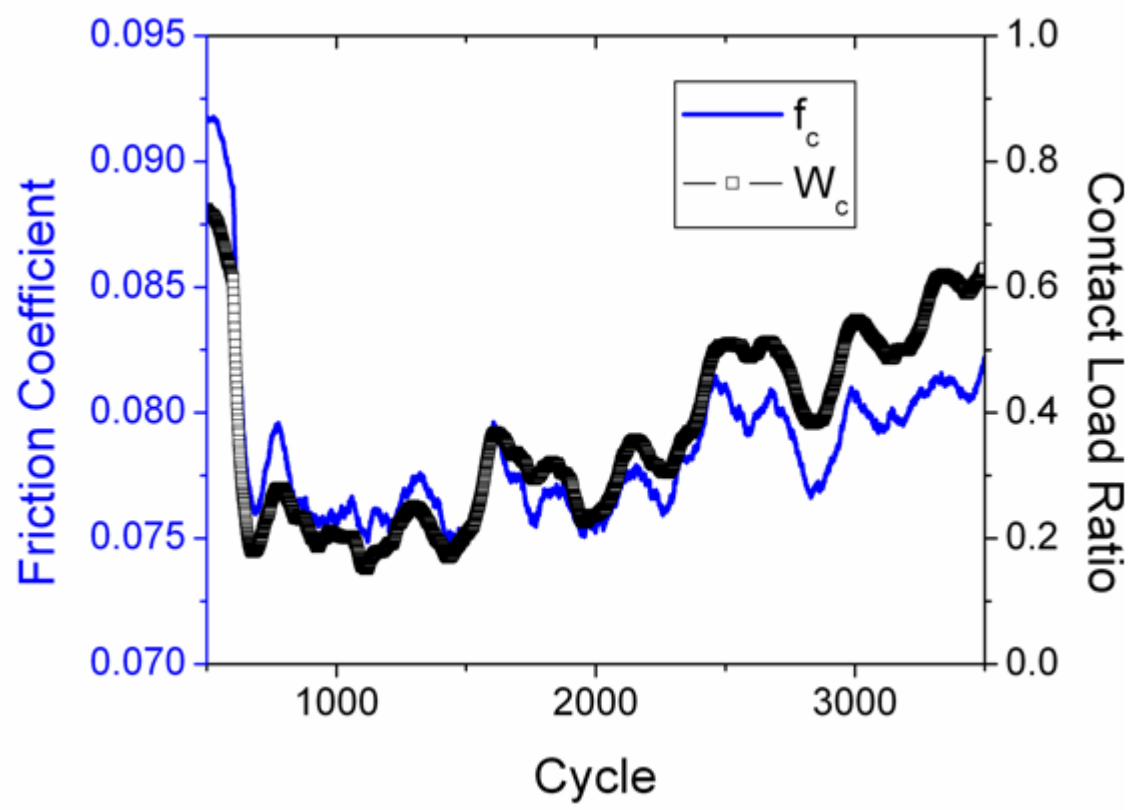

Figure 6.4.2-11: Friction coefficient (solid line) and contact load ratio (hollow squares) as functions of time for the ball-on-disk case illustrating the relationship between friction and contact area during the wear process.

The sharp decrease in friction observed during the running-in phase is consistent with a sharp decrease in the contact load ratio from approximately 0.7 to 0.3. Physically, this corresponds to a decrease in the percent of the load supported by contact locations (i.e. decreasing overall contact area). Then, the subsequent gradual increase in friction is concurrent with an increase in the contact load ratio. Here, the contact area is getting larger and the friction is increasing correspondingly. The other cases evaluated exhibited similar consistency between the contact load ratio and the friction coefficient.

Fatigue Crack Initiation – Background (Mura's theory on crack initiation)

The initiation of fatigue cracks is a complicated process involving various micromechanical interactions among dislocations, grains, and intrinsic resistance force. Before they nucleate into macrocracks, the fatigue cracks primarily develop in the patterns of shear cracks that find the easiest way to propagate. The site of crack initiation varies depending on both the microstructure and the stress state of the material under investigation. A large number of metallographic observations have indicated that localized cyclic deformation in persistent slip bands (PSBs) is

an important mechanism of fatigue crack initiation in many materials. The cyclic strain is concentrated along the PSBs and the plastic deformation ratchets up under a cyclic loading. To explain this phenomenon, Mura and his collaborators [Mura, 1991; Tanaka and Mura, 1981] modeled the forward and reverse plastic flow within PSBs as dislocation pile-ups of different signs in two adjacent layers, as shown in **Figure 6.4.2-12.** The fundamentals of the dislocation dipoles model agree with the observations made by Forsyth [1953], who found that there exist two closely spaced slip planes with one accommodating the plastic deformation during the forward loading and the other being associated with the reversed loading, respectively.

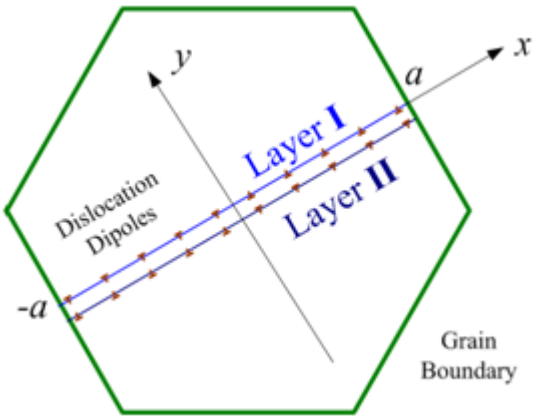

Figure 6.4.2-12: Mura's model for crack initiation within the grain

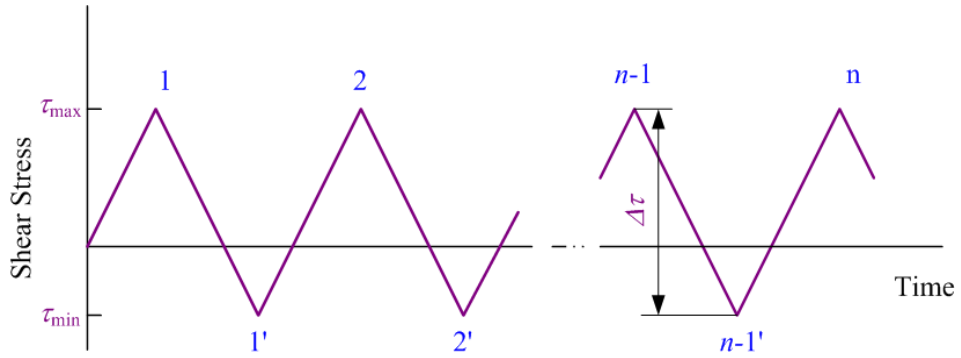

Figure 6.4.2-13: Applied shear stress pattern

Consider the cyclic shear stress pattern in a most favorably oriented grain as shown in **Figure 6.4.2-13**, where $\Delta\tau = \tau_{\max} - \tau_{\min}$ is the amplitude of the applied shear stress. During the forward loading, the dislocations are piled up on layer I and are assumed to be completely irreversible upon unloading, which however contributes only to the dislocations with opposite signs on layer II. In order to initiate the plastic flow on layers I, the applied stress, τ_{max}, is required to be greater than the intrinsic frictional stress, k, which is a material constant. In the first forward loading, dislocations are piled up at layer I in Fig. 3, satisfying the equilibrium equation

$$\tau_1^D + \tau_{\max} - k = 0 \qquad (50)$$

where τ_1^D is the stress caused by the distributed dislocation on layer I at loading point 1. When the slip plane [–*a*, *a*] is located away from the free surface of a homogeneous medium, the dislocation stress, τ_1^D, is obtained from the dislocation density, $D_1(x)$, as

$$\tau_1^D = \frac{\mu b}{2\pi(1-\nu)} \int_{-a}^{a} \frac{D_1(\xi)}{x-\xi} d\xi \tag{51}$$

where *b* is the magnitude of the Burgers vector, ν the Poisson's ratio and μ the shear modulus. The dislocation density function is solved from Eqs. (50) and (51) as

$$D_1(x) = \frac{2(1-\nu)(\tau_{\max} - k)x}{\mu b\sqrt{a^2 - x^2}} \tag{52}$$

The plastic strain, γ_1, caused by the above distribution of dislocations is

$$\gamma_1 = b\int_{-a}^{a} xD_1(x)dx = \frac{\pi(1-\nu)}{\mu}(\tau_{\max} - k)a^2 \tag{53}$$

and the stored energy per unit thickness, ΔU_1, due to the accumulated dislocation is

$$\Delta U_1 = -\frac{1}{2}\int_{-a}^{a} \tau_1^D b D_1(x)xdx = \frac{1}{2}\gamma_1(\tau_{\max} - k) \tag{54}$$

During the reverse unloading at point 1' of **Figure 6.4.2-13**, the similar computations are carried out on layer II:

$$\begin{aligned} D_{1'}(x) &= -\frac{2(1-\nu)(\Delta\tau - 2k)x}{\mu b\sqrt{a^2 - x^2}} = -\Delta D(x) \\ \gamma_{1'} &= -\frac{\pi(1-\nu)}{\mu}(\Delta\tau - 2k)a^2 = -\Delta\gamma \\ \Delta U_{1'} &= -\frac{1}{2}\gamma_{1'}(\Delta\tau - 2k) = \Delta U \end{aligned} \tag{55}$$

The results for the subsequent *j*-th loading cycle are obtained as follows:

the increment of dislocation:
$$\begin{cases} D_j(x) = \Delta D(x) & \text{on layer I} \\ D_{j'}(x) = -\Delta D(x) & \text{on layer II} \end{cases} \tag{56}$$

the increment of plastic strain:
$$\begin{cases} \gamma_j = \Delta\gamma & \text{on layer I} \\ \gamma_{j'} = -\Delta\gamma & \text{on layer II} \end{cases} \tag{57}$$

the stored energy:
$$\begin{cases} U_j = \Delta U & \text{on layer I} \\ U_{j'} = \Delta U & \text{on layer II} \end{cases} \tag{58}$$

The above results give quantitative evaluation of the accumulative plastic strain caused by the cyclic loading during the progress of the ratcheting in the slip band.

It is understood that when the slip plane is located near an interface, the exact expression for Eq. (51) becomes more complicated due to the effect of the image force. Except for very few cases, the closed-form solutions usually do not exist for the dislocation density functions. Consequently, solutions to Eqs. (50) and (51) have to resort to some type of numerical approach,

and the resulting plastic strain and the stored energy need to be evaluated by certain numerical quadrature.

Numerical approach

The general expressions for the stress field caused in a bi-material composite due to a dislocation may be very lengthy. For an edge dislocation located outside a circular inclusion, Dundurs and Mura [1964] have obtained a closed-form solution, which may be presented in a matrix form:

$$\begin{bmatrix} \sigma_{xx} \\ \sigma_{yy} \\ \sigma_{xy} \end{bmatrix} = \frac{2\mu_1}{\pi(\kappa_1+1)} \begin{bmatrix} G_{xxx} & G_{yxx} \\ G_{xyy} & G_{yyy} \\ G_{xxy} & G_{yxy} \end{bmatrix} \begin{bmatrix} b_x \\ b_y \end{bmatrix} \tag{59}$$

where b_x and b_y are the *x, y* components of the Burgers' vector, the Kolosov's constant $\kappa_1 = 3-4\nu_1$ for plane strain, ν_1 and μ_1 are Poisson's ratio and the shear modulus of the matrix, respectively. The detailed expression for the dislocation functions G_{ijk} can be found in [Hill et al., 1996]. Note that the solution with respect to a free surface [Jin and Keer, 2006] is a special case of Eq. (55).

Following a formulation procedure proposed by Jin and Keer [2006], the resultant governing equation may be represented in nondimensional form with -1 and +1 corresponding to the left and right crack tip, respectively:

$$\frac{1}{\pi}\int_{-1}^{1}\frac{\varphi(t)}{t-x}dt + \int_{-1}^{1}K(x,t)\varphi(t)dt = f(x), \quad (-1<x<1) \tag{60}$$

where the unknown function, $\varphi(x)$ is related to the normalized dislocation density function, the kernel, $K(x,t)$, though may be complicated in form, is a smooth and continuous algebraic function, and the known term, $f(x)$, stems from the applied external stress and the intrinsic frictional resistance.

The governing equation (56) may be solved numerically by employing the numerical scheme developed by Erdogan and Gupta [1972], which yields discrete function values at the integration points. The resulting stored elastic energy is then evaluated from the known information of the dislocation density by implementing numerical quadrature.

Fatigue Crack Initiation – Result

Effects of the free surface

The first example is used to benchmark the present numerical approach, assuming the inclination angle of the slip plane is $\theta = 45^0$, see **Figure 6.4.2-14**. The current results of the normalized dislocation density, **Figure 6.4.2-15**, show reasonable well agreement with the published results [Venkataraman et al., 1990]. The numerical results indicate a singular distribution of dislocation density at the right tip of the crack.

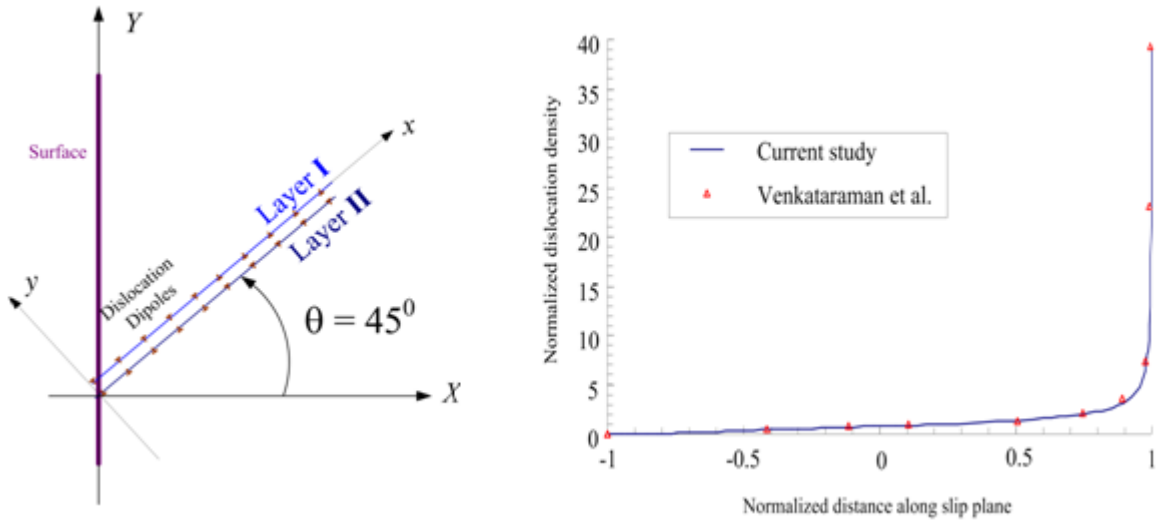

Figure 6.4.2-14 and 6.4.2-15: Inclined slip plane emanating from the free surface with θ = 45^0 and Benchmark of the normalized dislocation density for $\theta = 45^0$

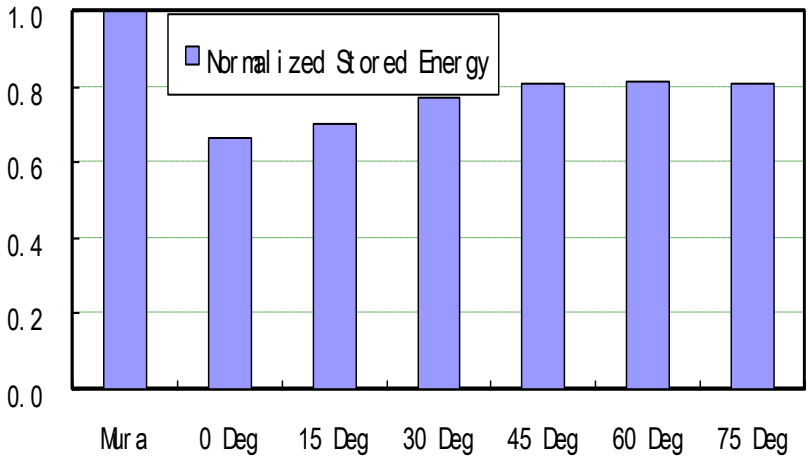

Figure 6.4.2-16: Comparison of stored energy for various inclination angles

The results of the stored elastic energy for various inclination angles θ are presented in **Figure 6.4.2-16**. The values are normalized by Mura's solution of Eq. (54), which is marked as unity in **Figure 6.4.2-17.** It is seen that when the inclination angle turns to around 45^0, the stored energy attains its maximum value, which indicates a most favorable pattern for the fatigue crack initiating from the free surface.

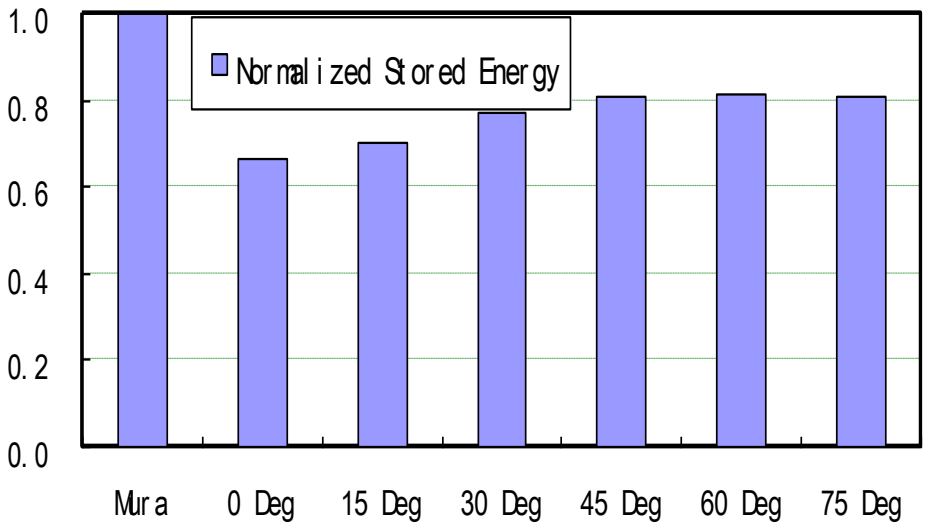

Figure 6.4.2-17: Comparison of stored energy for various inclination angles

Effects of the circular inclusion

In order to study the influence of the inclusion on the initiation of the fatigue crack, the slip plane is arranged in the radial direction, **Figure 6.4.2-18**. Numerical results for a hard inclusion are shown in **Figure 6.4.2-19**. The stored energy is smaller as the slip plane becomes closer to the inclusion. In contrast, when the inclusion is replaced by a void, the maximum stored energy appears to be located close to the circular hole, **Figure 6.4.2-20**, which indicates a possible mechanism for initiation of fatigue cracks from the void.

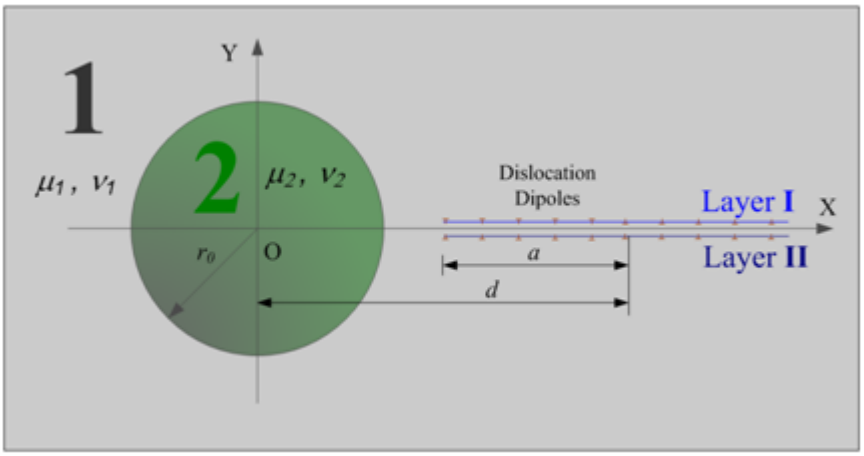

Figure 6.4.2-18: The dislocation dipoles are aligned along the radial direction

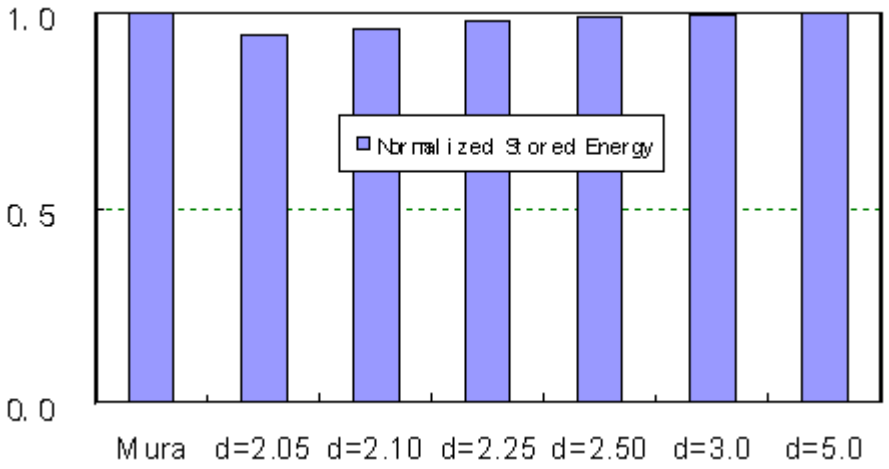

Figure 6.4.2-19: Numerical results for α=1.4, β=0

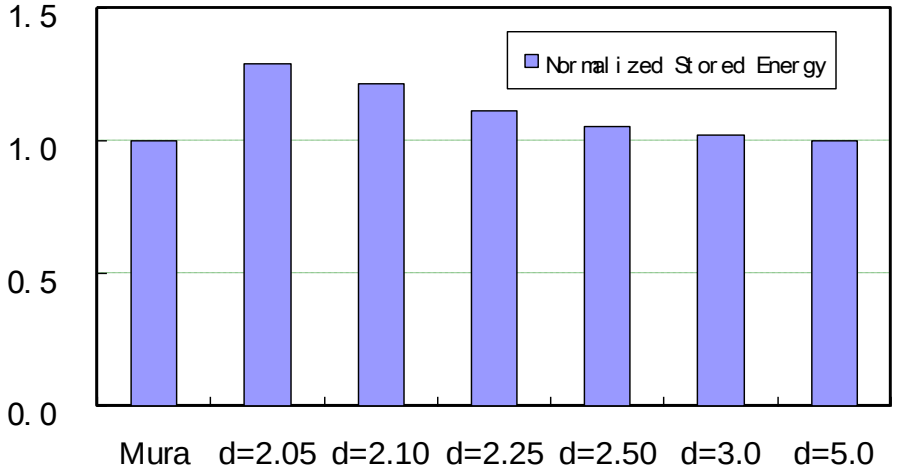

Figure 6.4.2-20: Numerical results for circular hole

Friction - Background

Interaction between the ball and the half-space induces normal pressure p and shear tractions q_x and q_y along the z, x, and y axes, respectively. The general contact model [Johnson, 1985] is repeated here for clarity,

$$h(x,y) = h_i(x,y) + u_z(x,y) - \delta_z$$
$$s_x(x,y) = u_x(x,y) - \delta_x, \qquad s_y(x,y) = u_y(x,y) - \delta_y \tag{65}$$

Here, δ_x, δ_y and δ_z are the rigid-body approaches along three axes respectively, s_x and s_y the relative slip along the x and y axes, u_x, u_y, and u_z three displacement components, h_i is the initial surface clearance, and h the surface gap after loading. It should be pointed out that the tractions applied on the corresponding points on two surfaces are the same in magnitude but opposite in direction. Based on the Boussinesq-Cerruti integral equations [Johnson, 1985], the relative

surface displacements at any point (x, y) can be formulated in terms of the tractions over the contact area as follows,

$$
\begin{aligned}
u_x(x,y) = \int_{-\infty}^{+\infty}\int_{-\infty}^{+\infty}\Bigg\{ & \frac{1}{\pi\rho^3}\left[\frac{(x-\xi)^2}{E'}+\frac{(y-\eta)^2}{E^*}\right]\cdot q_x(\xi,\eta) \\
& +\frac{(x-\xi)(y-\eta)}{\pi\rho^3\mu^*}\cdot q_y(\xi,\eta)-\frac{x-\xi}{\pi\rho^2\mu'^2}\cdot p(\xi,\eta)\Bigg\}d\xi d\eta \\
u_y(x,y) = \int_{-\infty}^{+\infty}\int_{-\infty}^{+\infty}\Bigg\{ & \frac{(x-\xi)(y-\eta)}{\pi\rho^3\mu^*}\cdot q_x(\xi,\eta) \\
& +\frac{1}{\pi\rho^3}\left[\frac{(x-\xi)^2}{E^*}+\frac{(y-\eta)^2}{E'}\right]\cdot q_y(\xi,\eta)-\frac{y-\eta}{\pi\rho^2\mu'^2}\cdot p(\xi,\eta)\Bigg\}d\xi d\eta \\
u_z(x,y) = \int_{-\infty}^{+\infty}\int_{-\infty}^{+\infty}\Bigg\{ & \frac{x-\xi}{\pi\rho^2\mu'}\cdot q_x(\xi,\eta)+\frac{y-\eta}{\pi\rho^2\mu'}\cdot q_y(\xi,\eta) \\
& +\frac{1}{\pi\rho E^*}\cdot p(\xi,\eta)\Bigg\}d\xi d\eta
\end{aligned}
\qquad (66)
$$

where $\rho=\sqrt{(x-\xi)^2+(y-\eta)^2}$, $1/E'=(1+\nu_1)/E_1+(1+\nu_2)/E_2$,
$1/E^*=(1-\nu_1^2)/E_1+(1-\nu_2^2)/E_2$, $1/\mu'=$ [illegible] , and $1/\mu^*=$ [illegible] . (67)

In order to conduct numerical analyses, the potential contact area is discretized by a rectangular mesh system with $M\times N$ elements, each of which is $2\Delta_1\times 2\Delta_2$ in size. Displacement solutions of uniform tractions over the element at the origin (influence coefficients) are derived. The influence coefficient, $D^{ij}_{[\alpha,\beta]}$, is the displacement, u_i, at the point of ($2\alpha\Delta_1$, $2\beta\Delta_2$) caused by traction q_j. Here, $i, j = x, y, z$, and $q_z = p$. For instance, the influence coefficients of normal displacement u_z induced by normal pressure p is,

$$
D^{zz}_{[\alpha,\beta]} = \int_{-\Delta_1}^{\Delta_1}\int_{-\Delta_2}^{\Delta_2} G_{zz}(2\alpha\Delta_1-\xi,2\beta\Delta_2-\eta)d\xi d\eta \qquad (68)
$$

where $G_{zz}(x,y)=1/\pi E^*\sqrt{x^2+y^2}$. The normal displacement can then be written in a discrete convolution,

$$
u_{z[\alpha,\beta]} = \sum_{\chi=0}^{M-1}\sum_{\psi=0}^{N-1}\left(q_{x[\chi,\psi]}D^{zx}_{[\alpha-\chi,\beta-\psi]}+q_{y[\chi,\psi]}D^{zy}_{[\alpha-\chi,\beta-\psi]}+p_{[\chi,\psi]}D^{zz}_{[\alpha-\chi,\beta-\psi]}\right) \qquad (69)
$$

Equations of the tangential displacements can be obtained in a similar way.

$\underline{u}_a=\underline{\underline{D}}^{ab}\cdot\underline{q}_b=\sum_{\chi=0}^{M-1}\sum_{\psi=0}^{N-1}D^{ab}_{[\alpha-\chi,\beta-\psi]}q_{b[\chi,\psi]}$ can be used to represent the basic discrete convolutions.

Here, $\underline{\underline{D}}^{ab}$ is the influence coefficient matrix, and the symbols with single underline are vectors

containing $M \times N$ values of corresponding variables at all elements. Consequently, the contact model shown in Eq. (1) can be rearranged to,

$$\begin{bmatrix} \underline{\underline{D}}^{xx} & \underline{\underline{D}}^{xy} & \underline{\underline{D}}^{xz} \\ \underline{\underline{D}}^{yx} & \underline{\underline{D}}^{yy} & \underline{\underline{D}}^{yz} \\ \underline{\underline{D}}^{yy} & \underline{\underline{D}}^{yy} & \underline{\underline{D}}^{yy} \end{bmatrix} \begin{bmatrix} \underline{q}_x \\ \underline{q}_y \\ \underline{p} \end{bmatrix} - \begin{bmatrix} \underline{\delta}_x \\ \underline{\delta}_y \\ \underline{\delta}_z \end{bmatrix} = \begin{bmatrix} \underline{s}_x \\ \underline{s}_y \\ \underline{h} - \underline{h}_i \end{bmatrix} \tag{70}$$

The contact problem is subjected to the following boundary conditions and constraints:

1) On the contact area, A_c, contact pressure p is larger than zero and less than the local normal strength, p_m, and the surface gap, h, vanishes. However outside the contact area, contact pressure has to be zero, and the surface gap is larger than zero.

$$\begin{aligned} &h = 0, \quad 0 < p \le p_m && \subset A_c \\ &h > 0, \quad p = 0 && \not\subset A_c \end{aligned} \tag{71}$$

2) The shear stress is less than the local shear strength, τ_m, which can be related to the local normal strength, p_m, and hardness of the softer material, H

$$p_m^2 + \alpha \tau_m^2 = H^2 \tag{72}$$

Here, H is roughly $2.8\sigma_Y$ for elastic perfectly-plastic materials, σ_Y the uniaxial yield strength, and α the Tabor constant. Here, we estimate the Tabor constant as follows. When two clear surfaces are adhered together under high vacuum conditions with contact pressure much less than the shear traction, the local shear strength approaches the bulk shear strength of the softer material, k_s ($\approx \sigma_Y / \sqrt{3}$). Therefore, the Tabor constant, α, approximately equals $(H/k_s)^2 \approx 23.52$. This value of the Tabor constant should be valid for cases with light load and small roughness because it is estimated with the relatively small normal pressure and the carefully cleaned surface (strong adhesion). However, the applicability of this value will be validated via comparing the numerical results with the experimental measurements in [Etsion, 2005].

3) The contact area is composed by the stick and slip zones. In the stick zone, A_{st}, the relative slip magnitude, $|s|$, is zero; the shear stress magnitude, $|q|$, is less than the local shear strength, τ_m. In the slip zone, A_{sl}, $|q|$ reaches the local shear strength, τ_m; and the relative micro slip happens between contact points ($|s| > 0$).

4)

$$\begin{aligned} &|q| = \sqrt{q_x^2 + q_y^2} < \tau_m, \quad |s| = \sqrt{s_x^2 + s_y^2} = 0 && \subset A_{st} \\ &|q| = \sqrt{q_x^2 + q_y^2} = \tau_m, \quad |s| = \sqrt{s_x^2 + s_y^2} > 0 && \subset A_{sl} \end{aligned} \tag{73}$$

Without losing generality, the procedure to evaluate the static friction force along the x axis is described below. First, the normal contact situation of the ball (shown in Fig. 1) with the half-

space is simulated ($\delta_x = \delta_y = 0$). The tangential approach, δ_x, is gradually increased, and the tangential force, F_x, in the x direction can be obtained by integrating the shear traction q_x over the entire contact area.

$$F_x = \Delta_1 \Delta_2 \sum q_x \qquad (74)$$

The static friction force is the maximum tangential force that the normal contact can support at sliding inception. In this paper, sliding inception is assumed to happen at the moment when the stick area, A_{st}, drops to zero. Finally, the static friction coefficient, μ_f, is determined by the static friction divided by the pre-applied normal load.

$$\mu_f = F_x / P \qquad (75)$$

Friction - Result

The comparison between the variation of the dimensionless static friction as a function of the dimensionless normal load measured in the experiment and those predicted by the present model, as well as those from the Kogut-Etsion friction model (or the KE model) [Kogut and Etsion, 2003], is shown in **Figure 6.4.2-21**. In order to incorporate the effects of material hardness and sphere radius, both the normal load and the static friction are normalized by P_c. The present model gives a better prediction on the static friction force than the KE model in the investigated load range of $P/P_c < 14$. Both the present model and the KE model overestimate the static friction under lower normal loads, $P/P_c < 6$. In addition, The KE model suggests that the static friction would vanish when the plastically deformed zone first reaches the surface (roughly at $P/P_c = 14$). Such a zero friction is in disagreement with the experimental results. Moreover, the static friction force measured from the copper-on-steel test is higher than that from the copper-on-sapphire test within the load range of $P/P_c < 14$, which was not shown in the KE model. The analysis of the present model not only demonstrates an improved agreement with the experimental friction trend as a function of normal load, but also predicts the friction discrepancy of the two material combinations.

Effect of Different Material Combinations

The static friction coefficients for a spherical contact involving copper balls are analyzed for three different material combinations: Copper and copper ($\beta = 0$), copper and steel ($\beta = 0.072$), and copper and sapphire ($\beta = 0.146$). Larger material difference leads to a larger value of β. The softer material, which is copper in all these cases, has a hardness of H = 1GPa. All material properties can be found in **Table 6.1.2-1**. The half-space has a rough surface of R_q = 0.04um and λ = 40um.

Figure 6.4.2-22 shows the profiles of static friction coefficient versus dimensionless normal load for the four material combinations. The static friction coefficient decreases exponentially as the normal load increases, which is consistent with the experimental observations. The comparison indicates that the static friction coefficient is smaller when the property dissimilarity of materials in contact is larger. For the contact of materials with larger property discrepancy or higher Dunders constant β, the shear traction induced by the normal pressure is larger; and the junctions of contact asperities are weaker and easier to be sheared. This point agrees well with the tribological practice of using dissimilar materials in a contact pair for low friction.

Effect of Surface Roughness

A group of rough surfaces with different RMS roughness values is generated by means of the digital filtration algorithm. The present model is used to evaluate the static friction coefficient for the contacts of a smooth copper ball against these rough surfaces of sapphire in order to investigate the effect of surface roughness.

Variations of the static friction coefficient as a function of the dimensionless normal load for different surface roughness values (R_q = 0.02, 0.06, and 0.12 um) are presented in **Figure 6.4.2-23**, which reveals that the static friction coefficient is lower for the contact with rougher surfaces when the roughness is in the studied range without asperity interlocking.

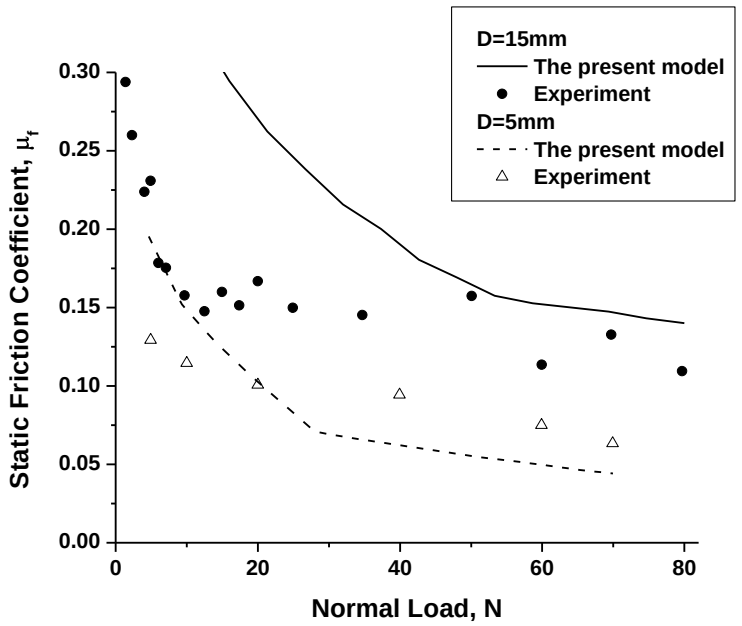

(a)

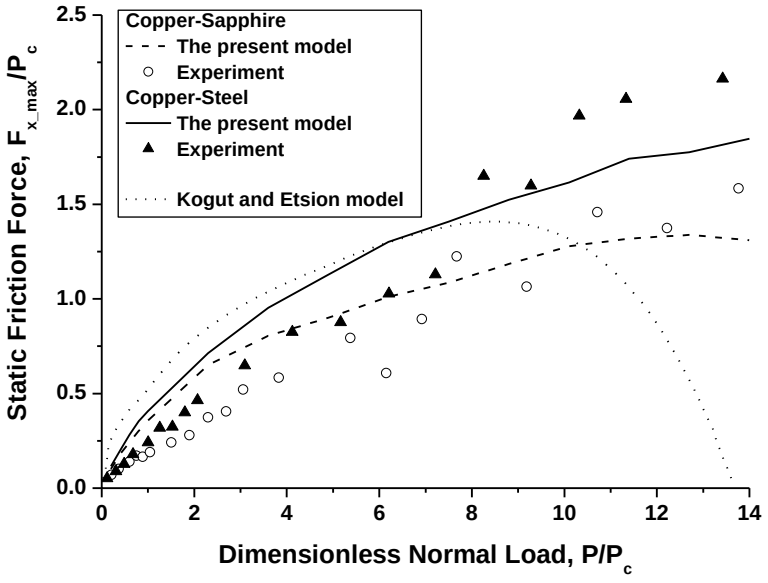

(b)

Figure 6.4.2-21: Model validations through comparison with the experimental results in [Etsion et al., 2005], (a) the static friction coefficient versus dimensionless normal load for copper on sapphire, and (b) maximum tangential force (static friction force) versus dimensionless normal load for copper on sapphire and copper on steel.

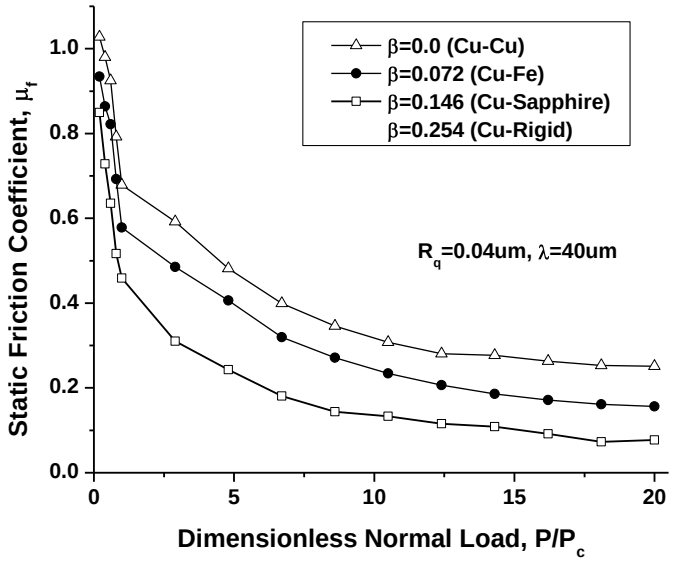

Figure 6.4.2-22: Comparison of static friction coefficient variations as a function of the dimensionless normal load for the contacts of the copper ball on the rough half-space of different materials.

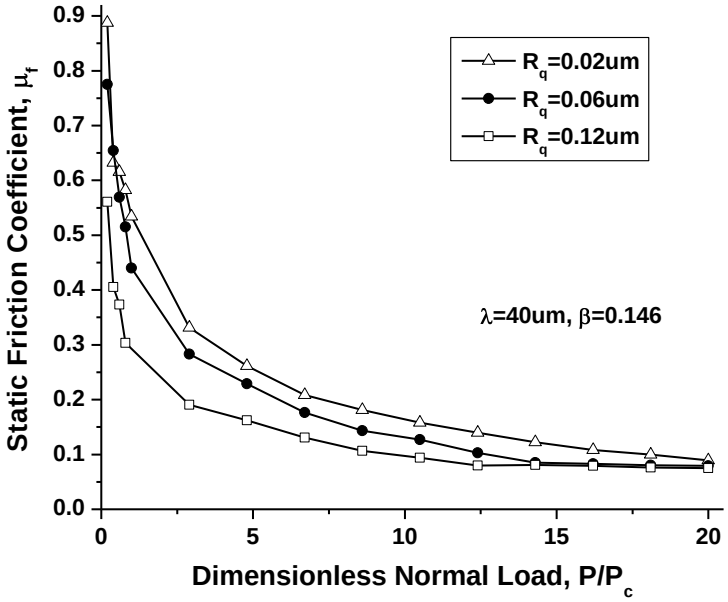

Figure 6.4.2-23: Effects of surface RMS roughness, R_q, on static friction coefficient for the copper ball on the sapphire half-space.

6.4.3 Process Techniques to Overcome Difficulties with Gear Geometry Effect and Temperature Effects

Challenges with Gear Coatings

A number of challenges have been identified that hamper the PVD (physical vapor deposition) coating of gears. These challenges affect the cleanliness of the gears prior to coating. They affect the thickness and adhesion of the coating. They affect the durability of the coating and also the practicality of coating gears. Among these challenges are gear geometry, the limited temperature processing, the surface finish requirement and the cost.

Gear geometry

Gear geometry presents the greatest challenge limiting the PVD coating of gears. Gear geometry itself influences gear cleanliness, coating thickness, adhesion and durability. While coarse gear teeth profiles shown in **Figure 6.4.3-1a** are somewhat easier to coat, the industrial trend is to move toward the finer pitched gears shown in **Figure 6.4.3-1b.** The gear tooth profile and the involute profile restricts both the mechanical access and access of electrical charges to the lower flank and root of the gear tooth.

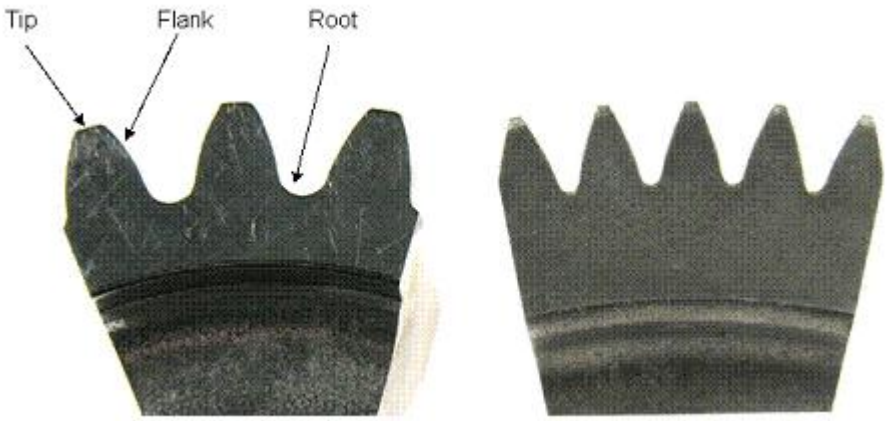

a b

Figure 6.4.3-1ab: Coarse pitch gear (left), processed in Batch 1063 with PVD CrWC coating, is compared to finer pitch gear processed in Batch 1137 with AlMgB14-TiB2-C coating.

Prior to PVD coating the gears must be super finished mechanically. The proprietary super finishing process used by REM tumbles the work pieces in a ceramic media that also contains a fruity acid. The combination of a mild mechanical and chemical attack removes asperities from the work piece surface. While this is an excellent process, it can be limited by gear geometry. For tumbling to be successful, the media must contact all the work piece surfaces. For fine pitched gears, the size of the tumbling media may prevent the media from getting to the gear root. Finer tumbling media must be selected or a mixed media approach that includes coarser as well as very fine media must be used. The consequence of not getting adequate super finishing of the gear tooth lower flank and root is poor adhesion. The coating will spall off easily when subjected to high contact stress.

Gear geometry also prevents the electrical field of the RF (radio frequency) cleaning plasma from getting to the gear tooth root. The tip of a gear tooth in comparison to the root is a high electric field concentrator. As a result, during RF etching and coating deposition, the charged species are attracted more to the tip than to the root. This has two major side effects:

1. RF etching becomes ineffective at the root
2. Non-uniform coating thickness from the tip to the root of the gear tooth.

Eaton performed a study on gear sections to evaluate the thickness and adhesion of PVD coatings at various locations of the gear tooth profile. A comparison is made between work with a Chromium-Tungsten-Carbon (CrWC) coating (Batch 1063) and new Aluminum Magnesium-Boride-Titanium DiBoride-Carbon (AlMgB14-TiB2-C) coating (Batch 1137). F**igure 6.4.3-1a** illustrates the geometric differences in the gears processed under Batches 1063 and 1137, respectively. The CrWC coating, Batch 1063, was applied to a coarse pitch gear. The AlMgB coating, Batch 1137, **Figure 6.4.3-1b** was deposited on a much finer pitch gear. This finer pitch gear is typical of the transmission components used for Eaton's "Best Tech 1" transmission.

Figure 6.4.3-2 presents micrographs from the coarse pitch gear PVD coated with Chromium-Tungsten-Carbon (CrWC) in Batch 1063. The left side micrograph (a) displays a uniform coating having a thickness of 3.05 microns (micrometers). A short distance away on the tooth flank (b), the coating thickness has decreased about 48 percent to 1.60 microns. At the root (c) the thickness at 1.62 microns has decreased 47 percent from the thickness at the tip. The coating also shows disbond. These results are unacceptable.

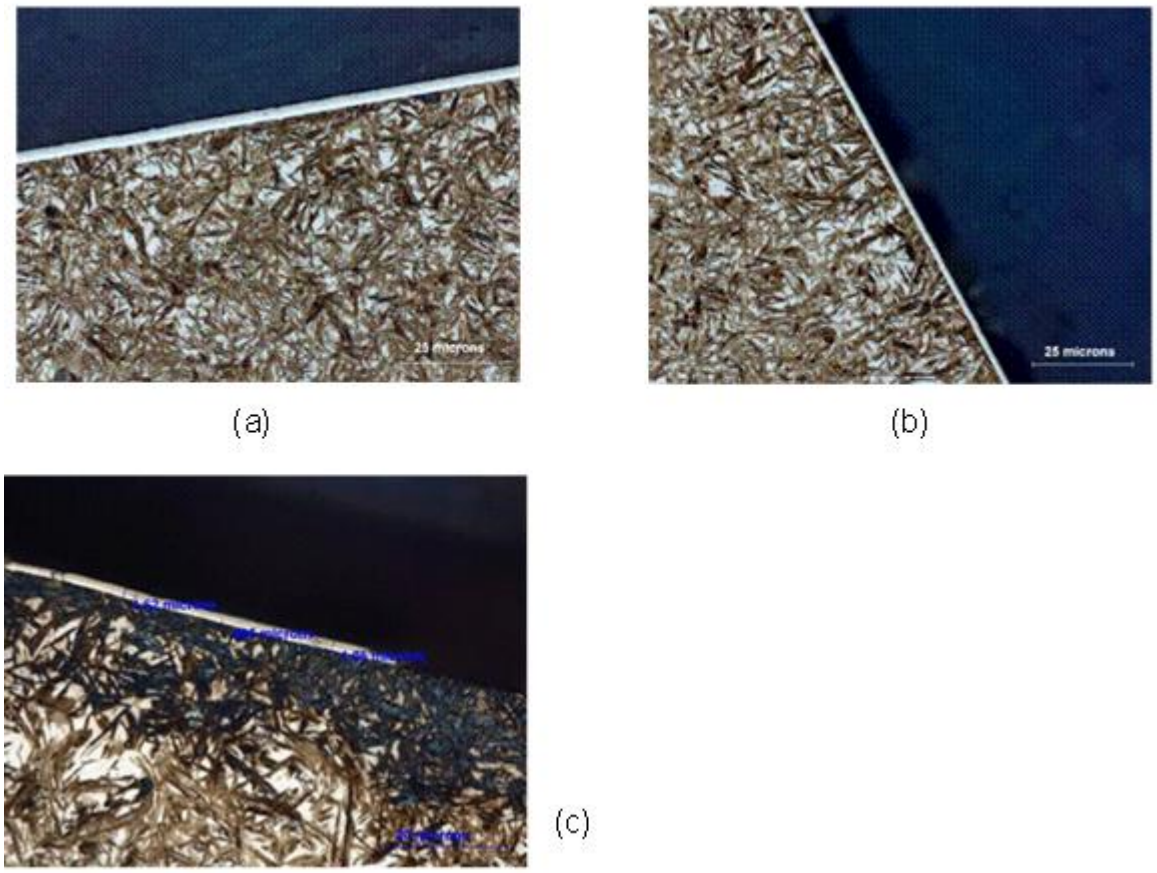

Figure 6.4.3-2: Micrographs of PVD CrWC coated gear tooth: (a) Batch 1063, tooth tip, 3.05 microns, 1000x; (b) Batch 1063, tooth flank, ~1.6 microns, 1000x.; (c) Batch 1063 root. 1.62 microns, disbond, 1500x.

In **Figure 6.4.3-3** a thicker PVD coating of Aluminum Magnesium Boride-Titanium DiBoride-Carbon (AlMgB14-TiB2-C) is evident on the finer pitch gear tooth. At the tooth tip a thickness of 3.72 microns has been obtained. A short distance away at the flank, the coating thickness is 27 percent less, reaching 2.72 microns. Halfway down the tooth flank, the thickness has dropped to 1.78 microns, 52 percent of the thickness at the tooth tip. At the root of the **Figure 6.4.3-3** gear tooth, coating thickness was 61 percent less than the thickness at the tooth tip. More troublesome, however, is the fact that the coating delaminated due to forces experienced while the metallographic sample was being mounted. This unfortunate result pinpoints the difficulty in getting sufficient cleaning at the root. A thick, highly adherent coating may not be absolutely necessary at the root but good coating thickness and adherence should extend at least halfway down the dedendum or more. In discussion with the PVD operator who coated the gear shown in **Figure 6.4.3-3**, the possibility that the particular gear section was not shot cleaned adequately could have contributed to the delamination. These results are not acceptable.

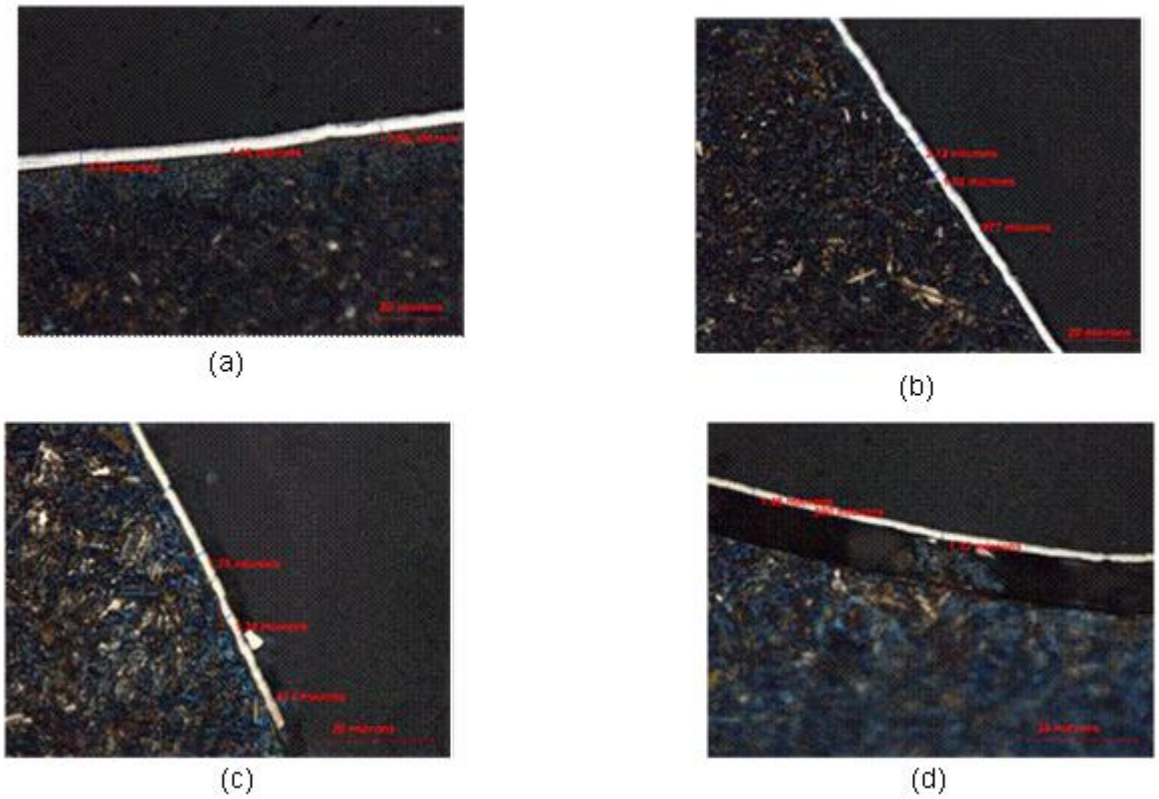

Figure 6.4.3-3: Micrographs of PVD Aluminum Magnesium Boride-Titanium DiBoride-Carbon (AlMgB14-TiB2-C) coated gear tooth: (a) Batch 1137, *tooth tip*, 3.72 microns, 1000x; (b) Batch 1137, *gear flank near tooth tip*, 2.72 microns, 1000x; (c) Batch 1137, *gear flank at half-tooth height*, 1.78 microns; (d) Batch 1137, at root of gear tooth, 1.46 microns, 1500x. Coating has delaminated from steel substrate of fine pitch.

The gear segment presented in **Figure 6.4.3-4** has a Chromium bond coat and a Tungsten Carbide-Carbon topcoat. At the tooth tip (a) the coating thickness measures 2.92 inch. Down in the root (b) the thickness of the coating is 2.62 inch, a decrease in thickness of only 10 percent; this is a good result. The coating retained an adequate thickness on the coarse pitch gear and showed good adhesion. While this result was good, the difference in the processing was very small. This inconsistency identifies uncontrolled variability in the PVD process that needs to be identified and addressed.

PVD technology breakthroughs will improve the coating of gears. The use of pulsed energy methods and alternative methods to RF cleaning will be investigated in the future.

(a) (b)

Figure 6.4.3-4: Micrographs of PVD Chromium/ Tungsten Carbide-Carbon (Cr/WC-C) coated gear tooth: (a) Batch 1062, *tooth tip*, 2.92 microns, 1500x; (b) Batch 1062, at *root* of gear tooth, 2.62 microns, 1500x. Coating has good adhesion at root of coarse pitch gear.

Limited Temperature Processing Due to Substrate

Most commonly used transmission gear materials are the 8600, 4100 and 4300 carbon steels. These materials typically are carburized and then tempered at 150 - 200ºC. This sets a limitation to PVD processing since the best adhesion results are achieved at processing temperatures around 350 to 500 ºC. PVD coating gears above 150ºC draws back the hardness of the carburized case that normally is 58 to 62 HRC. This hard carburized case provides an excellent supporting structure for the PVD coating. As the hardness of the carburized case decreases due to excessive PVD processing temperatures, the support for the extra hard PVD coating diminishes. The result is much like an unsupported hard eggshell. Despite the unfavorably low processing temperature, the PVD coating is expected to provide good adhesion. Lowering the PVD processing temperature is an opportunity for future technology development.

Surface Finish

The best adhesion of PVD coating is achieved on smooth surfaces with surface roughness of 0.05 to 0.10 micrometers (2 to 4 microinches). PVD coating coarser surfaces is possible but is not optimal. The PVD coating deposits with a thickness of 2 to 4 micrometer. PVD coatings follow the contour of large asperities. In service, as asperities break off, the coating is disrupted. Smooth surfaces are best.

Surface finishes used on transmission and axle gears today are improving and getting smoother. Among the different finishing methods are:

- Hobbed and shaved, about 45 microinches (1.14 micrometers)
- CBN grinding, about 22 microinches (0.56 micrometers)
- Honing, about 14 microinches (0.36 micrometers)
- Isotropic finishing (super finishing), about 2 to 4 microinches (0.05 to 0.10 micrometers)

There is a current trend in the industry to adopt super finishes (isotropic finish) 2-4 microinches for heavily loaded gears. As this occurs, surface finish may no longer be a limitation to implementing the PVD coating of gears.

Cost

Because of the dimensions and large surface area of gears, the number processed per PVD coating batch may be at best a few hundred. This limited quantity drives the cost to tens of dollars per gear. This is probably the biggest challenge to implementing the PVD coating of gears. However, a new trend in PVD machines is to transition from batch processing to continuous feed processing. This technology development can make gear coating practical.

6.4.4 Test Data to Support use of Coated Gears in Transmission Dynamometer Tests

Roller Contact Fatigue Tests

Eaton continued to examine PVD (physical vapor deposition) coatings for use on gears. Roller contact fatigue tests (RCFT) were conducted at a high level contact stress, 350 ksi. Eaton-internal PVD coatings and coatings from two external suppliers were tested. The performance of bare gear steel rollers was compared to the performance of the coated gears. PVD coatings tested included (1) Eaton Aluminum Magnesium Boride-Titanium DiBoride-Carbon (AlMgB-TiB-C), (2) Eaton Aluminum Magnesium Boride-Titanium DiBoride-solid lubricant (AlMgB-TiB-sl) and Diamond-Like Carbon (DLC) from two suppliers. Results of these RCFT are presented in **Figures 6.4.4-1 to 6.4.4-6.**

During the run-in period, bare gear steel produced an initial torque of 331 in-lbs at a load a 4,000 lbf. After 96 hours run time in Roadranger SAE 50 Revision 7 oil, the bare steel rollers showed a torque of 164 in-lbs at a similar 4,000 lb load. The 50 percent decrease in torque resulted from wear and polishing of the small roller, the spindle, **Figure 6.4.4-1.**

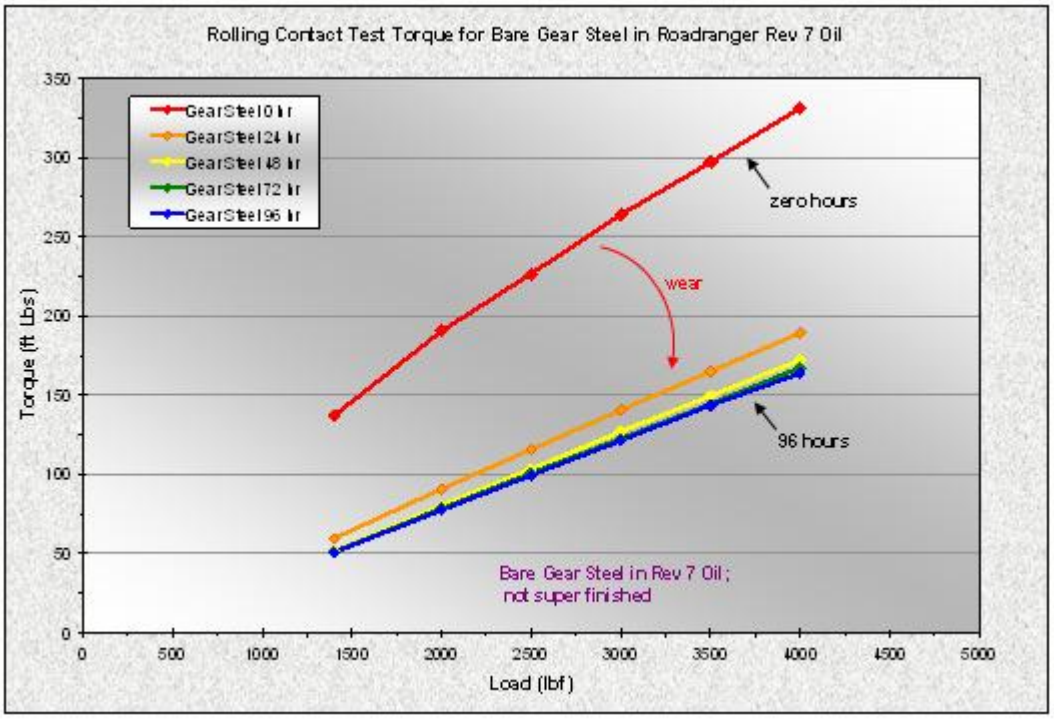

Figure 6.4.4-1: Roller contact fatigue test of bare steel in Roadranger Revision 7 oil. Steel wore and polished during testing, reducing the torque.

Super finished bare steel run in experimental, low friction oil TDN3 produced a very different result. From the start of the test at zero hours through the 96 hour duration, there was no wear of the rollers, see **Figure 6.4.4-2.** The torque remained constant at 111 inch-pounds, 66 percent lower than the starting point of ground bare steel in **Figure 6.4.4-1.**

Super finishing and a PVD coating of AlMgB-TiB-sl (solid lubricant) substantially reduced the initial torque to 140 in-lbs at 4,000 lbf, 58 percent lower initial torque than the bare steel. After 96 hours run time in Roadranger SAE 50 Revision 7 oil, the PVD coating stayed intact and the torque dropped to 120 in-lbs, **Figure 6.4.4-3.** Comparing the final torque for the bare steel (164 in-lbs) and the AlMgB-TiB-sl coating (120 in-lbs) reveals a 26 percent decrease in torque at 4,000 lbf. Also significant is the fact that the PVD coating survived 96 hours run time at a contact stress of 350 ksi. Previous RCFT of PVD coatings had generated coating failure at 48 hours run time.

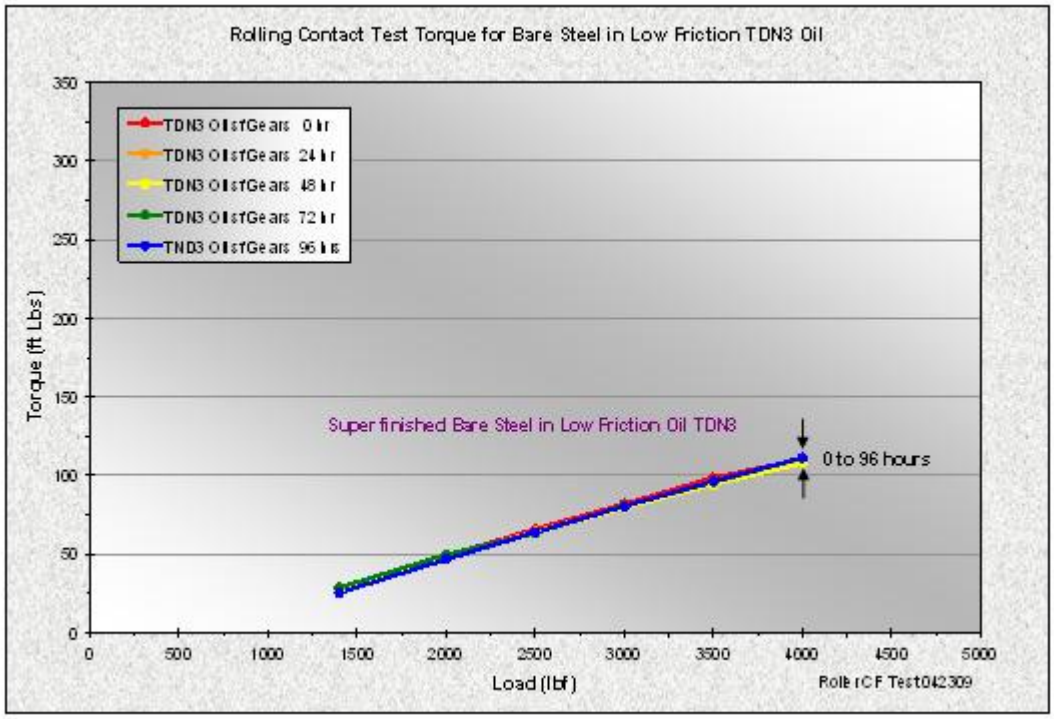

Figure 6.4.4-2: Roller contact fatigue test of super finished bare steel in low friction TDN3 oil. Wear was minimal with the torque remaining at 111 inch-pounds over the 96 hour test.

In **Figure 6.4.4-4** the AlMgB-TiB-C coating, also a solid lubricant-style coating, produced significant, additional reduction in torque. Initial torque at 4,000 lbf reached only 85 in-lbs. Super finishing and the AlMgB-TiB-C coating diminished initial torque by 74 percent. The AlMgB-TiB-C coating successfully completed the 96 hour test finishing with a final torque of 79 in-lbs. Comparing the final torque for the bare steel (164 in-lbs) and the AlMgB-TiB-C coating (82 in-lbs) reveals a 50 percent decrease in torque.

Supplier A provided Eaton a DLC coating. This DLC coating was testing in low friction TDN3 oil. This combination yielded a final torque of 80 in-lb, an impressive 51 percent reduction in final torque, see **Figure 6.4.4-5.** A second supplier also provided a DLC coating to Eaton, DLC2. While the DLC2 coating showed a similar, low initial torque, the coating stripped off 24 hours into the 96 hour test. A second test run on identical coated samples produced the same result.

Figure 6.4.4-6 summarizes the results of the roller contact fatigue tests. The combination of the PVD DLC coating and the low friction TDN3 oil resulted in an impressive 51 percent reduction in torque.

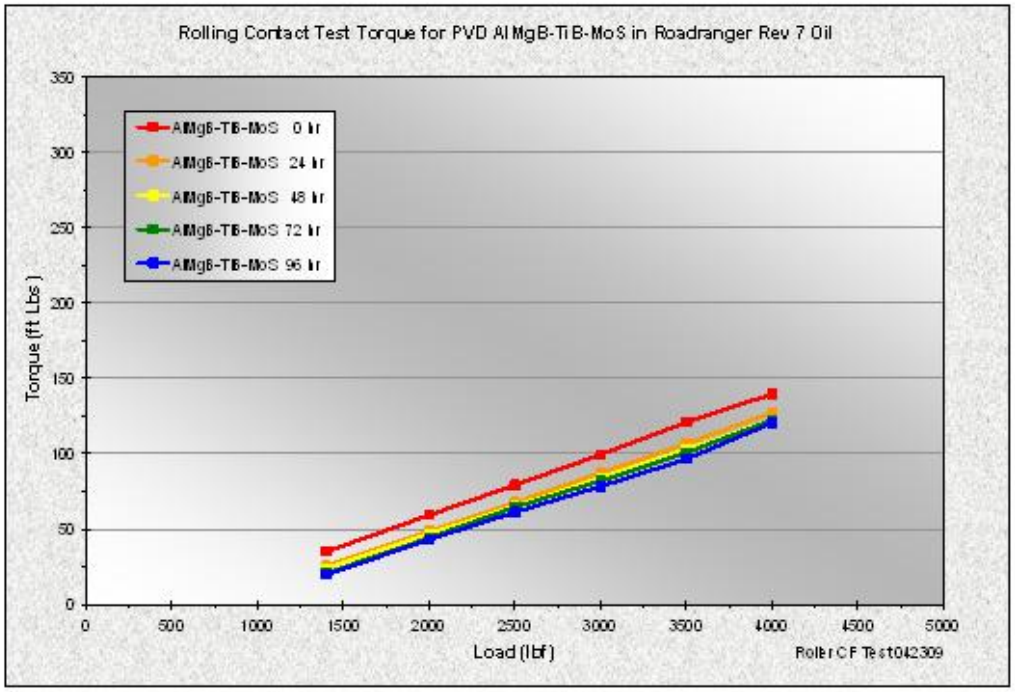

Figure 6.4.4-3: Roller contact fatigue test of super finished, PVD coated AlMgB-TiB-sl steel in Roadranger Revision 7 oil. Wear was minimal with the torque reducing from 140 to 120 inch-pounds over the 96 hour test.

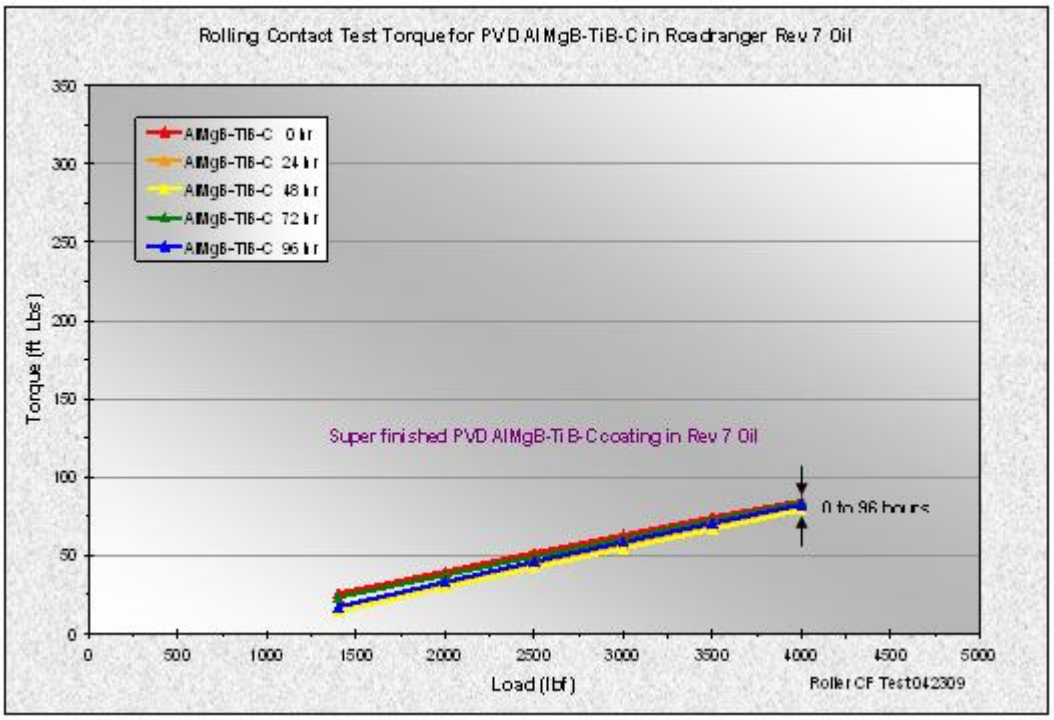

Figure 6.4.4-4: Roller contact fatigue test of super finished, PVD coated AlMgB-TiB-C steel in Roadranger Revision 7 oil. Wear was minimal with the torque remaining at 82 inch-pounds over the 96 hour test.

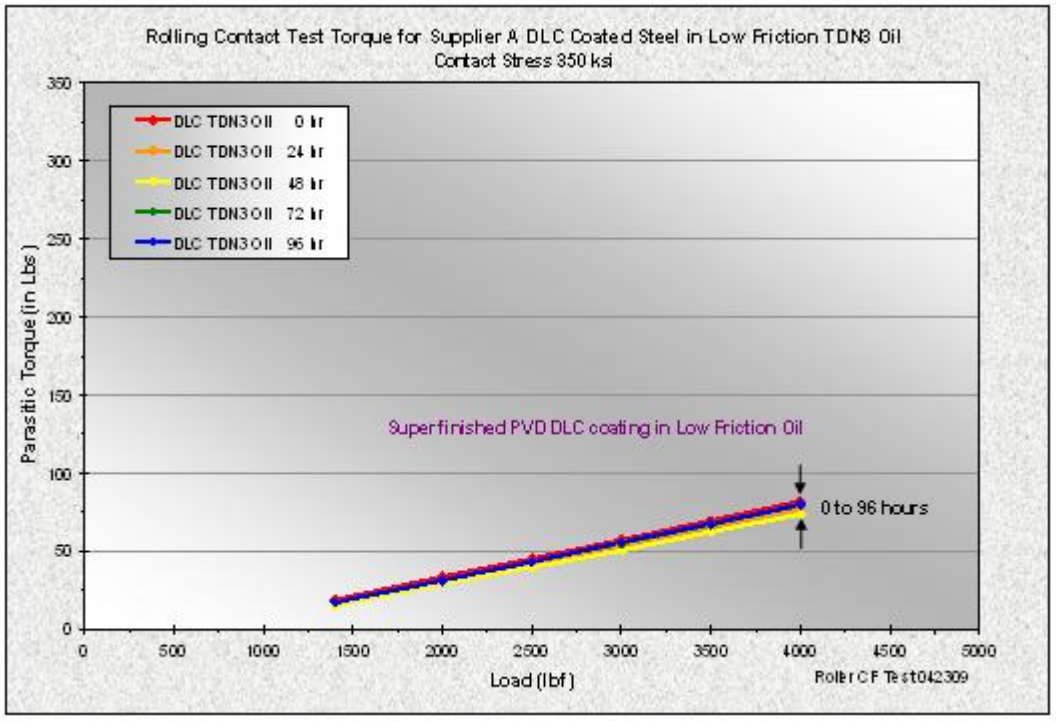

Figure 6.4.4-5: Roller contact fatigue test of super finished, PVD DLC coated steel in low friction TDN3 oil. Wear was minimal with the torque remaining at 82 inch-pounds over the 96 hour test.

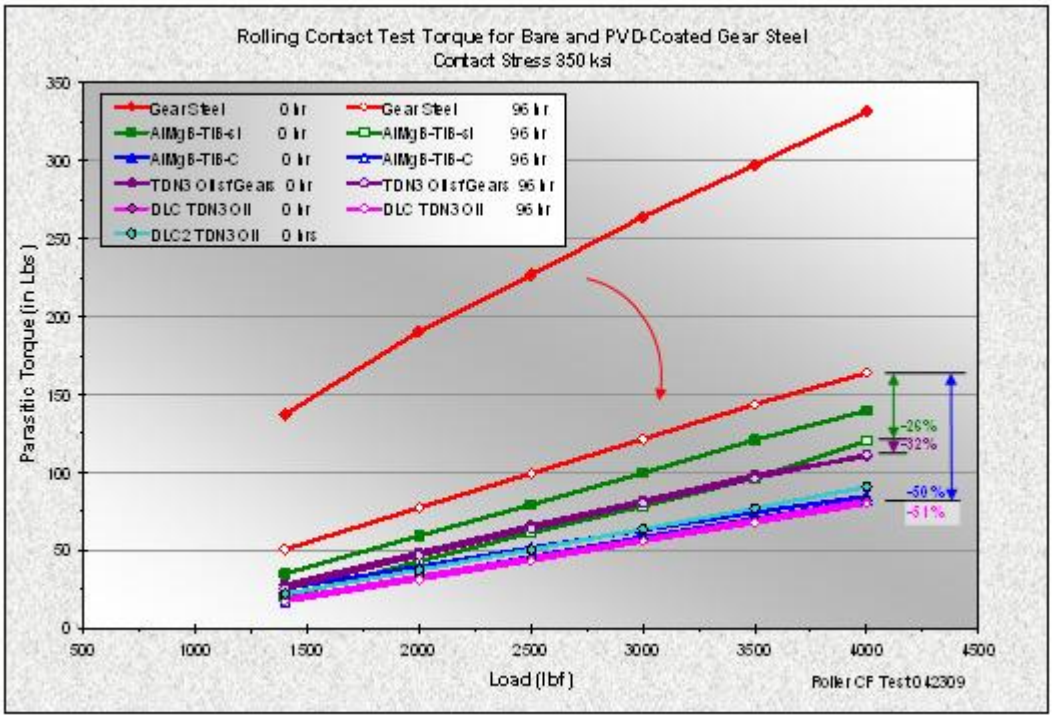

Figure 6.4.4-6: Summary of roller contact fatigue test of comparing bare steel, super finished steel and PVD coated steels. Best result was a 51 percent decrease in torque, and minimal wear, due to PVD DLC coating and TDN3 low friction oil.

6.4.5 Dynamometer Tests for Low Friction driveline components

Dry Sump (Low Fill) Component Efficiency Test

In 2008 Eaton ran a series of dynamometer tests to measure improvements to powertrain efficiency. A baseline transmission with standard production gears and Eaton SAE 50 PS-164 Revision 7 transmission fluid was compared to a similarly equipped dry sump (low fill) transmission. Tests were run at 180 horsepower and at 240 horsepower. For the 180 horsepower test, the baseline transmission showed efficiencies of 98.41 to 99.23 percent, **Figure 6.4.5-1.** At the same horsepower, the comparable dry sump (low fill) transmission produced efficiencies ranging from 98.86 to 99.63 percent. The largest improvement in efficiency attributed to the dry sump run at 180 horsepower was 0.50 percent. This 2008 efficiency improvement was achieved with the under drive gear ratio.

For tests run at 240 horsepower, **Figure 6.4.5-2**, the baseline transmission produced efficiencies varying from 98.36 to 99.10 percent. In comparison the comparable dry sump transmission operated at 240 horsepower gave efficiencies from 98.68 to 99.41 percent, **Figure 6.4.5-2.** The largest improvement in efficiency, 0.32 percent, came from the over drive gear ratio**.** The dry sump, one of five technical elements in the overall implementation strategy, improved efficiency from 0.32 to 0.50 percent.

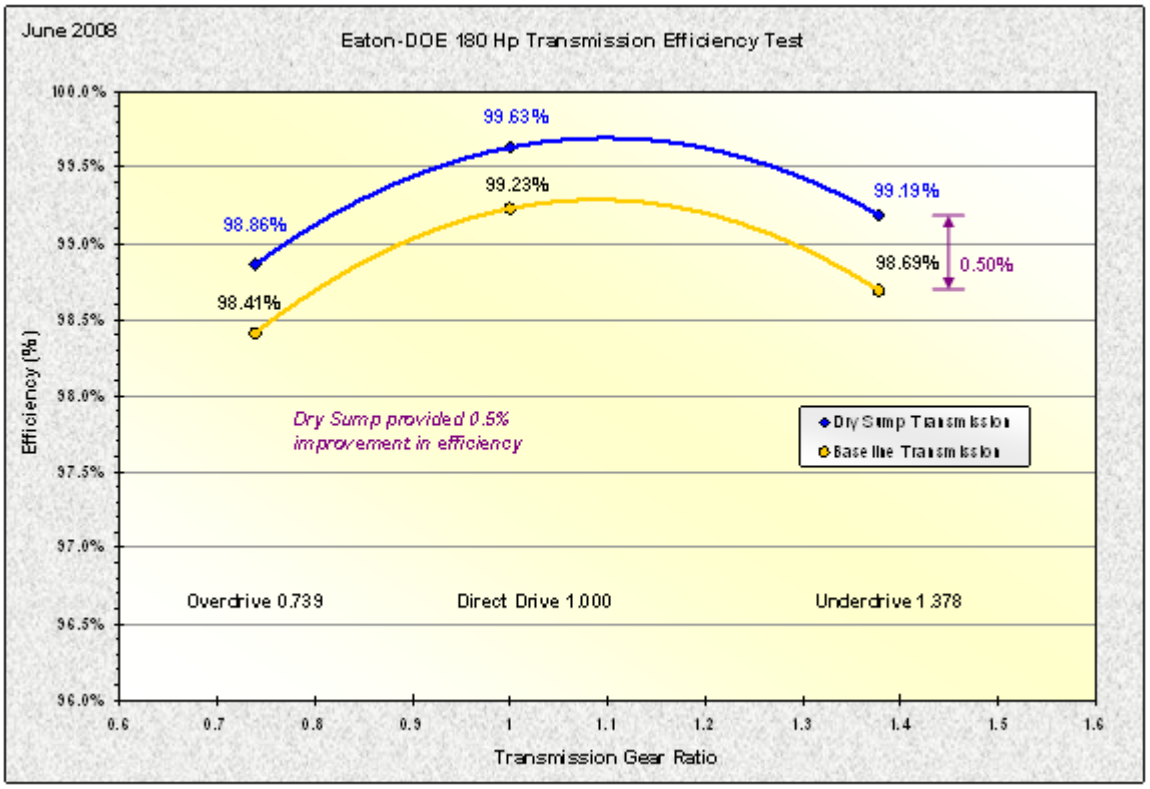

Figure 6.4.5-1: Results from a 180 horsepower dynamometer tests shows the dry sump alone improved efficiency by 0.5 percent compared to the standard transmission. This 2008 improvement relates to decreased churning losses.

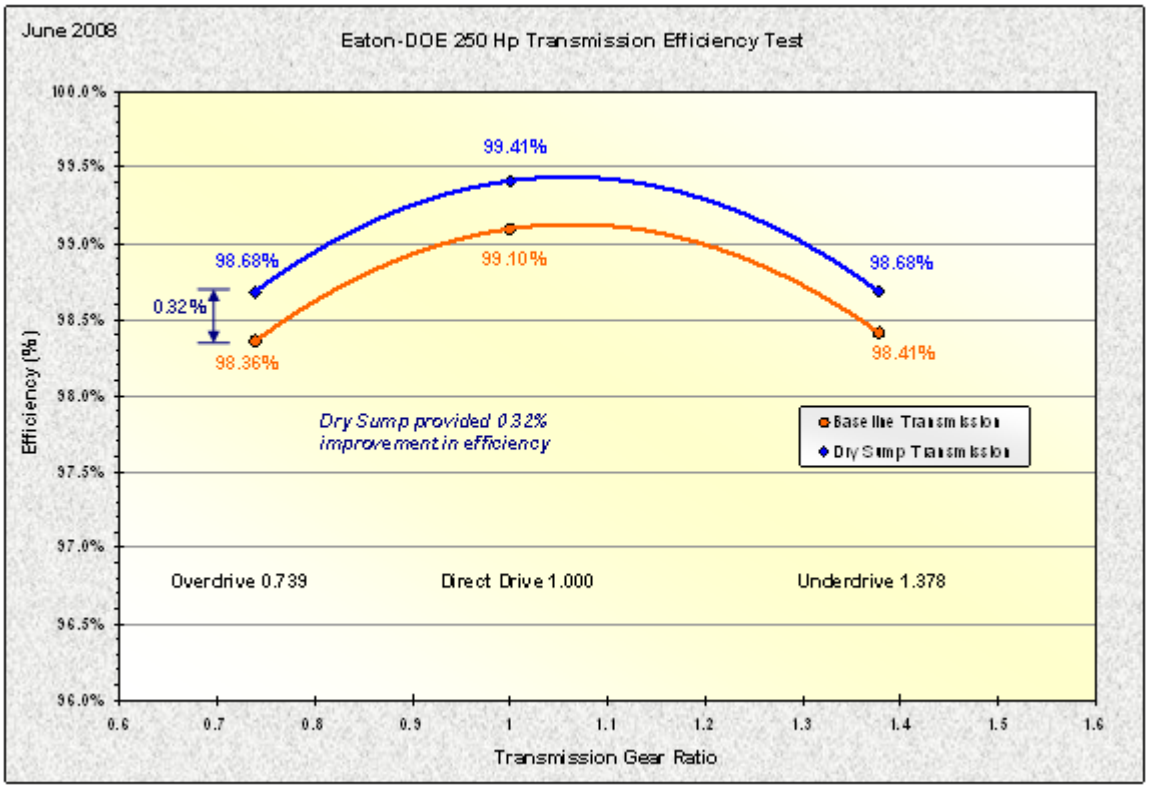

Figure 6.4.5-2: This graph compares efficiency for a standard baseline transmission and the dry sump transmission. The 240 horsepower dynamometer tests run in June 2008 showed a 0.32 percent improvement in efficiency with the 2008 dry sump transmission.

6.4.6 Dynamometer Test results using low friction axle and transmission prototypes

Best Technology Transmission Test, "Best Tech 1"

A more complete, advanced technology, transmission package was tested in June 2009. **Figure 6.4.6-1** presents the results from dynamometer tests conducted in June 2009. Again the test method was to compare a standard baseline transmission to an advanced technology transmission referred to as "Best Tech 1". The "Best Tech 1" transmission utilized four of five technical elements of the implementation strategy. In the Best Tech 1 unit standard gears were replaced with super finished, PVD (physical vapor deposition) coated AlMgB-TiB-C coated gears. The new low friction oil TDN3 was used in place of the standard Revision 7 oil. The Best Tech 1 transmission also used a new dry sump. This modulated valve dry sump used Eaton 5R transmission valves to direct lubricant only to the gear meshes actually transmitting torque. Because of the reduced oil consumption, the oil pump size could be cut in half, providing additional efficiency gains

Figure 6.4.6-1 reveals further increase in efficiency for the Best Tech 1 transmission in 2009 compared to the standard transmission. The 180 horsepower dynamometer test shows that the

standard transmission ran with efficiencies of 98.41 to 99.23 percent. In comparison the 2009 Best Tech 1 transmission produced efficiencies of 99.06 to 99.71 percent. *All three gear ratios tested ran at greater than 99 percent efficiency.* For the over drive ratio, the improvement at 180 horsepower in going from the standard transmission to the 2009 Best Tech 1 transmission was 0.65 percent.

A greater improvement in efficiency is documented in **Figure 6.4.6-2**. The standard transmission gave efficiencies of 98.36 to 99.10 percent at 240 horsepower. The 2009 Best Tech 1 transmission produced efficiencies of 99.12 to 99.69 percent. *The improvement in efficiency from the 2009 Best Tech 1 transmission reached 1.04 percent for the under drive gear ratio. The Best Tech 1 transmission provided gains in efficiency from 0.65 to 1.04 percent.*

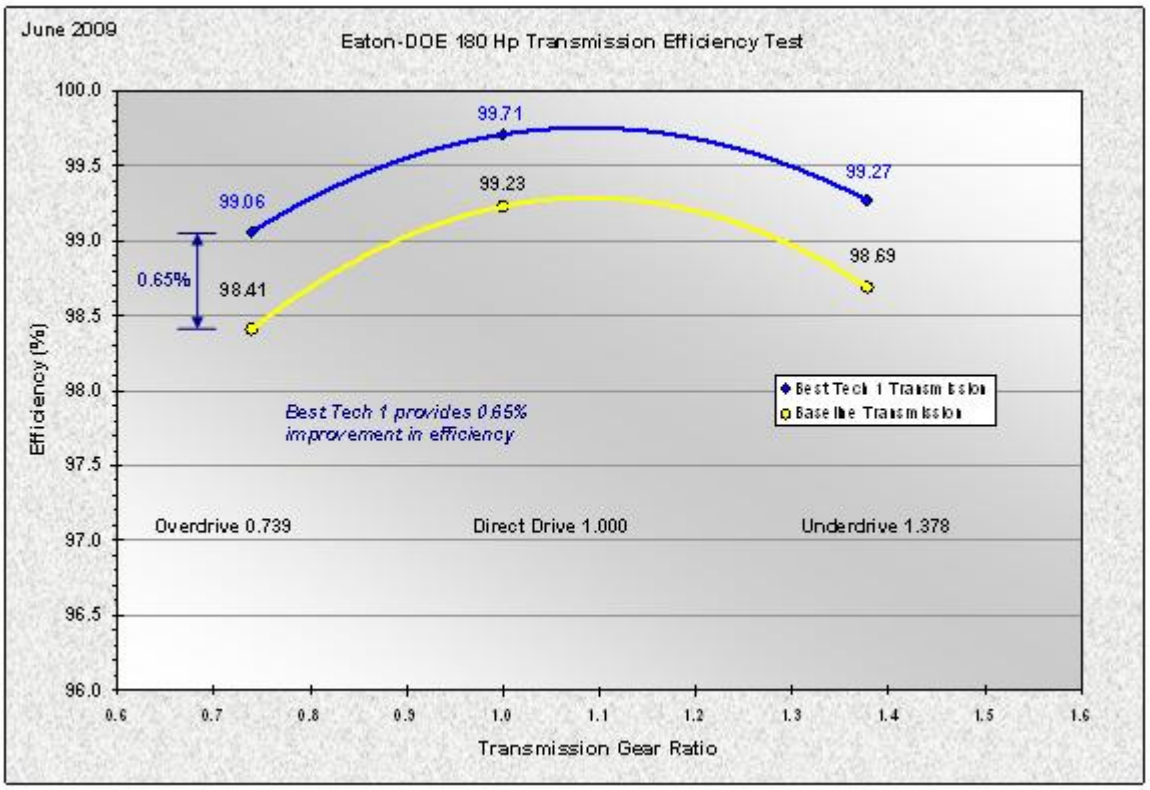

Figure: 6.4.6-1: A 2009 efficiency improvement of 0.65 percent resulted with the Best Tech 1 transmission compared to the standard transmission for 180 horsepower dynamometer tests.

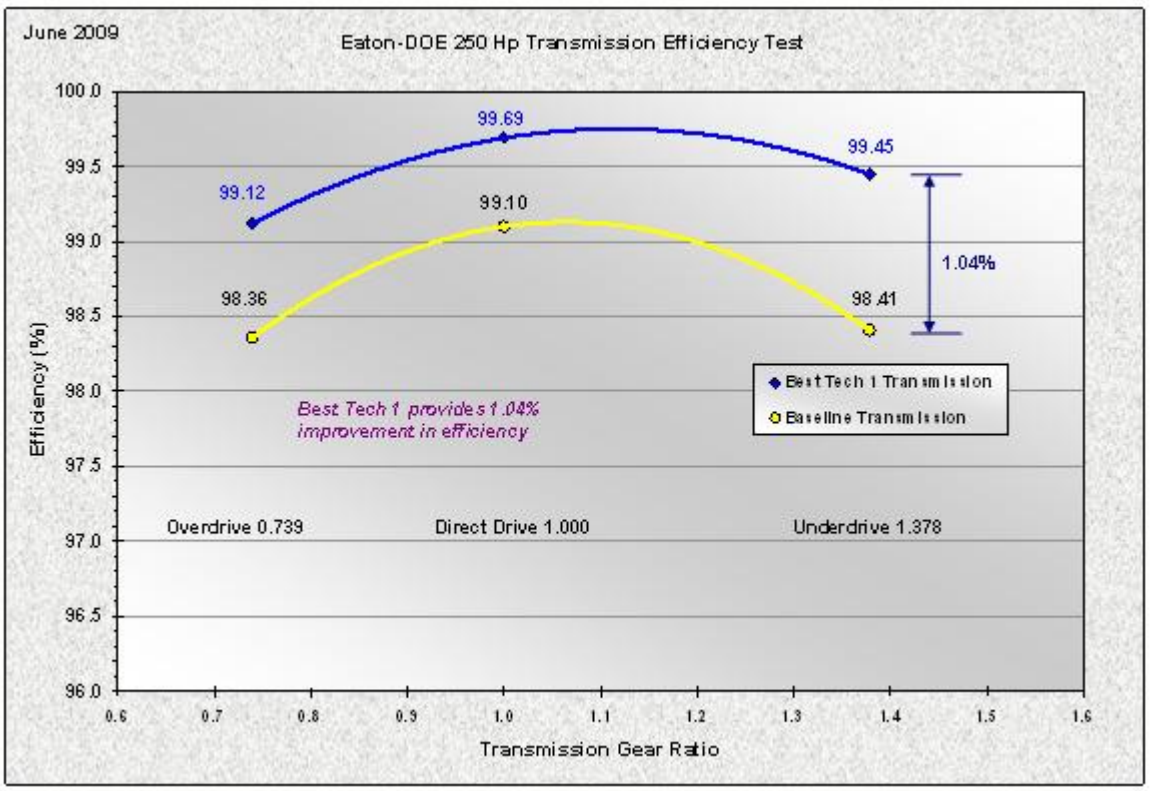

Figure 6.4.6-2: At 240 horsepower the 2009 Best Tech 1 transmission gave efficiencies greater than 99 percent for all three gear ratios tested. For the under drive gear ratio the efficiency improvement of the Best Tech 1 transmission over the standard transmission was *1.04 percent.*

SwRI Transmission Efficiency Tests

DOE granted a "no cost extension" of this powertrain efficiency program. The program ran through December 31, 2009. In this time Eaton contracted Southwest Research Institute (SwRI), San Antonio, TX, to perform "objective third party" efficiency tests.

SwRI performed efficiency testing on two FRO-16210C transmissions. One of the two transmissions had a conventional housing. The second transmission incorporated Eaton's dry sump (low fill). SwRI ran the efficiency tests at two load/speed conditions. Three gear ratios were investigated: 1.38 (Underdrive, 8th gear), 1.00 (Direct, 9th gear) and 0.74 (Overdrive, 10th gear). All tests were performed with a sump temperature of 180 degrees F. The SwRI dynamometer test stand used for the efficiency tests is shown in **Figure 6.4.6-3.**

Figure 6.4.6-3: A standard Eaton transmission is mounted on the transmission efficiency dynamometer test stand at Southwest Research Institute.

Eaton/SWRI; Effect of Oils on Transmission Efficiency

Figure 6.4.6-4 presents the results of examining three oils for their effect on transmission efficiency. All the oil tests were performed with the standard Eaton transmission (full fill sump) and standard production gears. The test speed was 1300 rpm while the input torque was 986 N-M. The first oil tested was Eaton SAE 50 Revision 7, the baseline for the test. The baseline oil gave underdrive, direct and overdrive efficiencies of 98.06, 99.27 and 98.44 percent respectively (red curve with red circle markers). In the SwRI tests the experimental TDN3 low friction oil actually lowered the efficiency (orange curve with square markers). This result is a departure from data generated previously at Eaton for the TDN3 formulation. However, the TDN3 oil tested at SwRI was prepared as a 50-gallon batch and not as the 20-gallon batch mixed for testing at Eaton Innovation Center. A slight gain in efficiency was provided by the new, low viscosity oil TGM5 (yellow curve with diamond markers). This gain is only 0.15 percent and most of the improvement could be attributed to experimental error in the test.

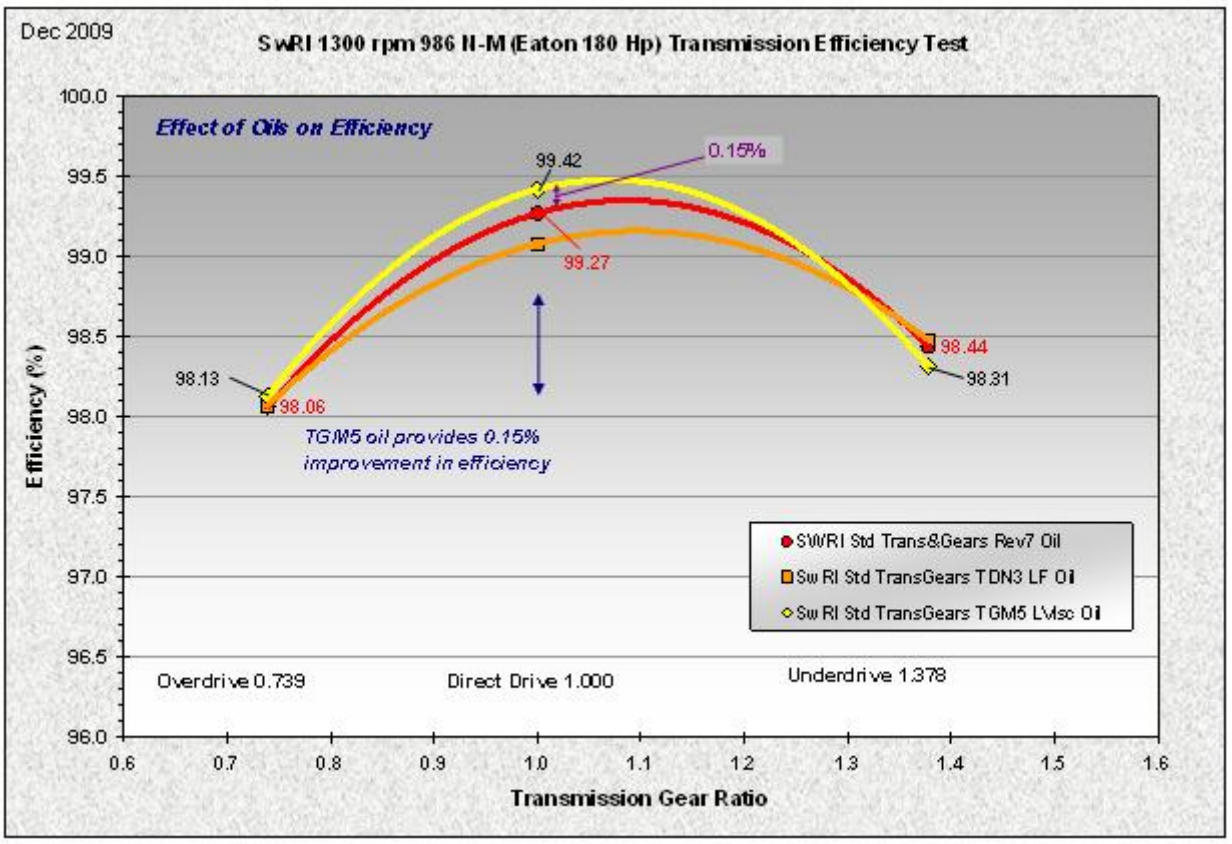

Figure 6.4.6-4: Effects of various oils on the efficiency of a standard transmission are shown. Experimental low friction oil TDN3 actually lowered efficiency while the new low viscosity oil TGM5 raised efficiency slightly.

In a second test for the effects of oils on efficiency, SwRI raised the speed to 1500 rpm and elevated the input torque to 1187 N-m, **Figure 6.4.6-5.** Efficiency results for the Eaton SAE 50 Revision 7 oil were similar to the efficiency for the lower speed, lower torque test of **Figure 6.4.6-4.** Overdrive, direct and underdrive exhibited efficiencies of 98.12, 99.31 and 98.47 percent respectively. Again the experimental low friction TDN3 oil adversely affected efficiency. In comparison the new, low viscosity oil TGM5 showed a small 0.14 percent improvement in efficiency. Direct drive was 99.45 percent efficient. An improvement this small could be absorbed by experimental error. For the most part, the oils tested in an Eaton standard transmission, mounted on the SwRI test stand, failed to improve efficiency.

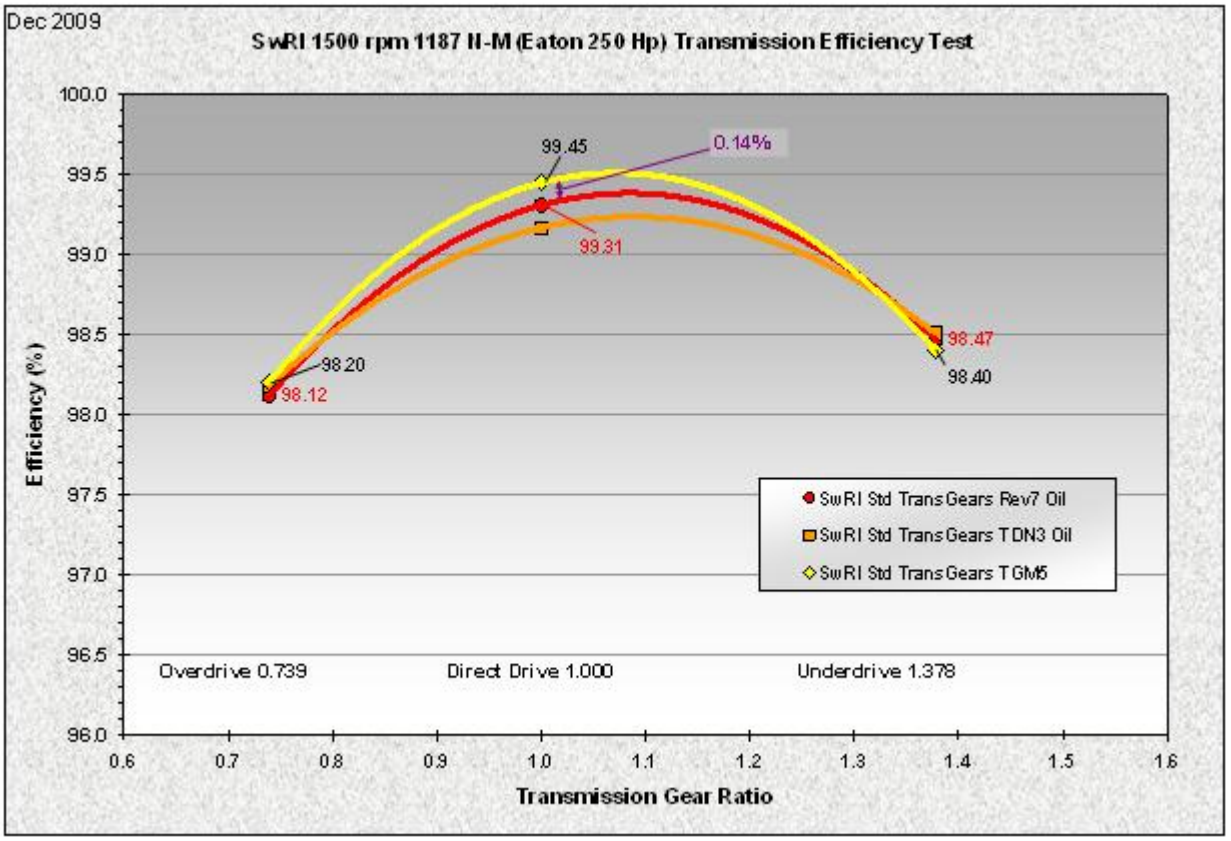

Figure 6.4.6-5: Effects of various oils on the efficiency of a standard transmission are shown. Experimental low friction oil TDN3 actually lowered efficiency while the new low viscosity oil TGM5 raised efficiency slightly.

Eaton/SwRI Effects of Dry Sump and PVD Coated Gears on Efficiency

In **Figure 6.4.6-6** the efficiency of the dry sump (low fill) combined with PVD DLC (physical vapor deposition, Diamond Like Carbon) coated gears and low friction TDN3 oil is compared to the efficiency of a standard transmission with production finished gears and SAE 50 Revision 7 oil. The dry sump, coated gears curve shows an improvement in efficiency at both the overdrive and underdrive conditions. The improvement at underdrive is 0.65 percent. For overdrive the gain in efficiency is 0.62 percent. While these improvements are not staggering, they are an improvement to a transmission that already is 98 plus percent efficient.

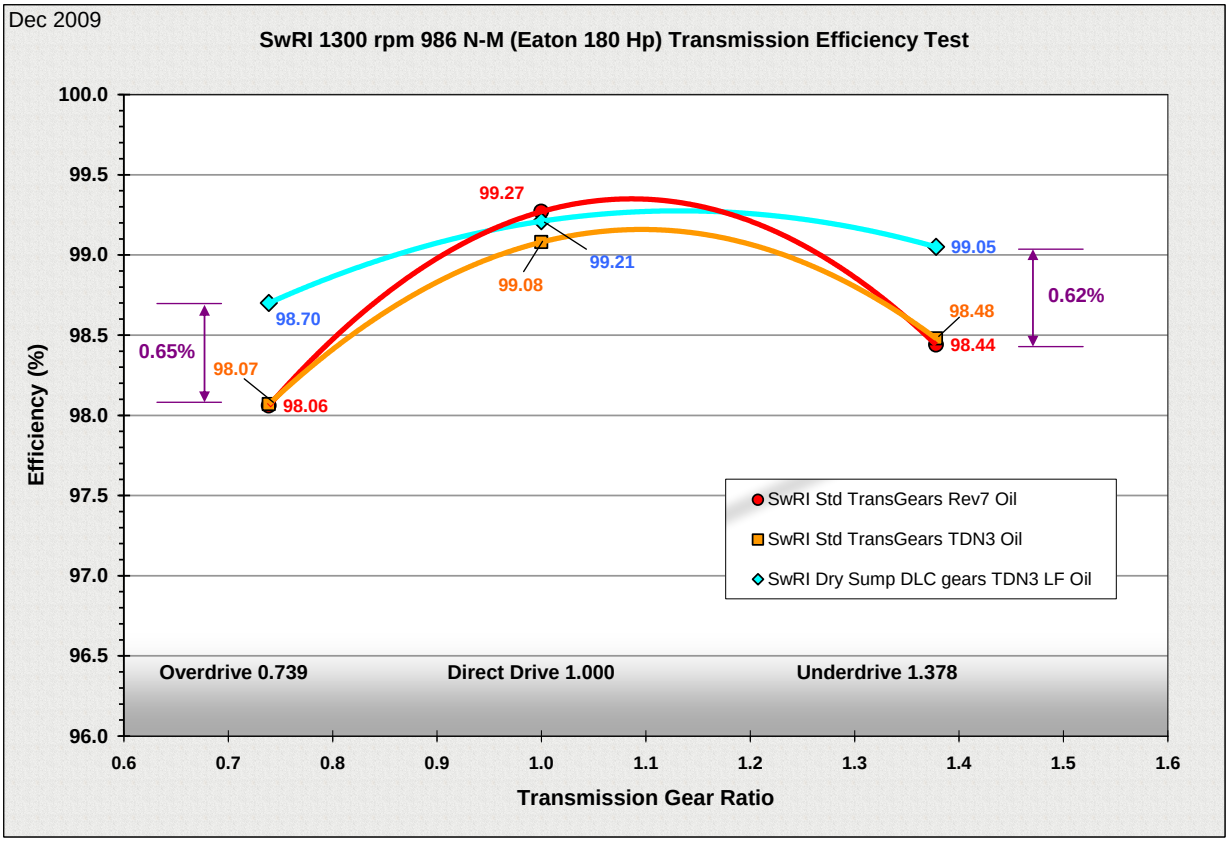

Figure 6.4.6-6: Effects of the dry sump with PVD DLC coated gears and low friction TDN3 oil on efficiency are compared to the efficiency of a standard transmission with SAE 50 Revision 7 oil. The advanced transmission with dry sump showed an efficiency gain of 0.65 percent in overdrive and 0.62 percent for underdrive.

Higher speed and larger input torque produced slightly better results as shown in **Figure 6.4.6-7.** The standard transmission set up (red curve with circle markers) exhibited an efficiency of 98.12 percent in overdrive. The advanced transmission configuration with dry sump and coated gears (light blue curve with diamond markers) gave an efficiency of 98.81 percent in overdrive, an improvement of 0.70 percent. Underdrive also realized an efficiency improvement with the advanced configuration. The standard transmission underdrive efficiency of 98.47 percent increased to 99.05 percent with the dry sump and coated gears.

Overall the technical elements of the implementation strategy improved efficiency from 0.62 to 0.70 percent in an independent third-party test. A larger improvement in efficiency from the advanced configuration was anticipated from the Southwest Research Institute tests. However, the TDN3 oil did not perform as well as was seen in the past. The TDN3 oil limited the efficiency improvement potential of the advanced transmission configuration.

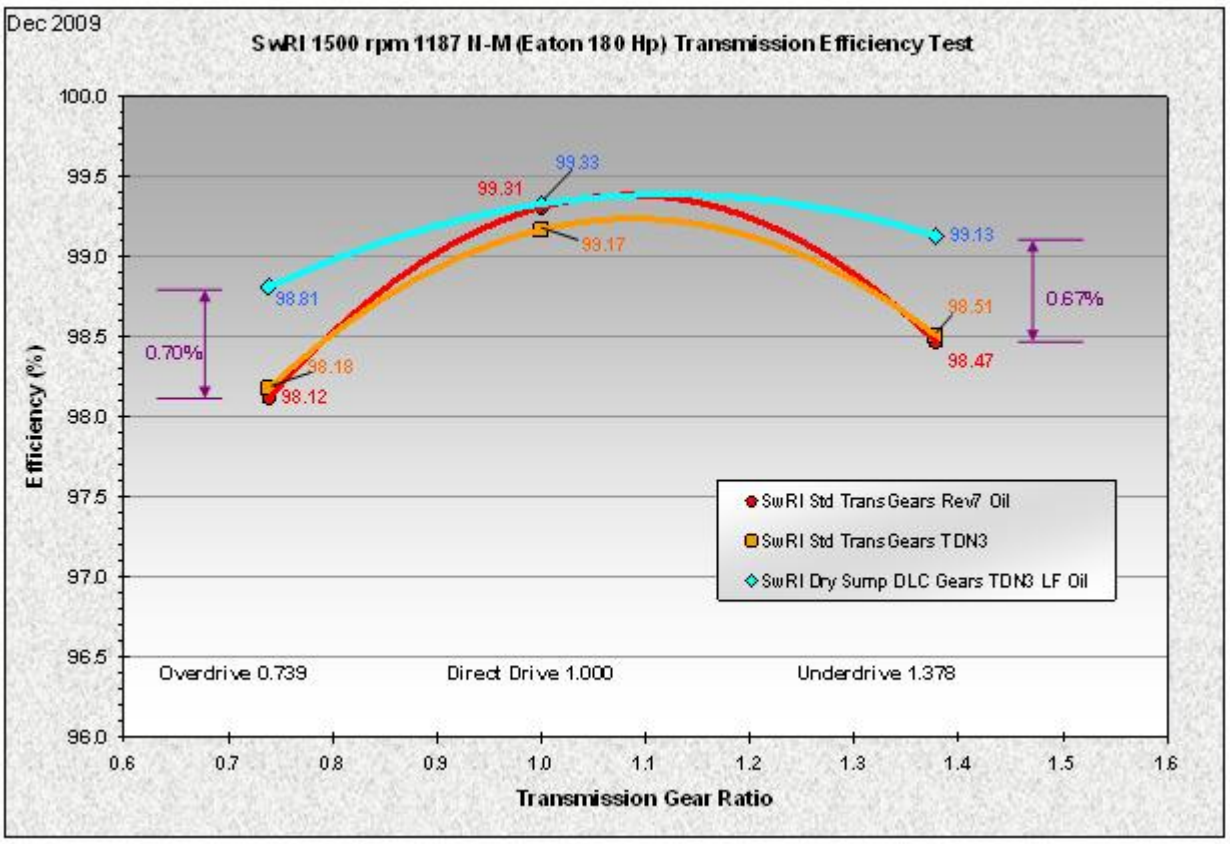

Figure 6.4.6-7: Effects of the dry sump with PVD DLC coated gears and low friction TDN3 oil on efficiency are compared to the efficiency of a standard transmission with SAE 50 Revision 7 oil. At 1500 rpm and 1187 N-m input torque the advanced transmission with dry sump showed an efficiency gain of 0.70 percent in overdrive and 0.67 percent for underdrive.

Axle Planetary Efficiency Test (Catepillar)

Caterpillar used a final drive four-square testing rig to collect axle efficiency data. A picture of this rig can be seen below in **Figure 6.4.6-8.**

Based on the results of previous test runs, the final drive efficiency comparison among the baseline oils and the low friction oil 20 was constructed. As can be seen in the **Figure 6.4.6-9**, low friction Oil 20 provides significant benefit throughout the entire load/speed curve. Additionally, Oil 20 showed increased benefit at the low speed, heavily loaded conditions. This benefit correlates strongly with what was seen with Oil 20 in the Differential Four-Square testing conducted in the past.

Utilizing this information in the model, the final drive contribution of energy gain by using the low friction oil 20 was rolled up to the machine flywheel to be in the range of *1.19 to 1.75 percent and from 0.36 to 1.38 percent for Run-out and Rim-pull* at different gearing conditions, respectively, **Figure 6.4.6-10.**

When the low speed data between the base-line Oil 18 is compared with that of the low friction Oil 20, *a 2 percent efficiency improvement* is seen across the low speed points.

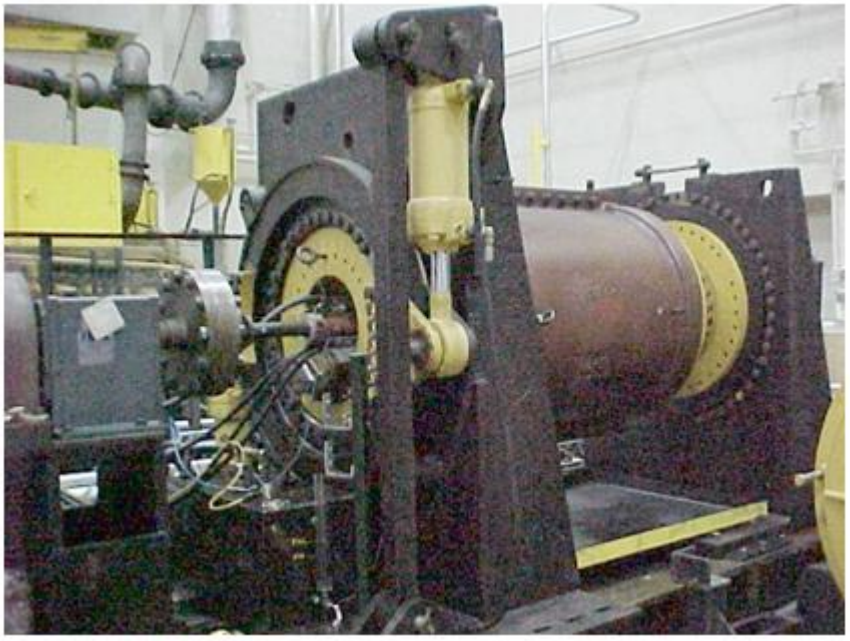

Figure 6.4.6-8: The Final Drive Four-Square testing Rig.

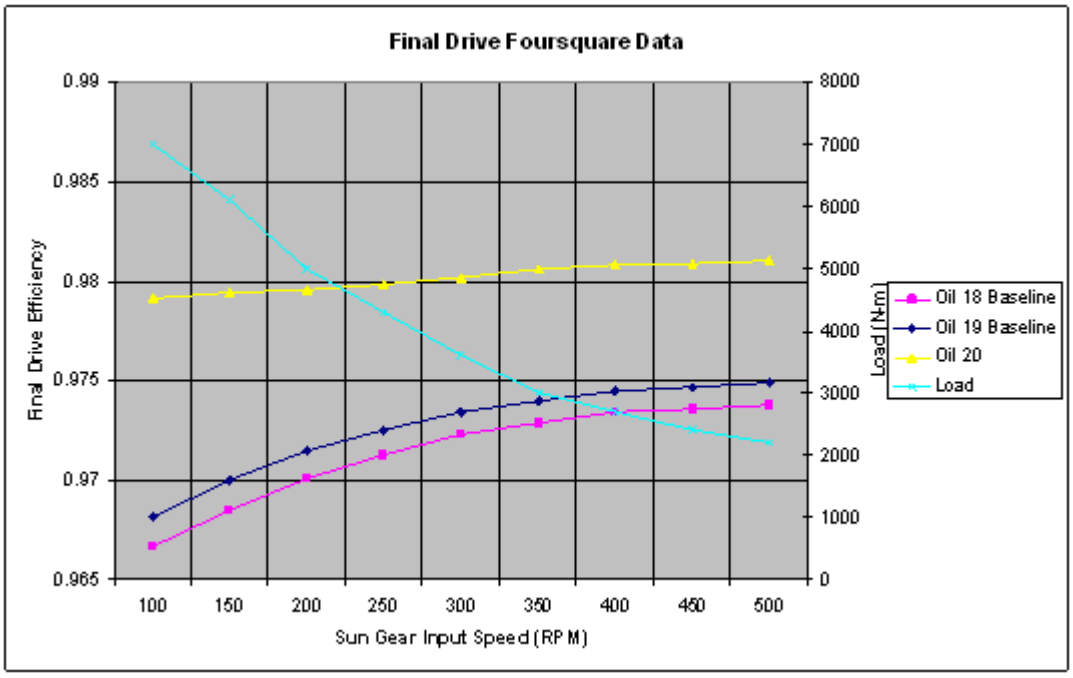

Figure 6.4.6-9: Final Drive Four-Square Efficiency Testing Data.

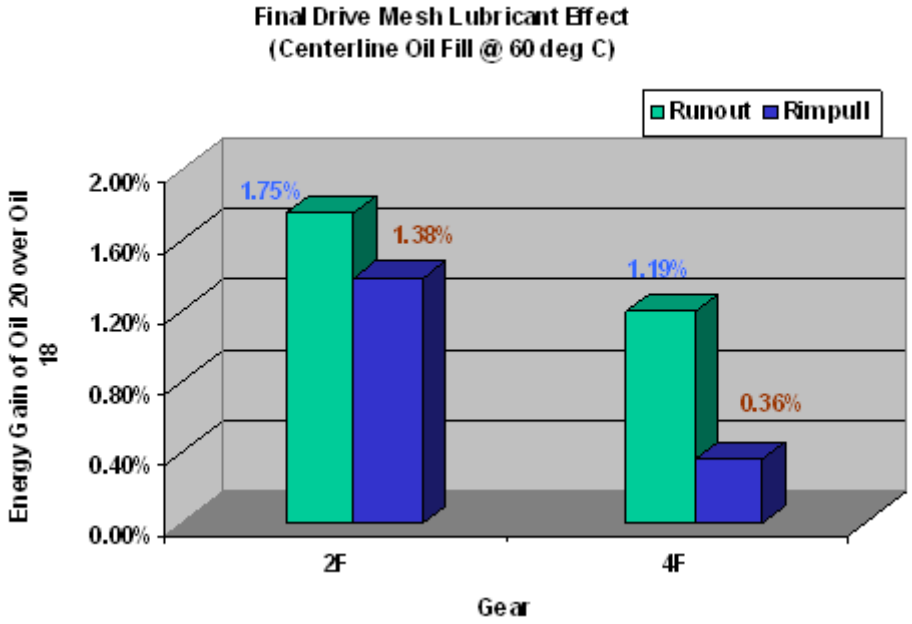

Figure 6.4.6-10: Final drive energy gain rolled up to the flywheel.

7.0 TECHNICAL ACCOMPLISHMENTS

1. One transmission configuration ran at greater than 99 percent efficiency for all three gear ratios tested: Under drive, direct drive and over drive. This transmission used a low fill sump, a reduced size oil pump with modulating valves, a low friction oil TDN3 and super finished and PVD AlMgB-TiB-C coated gears.
2. Technical elements of the implementation strategy improved transmission efficiency by one percent and improved drive axle efficiency by two percent.
3. A family of experimental low friction transmission fluids, including RYF4, SKQ5, TDN3 and TGM5, exhibited friction coefficients 40 percent lower than the commercial Roadranger SAE 50 Revision 7 oil and 68 percent lower than commercial Mobil SHC 50 lubricant.
4. An injectable, low friction additive RJK5 was formulated. During a test, injecting RJK5 additive into Roadranger SAE 50 Revision 7 oil immediately lowered the friction coefficient of the oil by 24 percent.
5. Designs were prepared for low fill sumps on a transmission and on a drive axle. The transmission low fill sump included an oil pump with three modulating valves and spray tubes.
6. PVD gear coatings including Diamond-Like Carbon (DLC) and Aluminum-Magnsesium-Boride (AlMgB) were modified for greater durability and lower friction.
7. The reduction in friction coefficient with increasing wear for components with high initial surface roughness was documented.

8.0 CONCLUSIONS

1. Truck driveline efficiency can be improved by three percent or more through use of the technical elements of the implementation strategy, including low fill sumps, low friction lubricants, super finishing and PVD gear coatings.
2. Low fill sumps and low friction lubricants provide the largest impacts in improving driveline efficiency.
3. Greater improvements in efficiency are possible with drive axles than with transmissions.
4. Physical Vapor Deposition (PVD) coatings for gears can be improved further by improving the RF (radio frequency) cleaning process, by manipulating the shape of the particle cloud around the gear teeth and by incorporating solid lubricants within the coating.

9.0 RECOMMENDATIONS

1. Truck transmissions and axles should incorporate low fill sumps with spray tubes and modulating valves.
2. Low viscosity and low friction oils with solid lubricant-forming compounds should be developed further and tested for friction reduction at very high contact stresses like 150 to 350 ksi.
3. Lubricants should be formulated specifically to work with PVD coated surfaces rather than bare steel surfaces.
4. All gears for truck transmissions and axles should be super finished, with the REM or similar process.